Phase control and measurement in digital microscopy

Matthew Raphael Arnison

A thesis submitted for the degree of
Doctor of Philosophy

Physical Optics Laboratory
School of Physics
University of Sydney

July 2003

Summary

The ongoing merger of the digital and optical components of the modern microscope is creating opportunities for new measurement techniques, along with new challenges for optical modelling. This thesis investigates several such opportunities and challenges which are particularly relevant to biomedical imaging. Fourier optics is used throughout the thesis as the underlying conceptual model, with a particular emphasis on three–dimensional Fourier optics.

A new challenge for optical modelling provided by digital microscopy is the relaxation of traditional symmetry constraints on optical design. An extension of optical transfer function theory to deal with arbitrary lens pupil functions is presented in this thesis. This is used to chart the 3D vectorial structure of the spatial frequency spectrum of the intensity in the focal region of a high aperture lens when illuminated by linearly polarised beam.

Wavefront coding has been used successfully in paraxial imaging systems to extend the depth of field. This is achieved by controlling the pupil phase with a cubic phase mask, and thereby balancing optical behaviour with digital processing.

In this thesis I present a high aperture vectorial model for focusing with a cubic phase mask, and compare it with results calculated using the paraxial approximation. The effect of a refractive index change is also explored. High aperture measurements of the point spread function are reported, along with experimental confirmation of high aperture extended depth of field imaging of a biological specimen.

Differential interference contrast is a popular method for imaging phase changes in otherwise transparent biological specimens. In this thesis I report on a new isotropic algorithm for retrieving the phase from differential interference contrast images of the phase gradient, using phase shifting, two directions of shear, and non–iterative Fourier phase integration incorporating a modified spiral phase transform. This method does not assume that the specimen has a constant amplitude. A simulation is presented which demonstrates good agreement between the retrieved phase and the phase of the simulated object, with excellent immunity to imaging noise.

Acknowledgements

Thanks to Carol Cogswell, my first supervisor in this project, for her ideas, energy and enthusiasm. It was Carol who got me addicted to biomedical imaging research a whole decade ago. Colin Sheppard was my second supervisor and shared with me his creativity and curiosity, his delight in discussing simple yet mind–bending optical ideas, and his ability to answer even my most primitive questions with patience and clarity.

I found Peter Török to be a most generous and supportive collaborator, who has a great passion for accurate optical modelling of important but challenging microscopy problems. He is wonderfully persistent in seeking the physical meaning behind the mathematics. Working with Peter has been very rewarding.

Kieran Larkin is one of those people who thinks in 3D Fourier space just as easily as most people think in real space. Nicholas Smith has been a great friend and colleague. I have been lucky to be able to collaborate with such a playful pair of physicists.

W. Thomas Cathey, Edward Dowski and Sara Tucker shared their pioneering expertise in the world of wavefront coding. CDM Optics provided an extended loan of a cubic phase mask and a 1 µm pinhole.

Thanks to Ken Weigert for his excellent craftsmanship. He helped design and then carefully constructed our custom microscope components. Graham Mannes and the rest of the physics workshop crew have also contributed in various practical matters.

Thanks to all my colleagues at the optics tea table, including Chris Barton, Ian Cooper, Paul Cronin, Janey Lin, Felix Margadant, Kiyofumi Matsuda, Trina Ng, David Philp, Maitreyee Roy, Shakil Rehman, Manjula Sharma, Shoshanna Cole, Elizabeth West, and Paul Xu. We all did our best never to talk about anything which any of us knew the least thing about. Paul "just quietly" Cronin was a great lab mate and co-conspirator in linoleum optics. Daniel Andruczyk, Nicholas Parslow and Shoshanna Cole suffered an office invasion by our couch and were good fun to hang out with after the tea table was lost.

I enjoyed my conference and email discussions with fellow microscopy researchers Martin Booth, Mats Gustafsson, Rainer Heintzmann, Farnaz Massoumian, and David Paganin. Taisuke Ota shared with me a manic month of experimental development in Osaka, and my experimental results in this thesis owe much to the skills I learned in that time. I also gained a lot from working with David Philp and Janey Lin on our early wavefront coding experiments at the University of Sydney. Eleanor Kable and Guy Cox at the Australian Key Centre for Microscopy and Microanalysis were ever ready to help with practical microscopy questions.

Thanks to Andreas Schönle for gently bringing to my attention a mathematical error I made in a journal paper published as part of this project.

I was fortunate to journey widely as part of this project, and the following people were kind enough to invite me and look after me at various overseas destinations:

- W. Thomas Cathey, Edward Dowski, Sara Tucker, Sherif Sherif, and Carol Cogswell at Colorado University;
- Peter Török at Oxford University;
- Satoshi Kawata, Nicholas Smith and Taisuke Ota at Osaka University;
- Joseph Braat at TU Delft; and
- Fu–Jen Kao at National Sun Yat-sen University.

Christopher Durrant gave me a personal course in electromagnetic theory from the ground up. Information technology support was provided by David Dawes, Sebastian Juraszek, and Anthony Monger. Felix Margadant leant me his second hand computer equipment. Felix runs so close to the bleeding edge, that using only his hand–me–downs I was able to run my calculations at blazing speed. Andrew Trimboli lent me his laptop for several of my overseas trips, which made a big improvement on carting my desktop compter around.

Cheerful and efficient administration support was provided by Leanne Howie, Evelyn Soh, Elizabeth Morris, and the legendary Noni McIntosh. Vicky Moore was always helpful at the physics library counter. Gotaro Mori at STA Travel helped me squeeze, juggle and shift a complicated round–the–world itinerary.

This work was supported financially by the Australian Research Council, a Sydney University Physics Scholarship, the School of Physics Denison Fund, the University of Sydney Postgraduate Research Support Scheme, a James Kently Memorial Scholarship, and an Optical Society of America New Focus Student Travel Grant.

Thanks to the people who develop and distribute the free software I depended on, including Debian GNU/Linux, XFree86, icewm, galeon, mozilla, pine, SpamAssassin, LyX, LaTeX, Pybliographer, ghostscript, gcc, nedit, octave, OpenDX, and all the free software that runs the internet. Thanks also to the creators of Mathematica, MATLAB, Photoshop, Illustrator, and Acrobat PDF. I relied on a huge and diverse music soundtrack for this project. Thanks to all those artists for music to do physics by.

I have been nurtured and entertained by the copious support and companionship of my friends and family. My dad John and my mum Jocelyn have looked after me in so many ways.

I am privileged to share life's journey with my partner Colleen, laughing, learning, living and growing together in our orbit around the Sun. Thank you Colleen for your tender care and support.

Ruby and Rudi, our canine companions, come last but not leashed. They never tire of taking simple and intuitive pleasure in mastering the physics of motion.

Declaration of originality

In this thesis I have acknowledged the contributions to my research made by my colleagues and collaborators. I have also cited the literature as appropriate. All other work presented is mine alone.

Significant contributions and collaborations included the following:

- Chapter 3: It was Colin Sheppard's suggestion to extend the transfer function theory from his papers (Sheppard et al., 1994; Sheppard and Larkin, 1997) in order to deal with arbitrary pupil functions. Andreas Schönle gently pointed out a mathematical error in the article which chapter 3 is based on (Arnison and Sheppard, 2002), enabling me to correct the error while preparing this thesis.

- Chapter 4: Peter Török collaborated with me on the refractive index change model for cubic phase mask imaging, contributing both his theoretical expertise and his source code. My heavy use of the projected pupil integration method was inspired by a personal demonstration of the technique by Kieran Larkin.

- Chapter 5: Carol Cogswell provided the vision and leadership for high aperture wavefront coding and worked on all the experiments and processing steps for the biological imaging result presented in section 5.3. Eleanor Kable and Theresa Dibbayawan prepared the HeLa cell specimen. David Philp and Janey Lin assisted with the 1 µm fluorescent bead point spread function measurement used to restore the HeLa cell EDF image, while Edward Dowski and Claude Rosignol worked on inverse filter design and image restoration.

- Chapter 7: Colin Sheppard and Kieran Larkin both provided key ideas used in the spiral phase algorithm, as detailed in appendix A.

Matthew Arnison
Submitted July 2003
Emended April 2004

Publications and presentations

Chapters 3–5 and chapter 7 are based on the work presented in the following publications:

- Arnison, M. R. and Sheppard, C. J. R. (2002) "A 3D vectorial optical transfer function suitable for arbitrary pupil functions," *Opt. Commun.*, **211**(1-6), 53–63.

- Arnison, M. R., Cogswell, C. J., Sheppard, C. J. R., and Török, P. (2003) "Wavefront coding fluorescence microscopy using high aperture lenses," in P. Török and F.-J. Kao (Eds.), *Optical imaging and microscopy: techniques and advanced systems*, vol. 87 of the Springer series in optical sciences, chap. 6, pp. 143–165, Springer-Verlag, Berlin.

- Arnison, M. R., Larkin, K. G., Sheppard, C. J. R., Smith, N. I., and Cogswell, C. J. (2004) "Linear phase imaging using differential interference contrast microscopy," *J. Microsc.*, **214**(1), 7–12.

The following conference presentations highlighted work described in this thesis (* indicates presenting authors):

- C. J. Cogswell,* M. R. Arnison, E. R. Dowski Jr., S. C. Tucker, and W. T. Cathey, "A new generation, fast 3D fluorescence microscope using wavefront coding optics," *Microscopy Society of America*, (Oregon, USA, 1999).

- C. J. Cogswell,* M. R. Arnison,* E. R. Dowski Jr.,* S. C. Tucker,* and W. T. Cathey,* "A novel 3D fluorescence microscope using wavefront coding optics," *Optical Society of America Annual Meeting*, (Santa Clara, CA, USA, 1999).

- C. J. Cogswell,* M. R. Arnison, E. R. Dowski Jr., S. C. Tucker, and W. T. Cathey, "Extended–depth–of–focus fluorescence microscope made possible using wavefront coding," *Focus on Microscopy*, (Shirahama, Japan, 2000).

- M. R. Arnison,* P. Török, C. J. R. Sheppard, W. T. Cathey, E. R. Dowski, Jr., and C. J. Cogswell, "High resolution extended depth of field microscopy using wavefront coding," *Students International Symposium on Advanced Engineering*, (Osaka, Japan, 2000), (invited talk).

- M. R. Arnison, P. Török, C. J. R. Sheppard,* W. T. Cathey, E. R. Dowski Jr., and C. J. Cogswell, "Wavefront coding in high numerical aperture microscopy," *Australian Optical Society XIII*, (Adelaide, Australia, 2000).

- W. T. Cathey,* M. R. Arnison, C. J. Cogswell, and E. R. Dowski Jr., "Large depth of field in fluorescence imaging of live cells," *Optical Society of America Annual Meeting*, (Rhode Island, USA, 2000).

- C. J. Cogswell, M. R. Arnison,* E. R. Dowski Jr., S. C. Tucker, and W. T. Cathey, "Wavefront coding gives rise to a fast extended–depth–of–focus fluorescence microscope," *Optics Within the Life Sciences VI*, (Sydney, Australia, 2000).

- C. J. Cogswell,* E. R. Dowski Jr., I. A. Prischepa, G. E. Johnson, S. C. Tucker, M. R. Arnison, and W. T. Cathey, "Recent advances in extended depth of focus microscopy for live–cell imaging," *Three-dimensional and multidimensional microscopy: image acquisition and processing VIII* at *SPIE Photonics West*, (San Jose, CA, USA, 2001).

- M. R. Arnison,* P. Török, C. J. R. Sheppard, W. T. Cathey, E. R. Dowski Jr., and C. J. Cogswell, "A model for wavefront coding in high numerical aperture microscopy," *Optical Society of America Annual Meeting*, (Long Beach, CA, USA, 2001).

- M. R. Arnison* and C. J. R. Sheppard, "Three dimensional optical transfer functions for high aperture systems with non-symmetric pupils," *Australian Optical Society Conference*, (Sydney, Australia, 2002).

- M. R. Arnison,* C. J. R. Sheppard, and P. Török, "High aperture wavefront coding," *Focus on Microscopy*, (Kaohsiung, Taiwan, 2002), (invited talk).

Acronyms, abbreviations and conventions

$\Longleftrightarrow$	Fourier transform relation
$\otimes$	convolution
$\star$	correlation
1D, 2D, 3D	one dimension, two dimensions, three dimensions
α	aperture half-angle
axial	parallel to the optical axis, z
amplitude	amplitude a of a complex field $a\mathrm{e}^{\mathrm{i}\phi}$
CCD	charge-coupled device
CPM	cubic phase mask
DC	direct current, i.e. image background or bias
DIC	differential interference contrast
EDF	extended depth of field
FITC	fluorescein isothiocyanate, a fluorescent dye
$f(x,y,z)$	functions in real space are usually lower case
$F(m,n,s)$	equivalent functions in Fourier space are often upper case
g'	projection of function g
$\mathcal{F}\{h\}$	Fourier transform of function h
$\mathbf{f}$	vectors are set in boldface
FFT	fast Fourier transform
$k_0 = 2\pi/\lambda_0$	vacuum wave number for light of wavelength λ_0
lateral	orthogonal to the optical axis
$\mathbf{m} = (m,n,s)$	vector in Fourier space, unit directional vector

n	refractive index
NA	numerical aperture
OTF	optical transfer function
paraxial	approximate scalar field propagation for small angles to the optical axis
phase	phase ϕ of a complex field $ae^{i\phi}$; optical path length variations
PSF	point spread function
SNR	signal to noise ratio
transverse	orthogonal to the optical axis
vectorial	high aperture electromagnetic focusing theory
wave	unit of phase (2π radians)
widefield	conventional microscope imaging, without pupil filters
$\mathbf{x} = (x, y, z)$	vector in real space

Contents

Part I

Theme and theory

Chapter 1

Overview and background

The original microscope consisted of a light source, a lens, and a specimen. For centuries, most of the design work on microscopes centred on the optics of the lenses used. But over the last few decades a fundamental shift has been gathering steam, as the field of digital microscopy matures.

Arguably this shift was launched by the modern confocal laser scanning microscope. Such microscopes delivered major improvements in resolution and 3D imaging. Confocal microscopes were made practical by the integration of laser illumination, specimen scanning, and electronic image storage. To fully analyse and optimise a confocal microscope, the optics of these additional elements must be considered as part of a full system.

Just as confocal microscopes evolved, conventional microscopes also become increasingly automated and computerised. Image digitisation is now a routine part of microscopy, whether by a charge–coupled device (CCD) camera or by attaching an analog to digital converter to the output of a photomultiplier tube.

Yet the final image from a microscope was generally still considered to be the intensity measurements made by a photodetector. Image restoration and deconvolution were reckoned to be post-processing steps, often applied only when further improvement was desired on the best possible microscope images that could be obtained with optics alone. Although such systems have often been called digital microscopes, a firewall remained between the design domains of optical imaging and digital processing.

The final step in the shift towards digital microscopy is to think of any microscope as a hybrid of optical, digital and computational parts. Just as different lenses within a high quality microscope objective contribute different imaging properties in a balanced dance towards perfection, different optical components can be combined with computational steps to bring out desirable new imaging features in the full digital microscope.

A potent example of this is wavefront coding, investigated in part II. Wavefront coding relies on an optical mask with a carefully designed phase function. When the mask is placed in the lens pupil it dramatically alters the phase and produces a terrible image from an otherwise excellent microscope. Yet the mask allows an image to be retrieved computationally which has similar resolution and superior depth of field compared with images from the unaltered microscope.

In the design of wavefront coding, digital microscopy is taken to its logical conclusion, with the possibilities of computational processing leading to deliberate and seemingly adverse optical modifications to the microscope. The full system gives a previously unobtainable tradeoff between the imaging characteristics of resolution, depth of field and dynamic range, opening up new applications for high resolution microscopy.

Interferometry has a much older heritage than wavefront coding but it is similar in its indirect approach to imaging. Instead of producing an intensity image of the amplitude of the object, interferometry uses superposition of electric fields to produce intensity fringes. The desired data is actually a phase image of the specimen, which can only be obtained using mathematical post-processing.

One modern variant of interferometry is the differential interference contrast (DIC) microscope. Generally DIC is used in a qualitative way to observe the phase gradient of a specimen. However, by capturing a series of phase shifted images, we can then reconstruct an image of the phase of the specimen. In chapter 7 I simulate a novel method for doing this, creating a new variety of digital microscope.

Fourier optics is a very useful way to model imaging performance when combining optical elements, and a key benefit is the ease with which the same Fourier transforms can be used for continued processing in the computer. However, Fourier optics as it is widely known is a 2D discipline, which fails to accurately model the 3D nature of high angle focusing. Top quality microscope objectives focus at very high angles, and this has lead to an emerging field of 3D Fourier optics.

The first papers on 3D Fourier optics are decades old, but development since then has been sporadic. Because direct numerical calculations were beyond the reach of computers, research has focused on special cases which allow analytic simplification of the problem. Computers have now increased in power so that more general 3D Fourier optics calculations are plausible, and this field is now ripe for development.

On the experimental side, relevant developments include high resolution spatial light modulators which can filter both amplitude and phase, accurate fabrication of phase filters at strengths of many wavelengths, and continuing improvements in the speed, resolution, pre-

cision and sensitivity of CCD cameras. These developments all provide increased flexibility, which motivates the exploration of models with changed assumptions, such as relaxing the traditional assumption of radial symmetry in high aperture focusing theory.

In chapter 3, I contribute an extension of previous transfer function theories which allows for 3D Fourier optics analysis of generalised optical elements, such as the wavefront coding mask described above.

In the remainder of this chapter, I will set the historical context for this thesis. Microscopy research is about the development of instrumentation which is in turn then applied as a measurement tool in other fields of science. This means that a crucial part of the historical context is the applications of the microscopy techniques discussed. Then in chapter 2 I give an overview of the relevant microscopy theory, before moving on to the first novel work of this thesis in chapter 3.

Two major domains where microscopy is used are in materials inspection and biological research. Although there is often overlap between the observation methods used in each domain, my emphasis in this thesis is on biomedical applications of digital microscopy. I will begin my background review by categorising the different varieties of digital microscopy, before focusing on two specific applications: extended depth of field and phase imaging.

1.1 Digital microscopy

I define a digital microscope as any system for creating images using a microscope together with digital technology. This generally includes any system control and information processing aspects of microscopy which are not purely optical, as most modern uses of electronics in microscope design emphasise digital rather than analog technology. This is a fairly broad definition of digital microscopy, so it is useful to categorise such systems in order of increasing sophistication:

1. A purely optical microscope, where the controls are manual and the user views the image directly through the eyepiece. There are no digital components in microscopes of this category.

2. The simplest digital microscope, where the optical image is captured digitally. Images may be digitised using a CCD camera, a photomultiplier tube (PMT) combined with an analog-to-digital converter, or by scanning photographs.

3. Automated digital microscopes, where operations such as focusing and filter selection are controlled by a computer. In conjunction with digital image capture, this allows

automated collection of images in different microscopy modes over a period of time. Confocal microscopes are generally in this category or higher.

4. Post-processing digital microscopes, where a useful image is obtained optically, but the user depends on computer processing of the digitised optical microscope image in order to discern specimen features of interest. This might include 3D visualisation or deconvolution to increase resolution.

5. Full hybrid digital microscopes, where optical and digital components depend on each other to deliver the desired imaging goals. Such microscopes are also called hybrid optical digital imaging systems.

Simple digital microscopes (category 2) evolved to allow digital presentation and quantitative image analysis. Image processing was generally restricted to such operations as contrast improvement, noise suppression and segmentation of objects (Wield et al., 1968).

Automated digital microscopes (category 3) certainly improved the efficiency of studies which involved repeated operations, and made many microscope features more convenient to use. However, the final image did not necessarily show any improvement on what could be obtained without any digitisation at all.

Even confocal microscopes may be placed in category 3. Marvin Minksy's original confocal microscope operated without computers, or indeed even lasers. He used analog electronics to control specimen scanning and build up an image for display (Minsky, 1961, 1988). Of course, subsequent addition of lasers and computers made the system much more powerful and indeed convenient. This enabled commercialisation of the technology two decades after Minsky's patent (Cox and Sheppard, 1983a,b).

This development echoes a trend in the early history of digital microscopy: collection and processing were assisted and automated first using analog electronics and later improved using lasers and computers. The original flying spot microscope used cathode ray tubes (CRT) for both scanning and display (Young and Roberts, 1951). Subsequent upgrades replaced the illumination CRT by a laser (Slomba et al., 1972) and controlled the scanning using a computer (Jarvis, 1974). Stein et al. (1969) integrated a computer with a conventional microscope to automate illumination control and specimen positioning, and for digitising the image. A detailed history of technological upgrades to microscopy was provided by Inoué (1995).

Post-processing microscopes (category 4) have been developing strongly over the past two decades in parallel with confocal microscopes. Deconvolution of a carefully collected

focus series from a conventional microscope (Castleman, 1979; Agard and Sedat, 1983) can compensate for the effects of defocus on the frequency content of the images, and allow resolution and optical sectioning abilities roughly equal to that of confocal microscopes. Deconvolution is often used in fluorescence microscopy.

Of course, deconvolution can also be applied to confocal microscopes, with a corresponding further increase in resolution (Shaw, 1995; Holmes et al., 1995). However, this is limited in practice by the lower dynamic range of confocal images due to the confocal pinhole, together with the fact that confocal images already provide sufficient optical sectioning to isolate most image data within a focal plane.

Volume datasets from both confocal microscopes and deconvolved conventional microscopes can be visualised in 3D (Carlsson et al., 1985). This has evolved to become a highly useful method for biologists and material scientists to inspect 3D specimen structures.

This thesis is concerned with systems in category 5, full hybrid digital microscopes. This field has been developing rapidly in the past two decades. Cathey et al. (1984) pointed out the advantages of designing an optical system to specifically enhance an image restoration method applied after electronic image capture, an approach which led to the field of wavefront coding (Cathey and Dowski, 2002). However, if we relax the requirement of *digital* electronics, then interferometers can be thought of as hybrid optical systems with a much longer history. This is because no useful image is obtained until after mathematical post-processing is applied to the intensity fringes obtained optically.

Many hybrid microscope systems have recently been developed. 4π two-photon confocal microscopy (Hell et al., 1997) produces an image with clear axial ringing of specimen features. Deconvolution is required to obtain an image without these distracting artefacts. Once this is done, substantial gains in resolution are possible, at the expense of significant optical complexity.

Closely related is standing wave microscopy and structured illumination microscopy (Bailey et al., 1993; Gustafsson et al., 1999; Gustafsson, 1999). In such systems, interference patterns are setup within the specimen. By phase shifting these patterns and combining the results, the observable spatial frequency range is extended, giving higher resolution.

In section 1.2.2 I give an overview of methods for extending the depth of field of microscopy. Some of the methods are purely digital — they take as input images obtained without any optical modification. Other methods, such as wavefront coding, are hybrid systems.

In section 1.3 I discuss various methods for imaging the phase of the specimen. Such methods generally involve hybrid systems, as phase cannot be digitised directly nor viewed by the eye.

1.2 Extended depth of field microscopy

In recent years live cell fluorescence microscopy has become increasingly important in biological and medical studies. This is largely due to new genetic engineering techniques which allow cell features to grow their own fluorescent markers. A popular example is green fluorescent protein. This avoids the need to stain, and thereby kill, a cell specimen before taking fluorescence images, and thus provides a major new method for observing live cell dynamics.

With this new opportunity come new challenges. Because in earlier days the process of staining often killed the cells, microscopists could do little additional harm by squashing the preparation to make it flat, thereby making it easier to image with a high resolution, shallow depth of field lens. In modern live cell fluorescence imaging, the specimen may be quite thick (in optical terms). Yet a single 2D image per time–step may still be sufficient for many studies, as long as there is a large depth of field as well as high resolution.

Light is a scarce resource for live cell fluorescence microscopy. To image rapidly changing specimens the microscopist needs to capture images quickly. One of the chief constraints on imaging speed is the light intensity. Increasing the illumination will result in faster acquisition, but can affect specimen behaviour through heating, or reduce fluorescent intensity through photobleaching.

Another major constraint is the depth of field. Working at high resolution gives a very thin plane of focus, leading to the need to constantly "hunt" with the focus knob while viewing thick specimens with rapidly moving or changing features. When recording data, such situations require the time-consuming capture of multiple focal planes, thus making it nearly impossible to perform many live cell studies.

Ideally we would like to achieve the following goals:

- use all available light to acquire images quickly,
- achieve maximum lateral resolution,
- and yet have a large depth of field.

However, such goals are contradictory in a normal microscope.

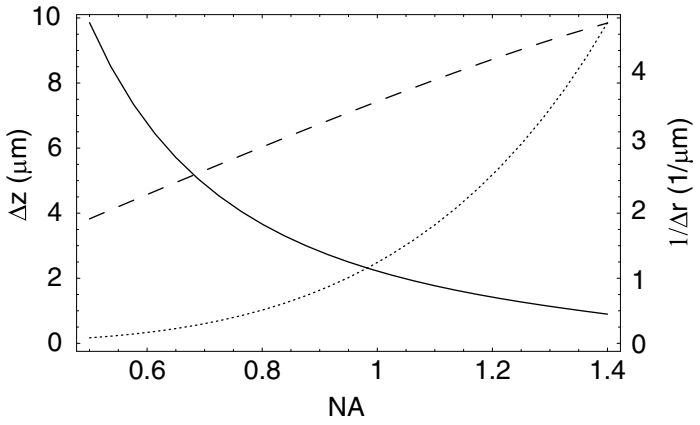

Figure 1.1: Depth of field Δz (*solid line*), lateral resolution $1/\Delta r$ (*dashed line*) and peak intensity at focus I_{focus} (*dotted line* – arbitrary units) for oil immersion ($n_{\text{oil}} = 1.518$) aplanatic microscope objectives with a typical range of NAs and $\lambda_0 = 0.53\,\mu\text{m}$ as the vacuum wavelength.

For a high aperture aplanatic lens, the depth of field is (Sheppard, 1988)

$$\Delta z = 1.77\lambda / \left[4\sin^2\frac{\alpha}{2}\left(1 - \frac{1}{3}\tan^4\frac{\alpha}{2}\right)\right] , \tag{1.1}$$

where Δz is defined as the distance along the optical axis for which the intensity is more than half the maximum. Here the focal region wavelength is λ and the aperture half–angle is α. A high aperture value for the lateral resolution $1/\Delta r$ can be approximated from the full–width at half–maximum (FWHM) of the unpolarised intensity point spread function (PSF) (Richards and Wolf, 1959). We can use the polarised PSF to find the peak intensity at focus, as a rough indication of the high aperture light collection efficiency (Richards and Wolf, 1959, Eq. (3.18)),

$$I_{\text{focus}} \propto \left[1 - \frac{5}{8}(\cos^{\frac{3}{2}}\alpha)(1 + \frac{3}{5}\cos\alpha)\right]^2 . \tag{1.2}$$

These relationships are plotted in Fig. 1.1 for a range of numerical apertures (NA),

$$\text{NA} = n_1 \sin\alpha \tag{1.3}$$

where n_1 is the refractive index of the immersion medium. The lateral resolution was determined using a numerically obtained FWHM of Eq. (5.2) from Richards and Wolf (1959) for

each α. Clearly maximising the depth of field conflicts with the goals of high resolution and light efficiency.

1.2.1 Focus and depth of field

It is worth considering what depth of field and focusing actually mean in microscopy (Berek, 1927). In a standard imaging system, the collection lens is moved back and forth along the optical axis to bring corresponding regions of the object into focus. We know when a system is in focus because at that lens position the image features are sharpest, and the system is imaging the widest range of spatial frequencies from the corresponding plane in the object. Moving the lens from this position will blur the image, and we denote this with the equivalent terms defocus and misfocus.

If the object is 3D rather than 2D, then in general we need to also consider contributions from out of focus planes of the object. The 3D transfer function, as described in section 2.4, is a general description of how the lens will image the overall and relative strength of spatial frequencies from all planes of the specimen.

In a conventional system, higher spatial frequencies will rapidly drop off away from the focal plane, while the low spatial frequencies persist for a long distance, giving the characteristic image blur for misfocused objects. This is because most of the collection and illumination power passes through all planes of the specimen, and thereby each plane of the specimen will continue to contribute power to the final image even when highly defocused.

In a confocal system, both high and low frequency components are strongly damped with misfocus. This is because the addition of a confocal pinhole to the collection system all but eliminates contributions from defocused specimen planes.

This is most clearly demonstrated in reflection confocal microscopy where the object lies on a single surface but at different heights (Hamilton et al., 1981). Conventional images of such a surface will blur out towards a medium level intensity for regions with increasing misfocus. In contrast, a confocal image will decay quickly to black without giving blurred images at intermediate levels of misfocus. This behaviour is called *optical sectioning*.

Differential interference contrast microscopes display both kinds of behaviour, because they produce images with a mix of brightfield and phase gradient information. The brightfield contribution to the image has weak optical sectioning, but the differential phase contribution is more strongly optically sectioned. In addition, the brightfield contribution will image the phase of defocused objects.

Because of the decoupling of focus planes provided by optical sectioning in confocal microscopy, a through-focus series of confocal images gives a good dataset for 3D visualisation. An alternative is to apply deconvolution to a conventional 3D dataset and thereby obtain optical sectioning through post-processing. In both cases the goal is to reduce the depth of field as much as possible. This provides dual benefits. Firstly it means that axial features will be more clearly resolved as higher axial frequencies will be imaged. Secondly it improves the optical sectioning, allowing finer axial slicing without contamination from object features in neighbouring focal planes.

Scanning electron microscopy (SEM) is well known for its ability to produce stunning 3D images. However, the images viewed with human eyes are actually 2D. What gives the impression of 3D imaging is the very large depth of field. SEMs operate with a very small aperture to avoid aberrations due to the poor quality of electromagnetic lenses. This small aperture gives a very large depth of field.

When visualising 3D volume datasets from confocal microscopes, we have a complete 3D dataset, so we can rotate the specimen in the computer and then recalculate a 2D view of the 3D volume for display. On a SEM microscope we cannot so easily obtain a 3D array of image intensities. When we wish to see a specimen from a different angle, we generally rotate it within the SEM itself.

In seeking to extend the depth of field of conventional optical microscopes, we are looking for the kind of 3D imaging behaviour that an SEM has. The user needs to be able to get rapid feedback when they move and rotate the specimen. System speed is crucial for this reason, adding to the speed requirements already discussed on page 8.

1.2.2 Methods for extending the depth of field

A number of methods have been proposed to work around the normally conflicting needs of resolution, depth of field and light efficiency to produce an extended depth of field (EDF) microscope.

Before the advent of CCD cameras, Häusler (1972) proposed a two step method to extend the depth of focus for incoherent microscopy. First, an axially integrated photographic image is acquired by leaving the camera shutter open while the focus is smoothly changed. The second step is to deconvolve the image with the integration system transfer function. Häusler showed that as long as the focus change is more than twice the thickness of the object, the transfer function for the integrated image does not change for parts of the object at different

depths — effectively the transfer function is invariant with defocus. The transfer function also has no zeros, providing for easy single–step deconvolution.

This method could be performed easily with a modern microscope, as demonstrated recently by Juškaitis et al. (2001). However, the need to smoothly vary the focus is a time–consuming task requiring some sort of optical displacement within the microscope. This is in conflict with our goal of rapid image acquisition.

A similar approach is to simply image each plane of the specimen, stepping through focus, then construct an EDF image by taking the axial average of the 3D image stack, or some other more sophisticated operation which selects the best focused pixel for each transverse specimen point (Häusler and Korner, 1984; Holmes et al., 1991; Schechner et al., 2000; Schechner and Kiryati, 2000; Synoptics Ltd., 2001; Valdecasas et al., 2001). Axial selection has been described in application to confocal microscopy (Sheppard et al., 1983), where optical sectioning makes the EDF post–processing straightforward. Widefield deconvolution images could also be used. In all cases the requirements of focal scanning and multiple plane image capture are major limitations on overall acquisition speed.

Potuluri et al. (2001) have demonstrated the use of rotational shear interferometry with a conventional widefield transmission microscope. This technique, using incoherent light, adds significant complexity, and sacrifices some signal–to–noise ratio (SNR). However the authors claim an effectively infinite depth of field. The main practical limit on the depth of field is the change in magnification with depth (perspective projection) and the rapid drop in image contrast away from the imaging lens focal plane.

Another approach is to use a pupil mask to increase the depth of field, combined with digital image restoration. This creates a digital–optical microscope system. Designing with such a combination in mind allows additional capabilities not possible with a purely optical system. We can think of the pupil as encoding the optical wavefront, so that digital restoration can decode a final image, which gives us the term *wavefront coding*.

In general a pupil mask will be some complex function of amplitude and phase. The function might be smoothly varying, and therefore usable over a range of wavelengths. Or it might be discontinuous in step sizes that depend on the wavelength, such as a binary phase mask.

Many articles have explored the use of amplitude pupil masks (Gibson and Lanni, 1989; Gu and Sheppard, 1992; Ojeda-Castañeda et al., 1988, 1989; Streibl, 1984a; Tschunko, 1974, 1981; Welford, 1960), including their use in high aperture systems (Campos et al., 2000). These can be effective at increasing the depth of field, but they do tend to reduce dramatically

the light throughput of the pupil. This poses a major problem for low light fluorescence microscopy.

Steel (1960) proposed and constructed a modified lens with negative spherical aberration. The lens profile changed from linear to spherical along the radius, merging the shape of an axicon with that of a normal lens, and therefore giving a longer depth of field.

Wilson et al. (2002) have designed a system which combines an annulus with a binary phase mask. The phase mask places most of the input beam power into the transmitting part of the annular pupil, which gives a large boost in light throughput compared to using the annulus alone. This combination gives a ten times increase in depth of field. The EDF image is laterally scanned in x and y, and then deconvolution is applied as a post–processing step.

Binary phase masks are popular in lithography where the wavelength can be fixed. However, in widefield microscopy any optical component that depends on a certain wavelength imposes serious restrictions. In epi-fluorescence, the incident and excited light both pass through the same lens. Since the incident and excited light are at different wavelengths, any wavelength dependent pupil masks would need to be imaged onto the lens pupil from beyond the beam splitter that separates the incoming and outgoing light paths. This adds significant complexity to the optical design of a widefield microscope.

The system proposed by Wilson et al. (2002) is designed for two-photon confocal microscopy. Optical complexity, monochromatic light, and scanning are issues that confocal microscopy needs to deal with anyway, so this method of PSF engineering adds relatively little overhead.

Wavefront coding is an incoherent imaging technique that relies on the use of a smoothly varying phase–only pupil mask, along with digital processing. Two specific functions that have been successful are the cubic (Bradburn et al., 1997; Dowski and Cathey, 1995) and logarithmic (Chi and George, 2001; Sherif and Cathey, 2003) phase masks, where the phase is a cubic or logarithmic function of distance from the centre of the pupil, in either radial or rectangular co-ordinates. Mezouari and Harvey (2003) have proposed quartic and logarithmic radial phase masks for reducing the impact of both spherical aberration and defocus. They note that the improvement in aberration tolerance is not as great as for rectangular masks, but that radial phase masks are easier to construct.

Elkind et al. (2003) have presented an iterative method for designing phase–only pupil masks, based on the Gerchberg–Saxton algorithm. Elkind et al. define the system performance to be measured by the transfer function averaged over each of N transverse planes across the desired EDF range. In each iteration step of the method they apply a constraint that the system performance should be as close as possible to an ideal in-focus response.

They then vary the pupil mask until the performance converges. Their simulated and experimental results show a $10\times$ depth of field increase.

Unlike wavefront coding, the Elkind et al. method does not need post-processing to retrieve the final EDF image. However, their results also show that while all spatial frequencies are transmitted over the wider depth of field, the overall contrast is weaker at the extreme end of the EDF range. In comparison, contrast levels show little variation across the EDF range in wavefront coding systems.

The cubic phase mask (CPM) was part of the first generation of wavefront coding systems, designed for general purpose EDF imaging. The CPM has since been investigated for use in standard (low aperture) microscopy (Tucker et al., 1999). The mask can give a ten times increase in the depth of field without significant loss of transverse resolution.

Commercialisation of wavefront coding microscopy has proceeded in parallel with my research for this thesis. Patent licensing (Cathey and Dowski, 1998; Dowski and Cogswell, 2003) and application development is being managed by CDM Optics (CO, USA). In 2002, Carl Zeiss released a product called DeepView which uses wavefront coding to provide EDF imaging for materials and industrial inspection microscopy. Olympus Optical Company have also licensed wavefront coding technology in order to develop an EDF endoscopy product.

Converting a standard widefield microscope to a wavefront coding system is straightforward. The phase mask is simply placed as close as possible to the back pupil of the microscope objective. The digital restoration is a simple single-step deconvolution, which can operate at video rates. Once a phase mask is chosen to match a lens and application, an appropriate digital inverse filter can be designed by measuring the PSF. The resulting optical–digital system is specimen independent. The wavefront coding process is illustrated in Fig. 1.2.

The main trade off is a lowering of the SNR as compared with normal widefield imaging. The CPM also introduces an imaging artefact where specimen features away from best focus are slightly laterally shifted in the image. This is in addition to a perspective projection due to the imaging geometry, since an EDF image is obtained from a lens at a single position on the optical axis. Finally, as the CPM is a rectangular design, it strongly emphasises spatial frequencies that are aligned with the CCD pixel axes.

High aperture imaging does produce the best lateral resolution, but it also requires more complex theory to model accurately. Yet nearly all of the investigations of EDF techniques reviewed above are low aperture. For this thesis I have chosen a particular EDF method, wavefront coding with a cubic phase plate, and investigated its theoretical (chapter 4) and experimental (chapter 5) performance for high aperture microscopy.

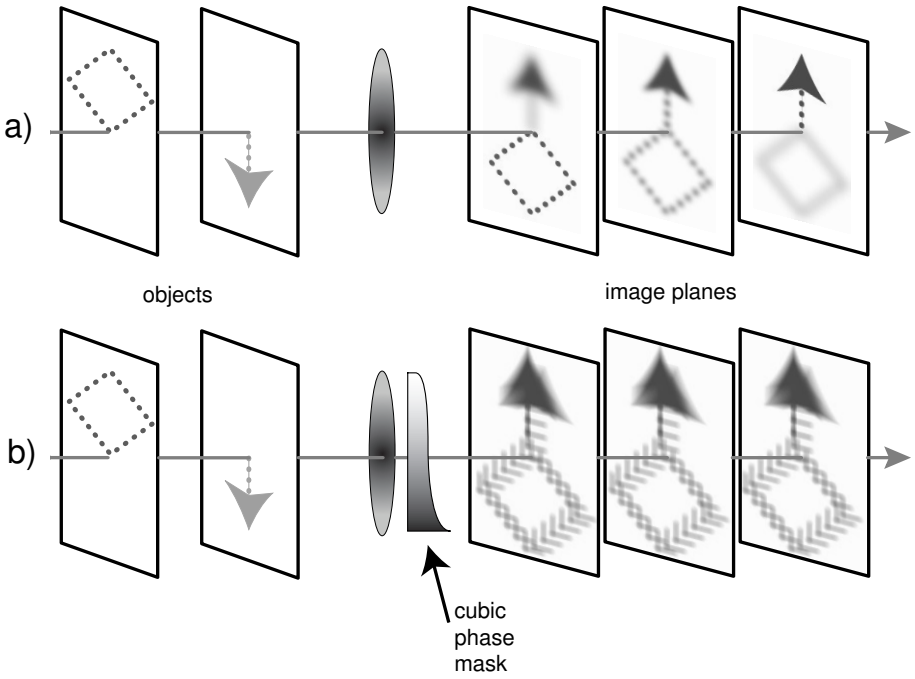

Figure 1.2: How points are imaged in standard versus wavefront coding systems: (a) Conventional (small depth of field) system with two axially–separated objects to the left of a lens. Because each object obtains best focus at a different image plane, the arrow object points decrease in diameter toward their plane of best focus (far right), while the object points of the diamond are increasingly blurred. (b) Inserting a CPM causes points from both objects to be equivalently blurred over the same range of image planes. Signal processing can be applied to any one of these images to remove the constant blur and produce a sharply–focused EDF image.

1.3 Phase microscopy

The main mechanisms for imaging specimen features in biological microscopy are amplitude, fluorescence, polarisation and phase. Amplitude and fluorescence are certainly very popular, however until recently viewing many biological features using amplitude or fluorescence contrast required staining and thereby killing the specimen. Even with the advent of green fluorescent protein, the act of viewing a specimen using a microscope may have additional biological side–effects (Jacquet et al., 2003).

As phase and polarisation imaging techniques evolved to become easier and more powerful, biologists were able to use them to view previously invisible specimen features in living cells. For example, a pioneering time–lapse movie of chromosomes dividing was taken using Zernike phase contrast shortly after the technique was commercialised in the 1950's (Bajer and Molè-Bajer, 1956; Inoué and Oldenbourg, 1998).

Phase imaging is also useful when combined with fluorescence, as often only certain features within a cell will fluoresce, so that a phase image acts as a backdrop showing key non-fluorescent features such as the nucleus and the cell walls. The ability to see microtubules moving chromosomes around during cell division provides an interesting example of the impact on biological research of new microscopy imaging modes (Waterman-Storer, 1998; Inoué, 2003).

1.3.1 Methods for phase imaging

Phase imaging is an ambiguous concept that bears careful definition. By comparison, brightfield imaging of specimen amplitude contrast is relatively straightforward, and is thus a helpful place to start when describing the imaging process.

Refractive index changes in the specimen will give spatial changes in absorption, transmittance and reflectance. Taking the case of brightfield transmission imaging, we would like to image the transmittance of the specimen in the focal plane. Assuming weak scattering in the specimen, the intensity of the electric field in the image plane will be proportional to the transmittance of the specimen. Conveniently, we can then record the intensity directly by converting photons into digital readings using a CCD camera.

But there may be features we wish to observe which change the refractive index or specimen thickness without significantly changing the transmittance. Such changes will introduce variations into the optical path length of the incident light. Assuming weak scattering in the specimen once more, these path length variations will translate into phase variations of the electric field in the image plane.

There is no equivalent solid state device to the CCD camera for recording the phase of an electric field. So we must use more indirect optical methods. The image field can be probed to retrieve the image phase. Alternatively, the imaging system can be modified so that the image intensity reveals information about the object phase. In both cases the key methods are interference and phase shifting.

We can use Fourier optics to model many possible modifications to the imaging system which convert object phase into image intensity (Sheppard and Wilson, 1980; Streibl, 1985). But fundamentally, Fourier optics points to a key limitation of lens system modifications for revealing phase. If we break up an object field $f(x)$ into real and imaginary parts $f = a + \mathrm{i}b$ and Fourier transform, then the corresponding real and imaginary parts remain separated as linear terms in Fourier space

$$a + \mathrm{i}b \Longleftrightarrow A + \mathrm{i}B \,, \tag{1.4}$$

where capitalisation denotes a Fourier transformed function. However the object magnitude and phase of the same function $f = r\exp(\mathrm{i}\phi)$ cannot be so easily untangled in Fourier space

$$r\exp(\mathrm{i}\phi) \Longleftrightarrow R \otimes \mathcal{F}\{\exp(\mathrm{i}\phi)\} \,, \tag{1.5}$$

where $\mathcal{F}$ denotes Fourier transformation and $\otimes$ denotes convolution. This means there is no simple way to apply a pupil function separately to the magnitude and phase information from the object field.

Nevertheless, many phase imaging methods rely on pupil modifications. In Zernike phase contrast (Born and Wolf, 1999) the DC component of the image is flipped by adding a phase mask in the pupil. For small optical path length changes, this gives an approximately linear phase response in the image intensity. However, for objects with non-uniform amplitude, the amplitude signal will be combined with the phase signal. Zernike phase contrast displays strong halo and shading–off artefacts, where the image intensity decays to the mean intensity level within any large area of constant phase.

We may think of the image signal being separated into parts by the act of diffraction by the specimen. By blocking the undiffracted part with various pupil masks, we can make visible the scattering caused by refractive index boundaries. This principle applies to various methods of phase imaging, including darkfield, schlieren phase imaging, Zernike phase contrast, and Hoffman modulation contrast (Pluta, 1989).

The schlieren and Hoffman techniques both give images of the phase gradient in the specimen, rather than the phase. This phase gradient is a partial derivative in a transverse direction, with the axis of differentiation set by the rotation of the anisotropic optical ele-

ments which produce the phase gradient contrast. The resulting image has a raised *bas relief* appearance. Differential phase contrast also produces a directional phase gradient, taking advantage of the access to the image spot provided by a confocal microscope to differentiate the image at the detector (Hamilton and Sheppard, 1984; Amos et al., 2003).

One particularly popular phase gradient imaging technique is Nomarski DIC (Pluta, 1989). This popularity reflects several strengths of DIC:

- the entire aperture of the objective is used, leading to high resolution and light efficiency,
- the derivative nature of DIC provides a boost in the contrast of high spatial frequencies in phase objects, and
- the derivative also gives very strong optical sectioning for phase features.

DIC achieves phase contrast by splitting the illumination into two orthogonally polarised beams, which interact independently with the specimen. By recombining these beams after the objective, the phase derivative can be measured. The details of DIC operation and theory are given in chapter 6. DIC still has its flaws: the phase signal is mixed with amplitude contrast, the phase is not entirely linear, and the phase gradient is anisotropic.

Despite the fact that it did not address any of these flaws, video enhanced DIC provided an important boost in the power of DIC for imaging biological features (Inoué, 1981; Allen et al., 1981). This technique forms a kind of digital microscope, as it side–steps the normal adjustment of DIC bias for optimal viewing by the eye, instead optimising the image contrast for later image processing (Salmon and Tran, 1998). This enabled viewing of microtubule dynamics, which was previously invisible with DIC as microtubules only give a slight change in refractive index, and they are very thin — as small as 25 nm in diameter (Inoué, 1989).

As discussed in chapter 6, DIC can be modelled using Fourier optics with a complex pupil function. In order to eliminate the amplitude signal and retrieve a linear phase signal, pupil modifications are not enough, we need to also perform some sort of optical phase shifting. Phase shifting implies a post-processing step of some kind, which means we have arrived at a full hybrid optical–digital microscope.

A new recipe for using DIC as part of a full hybrid digital microscope system to extract a linear isotropic phase is proposed and simulated in chapter 7. A review of alternative methods for using DIC to retrieve phase images rather than phase gradient images is given in section 6.2.

Recently two highly computational methods for phase retrieval have emerged. The first is based on one of the simplest ways to observe phase, which is to defocus slightly. It turns out that using the transport of intensity equation, an axial derivative recorded using a pair of defocused images can be used to retrieve a linear phase image (Paganin and Nugent, 1998). This is, in effect, a kind of phase shifting, as defocus may be modelled as a quadratic phase factor in the pupil plane, which has interesting implications for Fourier analysis of phase imaging (Barone-Nugent et al., 2002; Sheppard, 2002).

A second computational phase retrieval technique takes this kind of defocus phase shifting even further, by requiring a full 3D measurement of the intensity PSF. Once that is recorded, it can be 3D Fourier transformed to measure the pupil, where all the data should lie within the cap of a spherical shell (see chapter 3). By using this constraint together with the constraint that the image intensity must match what was recorded, this computational adaptive optics technique bounces back and forth between the PSF and the pupil to converge towards a complex PSF and complex pupil function (Hanser et al., 2001, 2003). This of course delivers both the PSF phase and the pupil phase.

Hanser et al. (2002) later applied this to the computational correction of spherical aberration in fluorescence microscopy, where small changes in refractive index or coverslip thickness can cause major imaging artefacts. A related technique used DIC to retrieve the specimen phase in order to improve the deconvolution of fluorescence images (Kam et al., 2001).

These last methods all involve significant optical modification in order to facilitate subsequent digital operations. They can all be clearly categorised as examples of the most highly evolved form of digital microscope, the hybrid optical–digital microscope.

1.4 Road map for this thesis

To take full advantage of the digital microscope, we should look at the information processing capabilities of each component. Adding any optical or digital element may produce both good and bad effects, but by keeping the whole system in mind, we can balance out the different components to arrive as close as possible to our imaging goal.

In order to fully explore high resolution digital microscopy, we need to relax some of the traditional constraints within optical imaging models. One example is radial symmetry, which makes sense for most optical components but cannot be assumed in the digital domain. Another is the assumption of small phase changes across the lens pupil, which is normal when striving for a traditional perfect focus but is no longer taken for granted for hy-

brid digital systems. Relaxing assumptions in this way makes more options available when assembling hybrid designs.

This thesis presents new theoretical work in 3D Fourier optics which can be used to help predict the performance of arbitrary pupil masks within a high resolution digital microscope (chapter 3). I then investigate theoretically and experimentally a digital microscope which uses phase control in the form of wavefront coding to create high resolution extended depth of field images (chapter 4 and chapter 5). Finally I propose a new form of digital phase microscope, which uses DIC, phase shifting and post-processing to measure the phase of a specimen (chapter 7).

The next chapter sets out the relevant accepted microscopy theory, before I begin presenting novel work in chapter 3.

Chapter 2

High aperture lens theory

High aperture lens theory is an active frontier of optics research. This means that careful consideration of assumptions and approximations is essential to place one's work in the context of evolving theories. In this chapter I begin with the Helmholtz equation and drill down through the most important constraints imposed by high aperture imaging to arrive at the theory used as a basis for this thesis.

2.1 Electromagnetic waves

It can be shown from Maxwell's equations that, in the absence of charges, an electromagnetic field $\mathbf{E}$ in an isotropic homogeneous medium must satisfy the Helmholtz wave equation of the form (Born and Wolf, 1999; Gu, 2000; Jackson, 1962; Stamnes, 1986)

$$(\nabla^2 + k^2)\mathbf{E} = 0\,, \tag{2.1}$$

where $k = nk_0 = n2\pi/\lambda_0$ is the wave number in a material of refractive index n, and k_0 and λ_0 are the vacuum wave number and wavelength respectively. We note that in Eq. (2.1) the Cartesian components of $\mathbf{E} = (E_x, E_y, E_z)$ can be decoupled and thereby solved independently.

The solutions of Eq. (2.1) are linear superpositions of electromagnetic waves in simple harmonic motion. We can write such waves with electric **e** and magnetic **h** vectors as the real parts of complex exponentials

$$\begin{aligned} \mathbf{e}(\mathbf{x},t) &= \Re\left[\mathbf{E}(\mathbf{x})\mathrm{e}^{-\mathrm{i}\omega t}\right] && (2.2)\\ \mathbf{h}(\mathbf{x},t) &= \Re\left[\mathbf{H}(\mathbf{x})\mathrm{e}^{-\mathrm{i}\omega t}\right] , && (2.3) \end{aligned}$$

where $\mathbf{x}$ is a position vector, t is time, $\Re$ denotes the real part, $\mathbf{E}$ and $\mathbf{H}$ are the complex position–dependent parts of the vectors, and ω is the angular frequency. By Maxwell's equations, the magnetic field can always be deduced once the electric field is known, so we consider only electric field from now on. We also drop any explicit mention of the time-dependent part $\mathrm{e}^{-\mathrm{i}\omega t}$ as it is superfluous in our descriptions of steady state fields.

A generic electric field vector with amplitude $\mathbf{E}_0$ and phase ϕ is then written as

$$\mathbf{E}(\mathbf{x}) = \mathbf{E}_0(\mathbf{x})\mathrm{e}^{\mathrm{i}\phi(\mathbf{x})} , \tag{2.4}$$

with the special case of a plane polarised wave

$$\mathrm{e}^{\mathrm{i}\mathbf{k}\cdot\mathbf{x}} \tag{2.5}$$

propagating in the direction of the wave vector

$$\begin{aligned} \mathbf{k} &= (k_x, k_y, k_z) && (2.6)\\ &= k\mathbf{m} \end{aligned}$$

where $\mathbf{m} = (m,n,s)$ is a Cartesian unit vector. A spherical wave is written as

$$\frac{\mathrm{e}^{\mathrm{i}kr}}{r} , \tag{2.7}$$

where r is the distance from the origin of the wave. These formulations assume a quasi–monochromatic wave, which allows subsequent integration over wavelength for the polychromatic case if needed. Electronic and biological detectors respond to the intensity of the electric field

$$I = |E_x|^2 + |E_y|^2 + |E_z|^2 . \tag{2.8}$$

Both spherical and planar waves are idealisations which can never actually exist. The basic unit of physical electromagnetic radiation is a dipole wave, created by an oscillating point charge. However, for many situations planar and spherical waves are useful approximations.

2.2 Vectorial focusing and point spread functions

Imaging fine details in a microscope requires a lens with high magnification, high resolution and low aberrations. A standard spherically shaped lens falls well short. In order to construct a high numerical aperture objective, manufacturers must work towards perfect focusing with several different lenses within the housing, all in delicate balance. Modelling such an objective would be complicated enough if we knew the details of their construction, but generally they are trade secrets. Instead, high aperture lens theory assumes the lens is a black box which can produce a perfect focus. Any deviations from this behaviour are modelled as aberrations from the perfect lens.

This still leaves a crucial question: what is a "perfect" focus? It is defined as the conversion of an electromagnetic plane wave, incident on the back pupil of the lens, into a spherical wave converging on the focal point. In order to have an incident plane wave, we are assuming the source of the radiation is very far away, which in optical terms means a distance much bigger than the wavelength of the light. We can then predict the electromagnetic field in the focal region by modelling the way the spherical wave diffracts from the edges of the lens pupil and propagates towards the focal plane. The importance of the diffraction effect is emphasised when a perfect focus is termed "diffraction limited" meaning that aperture diffraction and the wavelength of light place the most important limits on the size of the peak intensity spot at focus.

Huygens' principle, which may of course be re-derived from Maxwell's equations, is that an electromagnetic wave propagates using spherical wavelets. Kirchhoff used this principle to solve the Helmholtz wave equation for a wave passing through an aperture considered to be large with respect to the wavelength. The solution uses Green's theorem to convert a volume integral solution of Eq. (2.1) into a surface integral. Doing this requires choosing a Green's function. Using spherical waves in the form of Eq. (2.7) implements Huygens' principle. Each point on the aperture is a source of spherical waves.

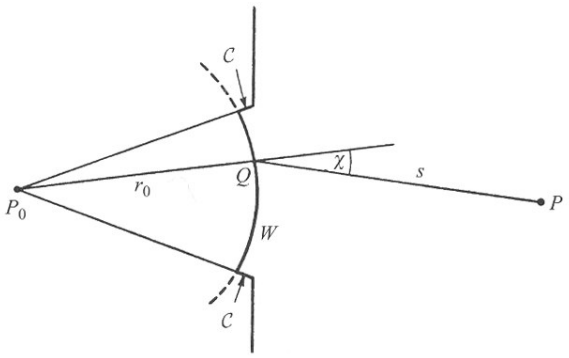

Figure 2.1: Geometry for the Fresnel–Kirchhoff diffraction integral in Eq. (2.9). P_0 is the source point of a spherical wavefront W with radius r_0 incident on an aperture. We integrate over surface elements S of the aperture to find a scalar approximation U of the electric field at the observation point P. For this figure and Eq. (2.9) only, s is the distance QP. If r_0 is large then the contribution from $\mathcal{C}$ can be neglected. Reproduced from Born and Wolf (1999).

The Fresnel–Kirchhoff integral for diffraction through an aperture is simple to express (Born and Wolf, 1999, p. 423)

$$U(P) = -\frac{\mathrm{i}k}{4\pi}\frac{\mathrm{e}^{\mathrm{i}kr_0}}{r_0}\int\int_W \frac{\mathrm{e}^{\mathrm{i}ks}}{s}(1+\cos\chi)\mathrm{d}S\,, \tag{2.9}$$

yet computationally time-consuming to solve. The geometry and notation are shown in Fig. 2.1. By moving the source point P_0 to the right of the aperture, making r_0 negative, we can use this equation to model a spherical wavefront with focal length r_0 converging to focus at P_0.

The Fresnel–Kirchhoff diffraction integral was later simplified by replacing the spherical wavelets with plane waves by Debye (1909) for scalar waves and by Wolf (1959) for the vectorial electromagnetic case. The wavelet approximation is illustrated in Fig. 2.2. This model is often called the angular spectrum of plane waves. The approximation to plane waves is valid when the observation and focal points are both a long way from the aperture, and for apertures much larger than the wavelength. This is equivalent to requiring a high Fresnel number

$$N = \frac{a^2}{\lambda R} \gg 1\,, \tag{2.10}$$

where a is the aperture radius and R is the distance from the aperture to the observation point. This relation is generally true for microscope imaging. For example, a Zeiss Plan-NEOFLUAR 40× 1.3 NA oil immersion lens has a back pupil radius of 5 mm and a focal

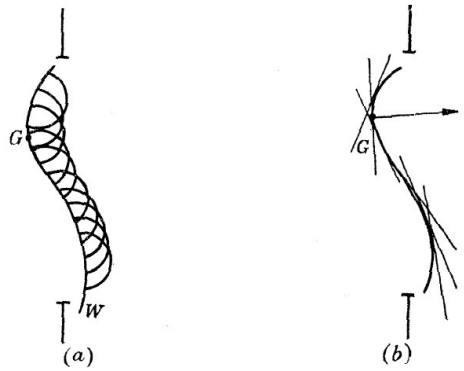

Figure 2.2: The Debye approximation replaces (a) spherical secondary wavelets with (b) planar secondary wavelets, propagating from each point G on the primary wave W. Reproduced from Wolf (1959).

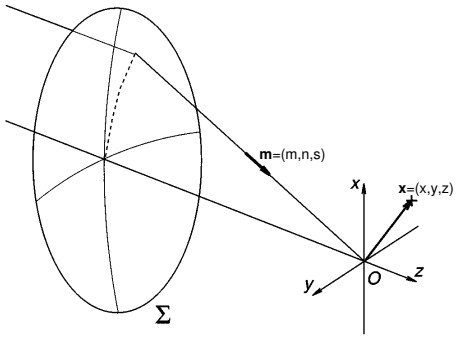

Figure 2.3: Diagram of the light focusing geometry used in calculating the vectorial PSF, indicating the focal region co-ordinate $\mathbf{x}$ and the pupil co-ordinate $\mathbf{m}$, the latter of which may also be thought of as a unit vector aligned with a ray from the pupil Σ to the focal point O.

length of 4.1 mm. For $\lambda = 550$ nm the Fresnel number in the focal region is $N \approx 11\,000$. On the other hand, if the pupil is in the back focal plane of the lens, then $N = \infty$ (Sheppard and Török, 1998). When designing high NA objectives it is difficult to place the aperture stop exactly at the back focal plane, and in addition the opening at the rear of the objective housing is usually not the actual aperture stop of the objective. Effectively $N \approx 11\,000$ is a lower bound on the Fresnel number of this lens.

Richards and Wolf (1959) used the Debye–Wolf approximation to calculate the field in the focal region of a high aperture lens

$$\mathbf{E}(\mathbf{x}) = -\frac{\mathrm{i}k}{2\pi} \int\int\int \mathbf{Q}(\mathbf{m}) \exp(\mathrm{i}k\mathbf{m}\cdot\mathbf{x}) \mathrm{d}\mathbf{m}\,, \tag{2.11}$$

where $\mathbf{x}$ is the observation point with the co-ordinate origin at the focal point, and $\mathbf{Q}(\mathbf{m})$ is the vectorial pupil function (McCutchen, 1964). The basic geometry is shown in Fig. 2.3. The vectorial pupil describes the state of the wavelets across the exit pupil of the lens, which is constrained to a spherical surface by Eq. (2.1). This spherical surface is known as the Ewald sphere. This pupil incorporates many important features of high aperture focusing, including:

- the 2D field across the entrance pupil of the lens at the back focal plane;
- aberrations from spherical focusing expressed as phase functions across the pupil;
- apodisation as necessary to provide aplanatic focusing; and
- polarisation scrambling: if the incident light is linearly polarised, significant energy is shunted into an axially polarised component.

The angular aperture of the lens cuts off the pupil function at an angle α from the optical axis, forming a cap of a sphere. The angular size of this cap limits the spatial frequencies which the lens may pass, and is related to the numerical aperture NA by

$$\sin\alpha = \frac{\mathrm{NA}}{n} \,. \tag{2.12}$$

The vectorial pupil is described in detail in section 3.1. Richards and Wolf (1959) demonstrated that the Debye–Wolf integral diverges from the paraxial approximation for apertures higher than about 0.5 NA in air, or 0.7 NA for oil immersion objectives.

We refer to the electric field $\mathbf{E}(\mathbf{x})$ in the focal region as the point spread function (PSF), which may denote either the complex amplitude or the intensity of $\mathbf{E}(\mathbf{x})$ depending on the context. Aberrations, such as spherical aberration introduced by a change of refractive index as the light passes through the coverglass into a watery specimen, may introduce significant shifts of the peak intensity away from the co-ordinate origin (Török et al., 1997). For this reason we term the geometrical centre of the focal sphere the Gaussian focal point,* or simply the focal point. This phrase denotes the fixed co-ordinate origin, as distinct from the variable location of the peak intensity. We refer to the volume around the focal point as the focal region.

*Gaussian in this context refers to a first order approximation to the focus position. Gauss' name is also used in optics to refer to beams with a Gaussian function as their intensity profile. This thesis does not discuss Gaussian beams.

Confirming this vectorial focusing theory by accurately measuring high NA PSFs is no trivial task. We say that the ideal PSF has a focal spot which is "diffraction limited" meaning that the most important limits on the size of the spot are the nature of electromagnetic diffraction and the wavelength of the light. Measurement of the PSF is subject to the same limits.

Low resolution images of a high NA intensity PSF were measured by Gibson and Lanni (1991) using 50 nm fluorescent beads. Schrader and Hell (1996) used a Twynam–Green interferometer to measure the PSF of a 1.4 NA lens and compare with Eq. (2.11). However, their measurement result was an interference pattern, rather than the intensity and phase of the complex field $\mathbf{E}$. An alternative approach to interferometry achieved high resolution images of the amplitude and phase of the high NA PSF, albeit without considering polarisation effects (Juškaitis and Wilson, 1998; Juškaitis, 2003). Rhodes et al. (2002) measured a high NA intensity PSF using a tapered fibre as a near-field probe, obtaining separate xz and yz sections which compared well with vectorial theory.

Bahlmann and Hell (2000) imaged the polarisation components of the PSF using a layer of fluorescent molecules with fixed dipole axes and found the behaviour matched theoretical predictions. Important applications of the polarised PSF are in polarisation microscopy as used to observe the anisotropy (birefringence) of biological features (Inoué, 2003; Oldenbourg and Török, 2000), and z-polarised confocal microscopy for probing the dipole axes of fluorescent materials (Huse et al., 2001).

2.3 Scattering, fluorescence and image contrast

To form an image, we rely on interactions between an incident focused electromagnetic field and the specimen. We can break up the specimen into tiny regions or particles, and then describe the scattering of the incident field from each particle. However, in general, light scattered once may then interact with a second particle and be scattered again. If we have a weakly scattering semi–transparent specimen, then we can concentrate on just the first scattering interaction, and assume that secondary scattering is negligible. This is known as the first order Born approximation, which was inherited from quantum mechanics. This allows us to treat interaction with the specimen as a linear system, which has important implications for Fourier analysis.

We follow the scalar derivation of the optical Born approximation used in Wolf (1969), together with vectorial extensions (Nieto-Vesperinas, 1991; Rohrbach and Stelzer, 2001). From Maxwell's equations it can be shown that an electromagnetic field $\mathbf{E}(\mathbf{x})$ in a region

without charges must satisfy the vectorial Helmholtz wave equation (Born and Wolf, 1999, p. 696 Eq. (3))

$$\nabla^2\mathbf{E}(\mathbf{x}) + n(\mathbf{x})k_0^2\mathbf{E}(\mathbf{x}) = 0\,, \tag{2.13}$$

where $n(\mathbf{x})$ is the specimen refractive index (which may be complex for absorbing materials). This assumes that the specimen region is isotropic with respect to the polarisation direction of the electric field, non-dispersive, and non-magnetic. We also assume that $n(\mathbf{x})$ varies slowly so that it is effectively constant over distances of the order of a wavelength. Finally, we assume the immersion and specimen material is linear.

Assuming the scattered field $\mathbf{E}_s$ is much weaker than the incident field $\mathbf{E}_\mathrm{m}$, and that the refractive index gradient is small throughout the specimen, then we model the scattered field as a perturbation on the incident field, giving for the total field

$$\mathbf{E}(\mathbf{x}) = \mathbf{E}_\mathrm{m}(\mathbf{x}) + \mathbf{E}_\mathrm{s}(\mathbf{x})\,. \tag{2.14}$$

In this model the incident field sees only a constant refractive index n_m. We then obtain a modified Helmholtz equation

$$(\nabla^2 + k_\mathrm{m}^2)\mathbf{E}_\mathrm{s}(\mathbf{x}) = \left[k_\mathrm{m}^2 - k_0^2 n(\mathbf{x})^2\right]\mathbf{E}(\mathbf{x})\,, \tag{2.15}$$

where $k_\mathrm{m} = n_\mathrm{m}k_0$. We define the scattering potential as

$$V(\mathbf{x}) = \left[k_\mathrm{m}^2 - k_0^2 n(\mathbf{x})^2\right]\,, \tag{2.16}$$

which describes the sample's interaction with the incident field. Now assuming that the scattered field is much weaker than the incident field $|\mathbf{E}_\mathrm{s}| \ll |\mathbf{E}_\mathrm{m}|$, we can apply the Born approximation to first order (Arfken and Weber, 1995, p. 521)

$$\mathbf{E}_\mathrm{s}(\mathbf{x}) \approx \int_\text{specimen} V(\mathbf{x}')\mathbf{E}_\mathrm{m}(\mathbf{x}')G(|\mathbf{x}-\mathbf{x}'|)\mathrm{d}\mathbf{x}'\,. \tag{2.17}$$

The Green's function used here is a spherical wave

$$G(r) = \frac{\exp(\mathrm{i}k_\mathrm{m}r)}{4\pi r}\,. \tag{2.18}$$

Equation (2.17) is linear and shift-invariant with respect to the incident field and the scattering function. This means that we can think of specimen imaging under the Born

approximation as a linear system. The next step usually taken in modelling imaging is to define an object transmittance function

$$O(\mathbf{x}) = A_{\text{obj}}(\mathbf{x})\mathrm{e}^{\mathrm{i}\phi_{\text{obj}}(\mathbf{x})}\,, \tag{2.19}$$

with an amplitude A_{obj} component corresponding to the ratio of transmitted light to incident light and a phase component ϕ_{obj} corresponding to the optical path difference between the incident and transmitted light. The transmitted light is the sum of the incident and scattered field as given in Eq. (2.14).

Physically we know that the scattered field is 90° out of phase with the incident field. This is because when a system is stimulated into resonance, there is a 90° shift between the phase of the stimulation signal and the resonance vibration. This phase shift is crucial to imaging as it explains why changes in the *imaginary* (absorbing) part of the specimen refractive index give contrast in the *real* part of the image field. It also explains why variations in the real part of the object transmittance $O(\mathbf{x})$ give more image contrast in a standard system: if the scattered field is mostly real, then mathematically a small real addition to E will have a greater impact on the intensity $|E|^2$ than a small imaginary addition. However, this factor of i between the two fields is rarely explicitly shown in the literature.

Focusing also produces an i phase shift, evidenced by the i factor out the front of Eq. (2.11), as the far-field of a spherical wave is 90° out of phase with the centre. However, both the incident and scattered fields go through the same objective and detector lenses, so they will both undergo the same focusing phase shifts.

As noted in section 1.3.1, the Fourier nature of Eq. (2.11) means there is no straightforward way to separate the magnitude and phase signals for an observation point without some sort of phase shifting involving multiple recordings.

In fluorescence imaging, the contrast mechanism is of course quite different. Dipoles within the dye molecules are excited by the incident field at their resonant wavelength, and the excited dipoles emit radiation at a different wavelength. Török and Sheppard (2002) discussed the effects of the polarisation of the incident field and identified four cases:

1. Induced dipole, unpolarised emission. The dipole is excited by the total incident field, and the emission dipole axis is randomly oriented giving unpolarised emission.

2. Permanent dipole, unpolarised emission. The dipole is excited only by the component of the incident field parallel to the permanent dipole moment. As for the previous case the emission dipole axis is randomly oriented.

3. Induced dipole, polarised emission. The dipole is excited by the total incident field, and the emission dipole axis is in the same direction as the incident field.

4. Permanent dipole, polarised emission. The dipole is excited only by the component of the incident field which is parallel to the dipole's permanent axis, and the emitted radiation pattern has a fixed dipole moment.

For single photon excitation, the probability of excitation is given by the intensity I_d of the relevant component of the incident electric field as described in each case above. For multi-photon fluorescence, the probability is I_d^N where N is the order of the multi-photon process, such as $N = 2$ for two-photon.

An example of fixed dipole fluorescence (cases 3 and 4) from crystals of green fluorescent protein is described by Inoué et al. (2002), while Bahlmann and Hell (2000) used fixed dipoles to measure the vectorial PSF.

If the dipole can freely rotate between excitation and emission (cases 1 and 2), then the image in a confocal fluorescence microscope is the same as for an isotropic point object (Sheppard and Török, 1997b). For a weak fluorescent object, such as a thin specimen, we can assume in cases 1 and 2 that the incident field for any region within the specimen is unaffected by the object. For this particular situation, we can use a linear imaging model within the vectorial theory.

While providing linear imaging behaviour, both this weak fluorescence model and the Born approximation (Eq. (2.17)) ignore multiple interactions. This neglects important factors which commonly occur in microscope imaging of thick objects, such as depth shadowing where deeper regions of the specimen receive less excitation. As with all approximations, any conclusions reached using their help must be handled with care.

2.4 3D Fourier optics

The Debye–Wolf angular spectrum integral Eq. (2.11) is a 3D Fourier transform. This fortuitous property allows a vast array of analytical and numerical tools to be applied directly to the problem of high aperture focusing.

The Helmholtz equation Eq. (2.1) means that the vectorial pupil $\mathbf{Q}$ of the Debye–Wolf equation is constrained to the 2D surface of the cap of a sphere, with the angular extent of the cap prescribed by the angular aperture of the lens α (see section 3.1 for details of the geometry of $\mathbf{Q}$). We can generate the field in the focal region from the 3D Fourier transform of a 2D surface (McCutchen, 1964). This is the basis of 3D Fourier optics.

In practice we only need to evaluate a 2D Fourier transform, because the surface delta function in $\mathbf{Q}$ sifts out the third dimension in the integral. It is by taking account of the curvature of the pupil function that 3D Fourier optics remains accurate at high apertures.

Fourier optics is more commonly known in its 2D paraxial incarnation (Goodman, 1968), where α is assumed to be small and therefore the cap of the sphere is approximately flat. A further simplification used in 2D paraxial Fourier optics is the scalar approximation, where the effects of polarisation of the electric field are assumed to be negligible, so that the electric field can be represented by a single complex field component E instead of a triplet (E_x, E_y, E_z).

Returning to 3D vectorial Fourier optics, the curvature of the pupil can be taken into account using a simple amplitude modification of the pupil function. The vectorial nature of focusing and aplanatic apodisation are also described using a modification of the 2D pupil surface function. As with 2D Fourier optics, any amplitude or phase filters placed into the back focal plane of the lens can be modelled using pupil functions.

Taking things a step further, many other imaging characteristics can be incorporated into a 3D Fourier optics model by describing their effects in frequency space and then modifying the pupil function. In their vectorial treatment of a planar change in refractive index, Török et al. (1995) pointed out that the required pupil modifications are consistent with an angular spectrum model.

Rohrbach and Stelzer (2001, 2002a) extended this Fourier approach to model optical trapping of small spherical particles. Their pupil function included the dipole pattern of specimen response, Born approximations to first order (single scattering) and second order (multiple scattering), and Mie scattering.

These 3D Fourier optics approaches are valid without assuming linear specimen imaging, with Fourier space modelling of secondary scattering a potent example (Rohrbach and Stelzer, 2001, 2002a).

2.4.1 Transfer functions

The performance of a linear, space-invariant imaging system when imaging weakly scattering objects is usefully described by the transfer function. This specifies the imaging contrast for different spatial frequencies in the object. The coherent transfer function (CTF) is simply the pupil function, as in coherent linear imaging the scattered field relies on the complex field in the focal plane. For incoherent linear imaging, the image is derived from the convolution

of the intensity PSF with the object. The Fourier transform of the intensity PSF is termed the optical transfer function (OTF).

By determining the system OTF, together with a model for the response of the object to incident light, we can build up a model for the system as a whole. Transfer functions for each optical component can be multiplied to give an overall system transfer function, which can be multiplied with the object spectrum and inverse Fourier transformed to calculate the expected image.

Even if the system is not weakly scattering (as described in section 2.3), and is therefore non-linear, the Fourier transform of the intensity PSF is a useful measure of incoherent focusing performance, and is often still termed the OTF. In such cases the 3D OTF describes the action of a lens in terms of spatial frequencies in the 3D PSF produced at the focus. An alternative label for the 3D OTF in non-linear cases is the intensity spectrum (Streibl, 1984b).

Maximising the performance of high resolution microscopy requires increasingly accurate models for the high numerical aperture lenses used, for the effects of their apodisation functions, and for any aberrations introduced by the specimen. Vectorial theory for the accurate calculation of the high aperture PSF has been available for a long time (Ignatowsky, 1919, 1920; Richards and Wolf, 1959). Yet despite the popularity of Fourier optics for modelling low aperture systems, the field of high aperture vectorial transfer functions remains relatively unexplored.

Frieden (1967) first derived the scalar 3D OTF as an autocorrelation using the paraxial approximation. This autocorrelation provides a method for calculating the OTF directly from the pupil function. This is much simpler than first obtaining the PSF and then performing a Fourier transform — especially in 3D.

Frieden's work was extended by Sheppard et al. (1994) to cover the scalar high numerical aperture case by explicitly avoiding the paraxial assumption. This work derived analytical expressions, assuming cylindrical symmetry in the pupil function. However, modelling arbitrary aberrations and pupil functions, and indeed using a vectorial approach taking account of the asymmetry of incident polarised light, requires a more general non-cylindrical model. Sheppard and Cogswell (1990) and Gu (2000) provide good overviews of high aperture scalar 3D transfer function theory.

An alternative approach is to calculate the autocorrelation as a multiplication in Fourier space, as shown in Fig. 2.4, allowing the use of the fast Fourier transfer (FFT) algorithm. This method was applied to vectorial pupil functions by Sheppard and Larkin (1997), resulting in a vectorial OTF. This is a useful method, especially for 2D projections. However calculation

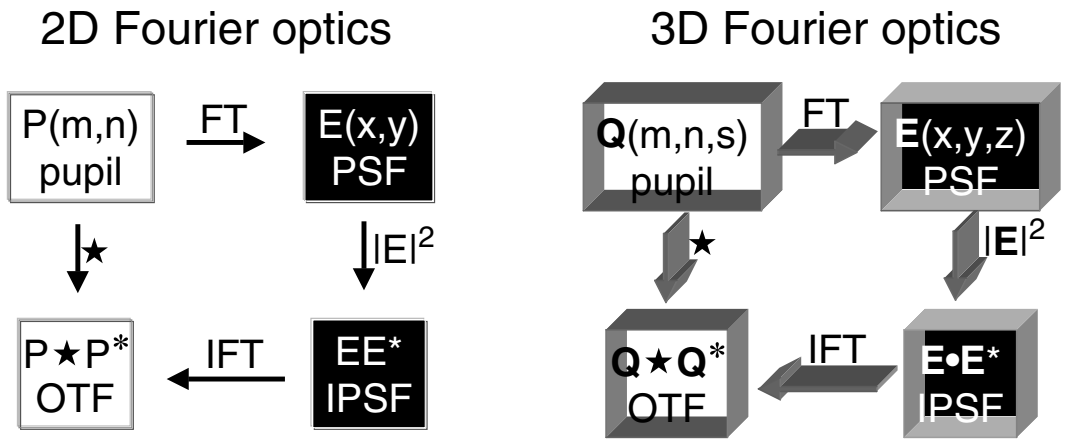

Figure 2.4: Using Fourier optics to move between the pupil function, the PSF, the intensity PSF (IPSF), and the OTF for incoherent linear imaging.

using 3D FFTs would be awkward, delicate and time consuming due to the need for careful consideration of sampling issues, accuracy and the large 3D arrays required.

A vectorial OTF was also presented by Urbańczyk (1986), but the analysis was restricted to a 2D transverse OTF for low angle systems. The earliest mention of an incoherent scalar OTF with an axial dimension was by Mertz (1965, pp. 101–102).

Streibl (1984a,b) developed a 3D intensity spectrum based on partially coherent imaging theory. He noted that a 3D OTF is useful for describing incoherent imaging of weak fluorescent objects. For a weak phase object, he used a partially coherent version of the Born approximation to develop transfer functions for amplitude and phase (Streibl, 1985). All of the results plotted relied on the paraxial approximation.

Experimentally measured high aperture pupil functions and OTFs have recently been used to analyse the performance of advanced digital microscope designs. Gustafsson et al. (1999) used high NA OTFs to characterise their structured illumination fluorescent microscope, for which Fourier optics provides the conceptual building blocks in engineering a sevenfold increase in resolution. Gustafsson (1999) also used OTFs to great effect in a review comparing various recent methods for increasing resolution. Heintzmann et al. (2001) used experimental OTFs to describe an epi-fluorescence microscope with a micro–electro–mechanical systems (MEMS) array of mirrors in the pupil plane.

Hanser et al. (2003) described a phase retrieval method which relies on the spherical surface shape of the high aperture pupil. The spherical surface was applied as a constraint on the Fourier transform of their image intensity measurements. Using iterative convergence they determined both the complex pupil function and the complex PSF.

All of these experimental methods use scalar OTFs, however Hanser et al. do propose an extension to the vectorial case.

Chapter 3 of this thesis extends the work presented in two papers by Sheppard et al. (Sheppard et al., 1994; Sheppard and Larkin, 1997), generalising where necessary to full 3D Cartesian co-ordinates, in order to avoid the assumption of radial symmetry. I use this extended model to chart the 3D structure of the vectorial OTF, and discuss the implications and potential uses.

Our original publication of this work (Arnison and Sheppard, 2002), which forms the basis of chapter 3, coincided with the independent development and publication of a vectorial OTF by Schönle and Hell (2002). Schönle and Hell used spherical polar co-ordinates rather than Cartesian, and also calculated the vectorial coherent transfer function for confocal reflection microscopy and a spherically aberrated vectorial OTF for a change in specimen refractive index based on the model presented by Török et al. (1995).

2.5 Imaging systems

So far in this chapter I have concentrated on the physics of focusing and scattering. While these lie at the heart of high aperture microscopy modelling, there are other important factors which should be addressed in order to form a model of a complete imaging system.

Coherence describes the strength of interference to be expected if waves from disparate points in the imaging system are brought together. Coherence can be categorised as either lateral or temporal.

Lateral coherence applies to an extended illumination source together with a finite condenser aperture. Laterally separated points within the extended source will in general be partially coherent. An infinitely small condenser aperture, a confocal pinhole, or a laser illumination source will all give laterally coherent illumination. If the phase of the scattered light from the specimen is independent of the incident phase, such as for fluorescence imaging, then the system is laterally incoherent. The most general case of partial lateral coherence requires an additional 2D convolution of the extended source with the lens pupil to calculate the PSF. Fourier optics is very useful for modelling partially coherent optics, as demonstrated for the 3D case by Streibl (1984b) among others.

In this thesis I use a laterally incoherent model for modelling fluorescence microscopy, and a coherent model for modelling DIC. The technique of wavefront coding relies on incoherent imaging to produce a focus invariant transfer function — the partially coherent behaviour of wavefront coding systems is yet to be explored. Although DIC microscopes

can be operated with closed condenser apertures, in general the best performance is obtained with a partially open condenser, meaning that a partially coherent model for DIC is more accurate.

Temporal coherence refers to the strength of interference between different axial positions on the wave-train. Laser light being quasi-monochromatic has very high temporal coherence, on the order of 1 m. A spectrum of wavelengths in the light will broaden the temporal bandwidth, with white light having a temporal coherence on the order of microns. Behaviour for broadband light fields can be determined from a monochromatic model by integrating over the wavelength range. Fluorescence microscopy filters select a narrow wavelength range and are therefore focusing is relatively coherent in temporal terms. Preza et al. (1999) discusses and tests the implications of temporal coherence for DIC phase imaging. Throughout this thesis I assume quasi-monochromatic light.

A related issue is the change of wavelength between the incident and emitted light in fluorescence. Modelling the focusing of a single lens does not require incorporation of this behaviour, but it would of course need to be taken into account for a full system description (Sheppard and Cogswell, 1990).

For the vectorial theory in this thesis, I assume the pupil field is linearly polarised. Partially polarised or unpolarised incident light could be modelled by integrating over the polarisation angle. For fluorescent microscopy, the beam splitter will produce elliptically polarised light, which I approximate as linearly polarised. The polarisation of the emitted fluorescence will depend on the nature of the dye molecules, as discussed in section 2.3.

The tools described in this chapter are the building blocks needed to construct a model of a full imaging system. Török et al. (1995; 2000) show how to use generalised Jones matrices to build up a full vectorial system model in real space, while Rohrbach and Stelzer (2002b) built a full vectorial system model in frequency space.

In this thesis I have largely restricted my investigations to the pupil function, the focused field, and the intensity spectrum. Cartesian co-ordinates are used to suit the rectangular nature of both the wavefront coding phase mask and the lateral DIC shear.

Fourier optics is used throughout this thesis in various ways. It is used as the domain for developing a vectorial OTF in chapter 3, and for reviewing the concepts behind wavefront coding in chapter 4. I develop a high aperture Fourier optics theory for wavefront coding, with its accompanying problems of very large phase aberrations, lack of radial symmetry, and long focal depth, all of which are unusual in high aperture focusing theory. Fourier optics is also used in chapter 5 to analyse the experimental performance of wavefront coding.

Developing and implementing the modified spiral phase transform used in chapter 7 relied fundamentally on a Fourier optics approach. Naturally, for the theoretical simulation of DIC I use Fourier optics once again.

Chapter 3

Vectorial optical transfer function

In this chapter I describe a method for calculating the vectorial OTF for an arbitrary pupil. Our approach is to extend the work presented in two papers by Sheppard et al. (Sheppard et al., 1994; Sheppard and Larkin, 1997), generalising where necessary to full 3D Cartesian co-ordinates, in order to avoid the assumption of radial symmetry. We present general descriptions of the vectorial lens pupil functions. This pupil function description is then used in an autocorrelation to form the vectorial optical transfer function (OTF).

This autocorrelation may be geometrically interpreted as the volume of overlap between two spherical shells. We derive general formulas for the volume of overlap, which do not assume radial symmetry, resulting in a single integral autocorrelation. This equation is straightforward, if time consuming, to calculate, and serves as a useful alternative to the Fourier transform method (Sheppard and Larkin, 1997). We then plot the vectorial OTF for various cases. Finally we discuss the implications and potential uses of a vectorial OTF.

3.1 Vectorial pupil function

The theory of Richards and Wolf (Wolf, 1959; Richards and Wolf, 1959) describes how to determine the electric field in the focal region of a lens which is illuminated by a plane polarised quasi-monochromatic light wave. Their analysis assumes very large values of the Fresnel number, equivalent to the Debye approximation. We can then write the equation for the vectorial PSF $\mathbf{E}(\mathbf{x})$ of a high NA lens illuminated with a plane polarised wave as the Fourier transform of the complex vectorial pupil function $\mathbf{Q}(\mathbf{m})$ (McCutchen, 1964),

$$\mathbf{E}(\mathbf{x}) = -\frac{\mathrm{i}k}{2\pi}\int\int\int \mathbf{Q}(\mathbf{m})\exp(\mathrm{i}k\mathbf{m}\cdot\mathbf{x})\mathrm{d}\mathbf{m}\,. \tag{3.1}$$

Here $k = 2\pi/\lambda$ is the wave number, λ is the wavelength, $\mathbf{m} = (m,n,s)$ is the Cartesian pupil co-ordinate, and $\mathbf{x} = (x,y,z)$ is the focal co-ordinate. The vectorial pupil function describes the effect of a lens on the polarisation of the incident field, the complex value of any amplitude or phase filters across the aperture, and any additional aberration in the lens focusing behaviour from that which produces a perfect spherical wavefront converging on the focal point.

Because we are describing the behaviour of electromagnetic waves, they must obey the Maxwell equations, giving an important constraint — the homogeneous Helmholtz equation for time-independent vectorial wave fields,

$$\nabla^2\mathbf{E}(\mathbf{x}) + k^2\mathbf{E}(\mathbf{x}) = 0\,, \tag{3.2}$$

assuming a constant refractive index in the focal region.

By expressing the Helmholtz equation in Fourier space, we can determine the electromagnetic constraints on the pupil function $\mathbf{Q}(\mathbf{m})$. Applying the Fourier relationship $\nabla^2\mathbf{E}(\mathbf{x}) \Leftrightarrow -|\mathbf{m}|^2\mathbf{Q}(\mathbf{m})$, we have

$$(|\mathbf{m}|^2 - k^2)\mathbf{Q}(\mathbf{m}) = 0\,, \tag{3.3}$$

which means that the pupil function is only non-zero on the surface $\mathbf{Q}_s(\mathbf{m})$ of a sphere with radius k,

$$\mathbf{Q}(\mathbf{m}) = \mathbf{Q}_s(\mathbf{m})\delta(|\mathbf{m}| - k)\,. \tag{3.4}$$

This is known as the Ewald sphere in the theory of X-ray diffraction (Ewald, 1916; James, 1965).

For a practical quasi-monochromatic wave, k cannot have purely a single value, so the spread of wavelengths in the illumination light gives a small finite thickness to the spherical shell. For this paper we examine the monochromatic case and assume a thin shell of thickness δk and take the limit $\delta k \to 0$.

Because the pupil function only exists on the surface of a sphere, we can slice $\mathbf{Q}(\mathbf{m})$ along the $s = 0$ plane into a pair of functions

$$\mathbf{Q}(\mathbf{m}) = \mathbf{Q}_s(\mathbf{m})\delta(s - \sqrt{k^2 - l^2}) + \mathbf{Q}_s(\mathbf{m})\delta(s + \sqrt{k^2 - l^2})\,, \tag{3.5}$$

representing forward and backward propagation. Here we have introduced a transverse radial co-ordinate $l = \sqrt{m^2 + n^2}$. Restricting our attention to the forward propagation case and

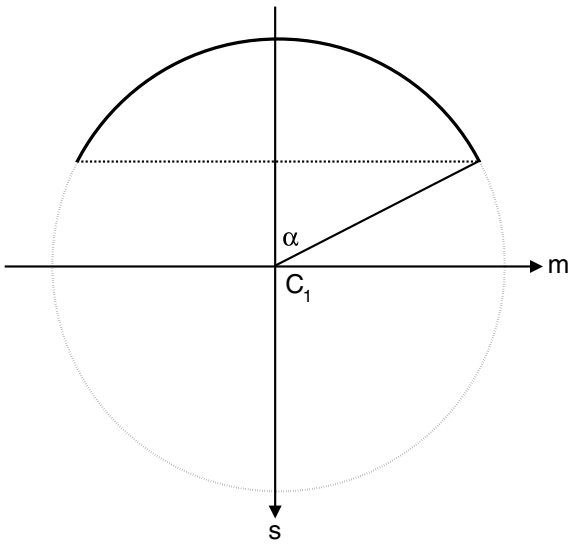

Figure 3.1: A cross-section through the pupil sphere in the (m,s) plane.

anticipating that the pupil function will later be integrated, we can define a 2D function for the value of the pupil on the surface of the sphere

$$\mathbf{P}_+(m,n) \quad = \quad \mathbf{Q}_\mathrm{s}(m,n,s_+)\,, \tag{3.6}$$

where we have normalised the radius to $k=1$ and indicated the constraint on s to the upper surface of the sphere with

$$s_+ = \sqrt{1-l^2}\,. \tag{3.7}$$

The aperture of the lens is represented by slicing a cap off the top of the sphere, as shown in Fig. 3.1. The angle α subtended by the cap at the centre of the sphere is related to the numerical aperture NA and the refractive index n of the imaging medium (such as air, water or immersion oil) by

$$\sin\alpha = \frac{\mathrm{NA}}{n}\,. \tag{3.8}$$

For incident light which is plane-polarised along the x axis, we can derive a vectorial strength function $\mathbf{a}(m,n)$, from the strength factors used in the vectorial point spread function integrals (Richards and Wolf, 1959; Mansuripur, 1986, 1993; Sheppard and Larkin, 1997)

$$\mathbf{a}(m,n) = \begin{pmatrix} (m^2 s_+ + n^2)/l^2 \\ -mn(1-s_+)/l^2 \\ -m \end{pmatrix} \tag{3.9}$$

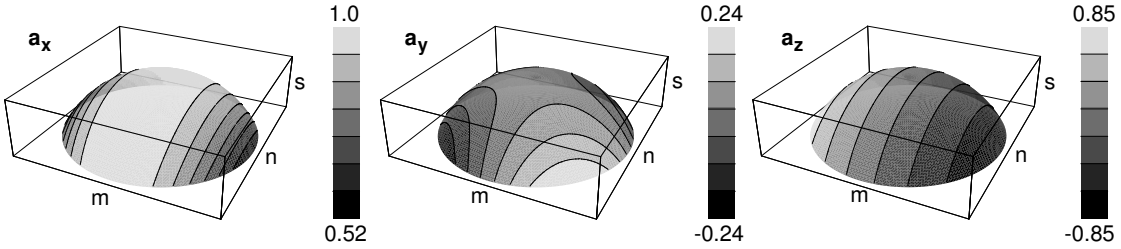

Figure 3.2: The vectorial strength factors $\mathbf{a}(m,n)$ for linearly polarised light propagating in the forward direction, mapped onto the spherical pupil caps, with $\alpha = \pi/3$. $\mathbf{a}(m,n)$ is shown split into its Cartesian components a_x, a_y, and a_z.

where we have converted from the spherical polar representation in Richards and Wolf to Cartesian co-ordinates. We show an example case for $\mathbf{a}(m,n)$ in figure 3.2, with $\mathbf{a}(m,n)$ split into its Cartesian components.

We can now model polarisation, apodisation and aperture filtering as amplitude and phase functions over the pupil cap,*

$$\mathbf{P}_+(m,n) = \mathbf{a}(m,n)S(m,n)T(m,n)\ , \tag{3.10}$$

representing forward propagation only ($\alpha \leq \pi/2$), where $S(m,n)$ is the apodisation function, and $T(m,n)$ is any complex transmission filter applied across the aperture of the lens. This transmission factor can also be used to model focusing aberrations.

For uniform focusing, the Herschel condition, the apodisation function is simply

$$S_{\mathrm{h}}(m,n) = 1\ . \tag{3.11}$$

Microscope objectives are usually designed to obey the sine condition, giving aplanatic imaging (Hopkins, 1943), for which we write the apodisation as

$$S_s(m,n) = \cos^{\frac{1}{2}}\theta \tag{3.12}$$

$$= \sqrt{s_+}\ . \tag{3.13}$$

*In our original publication of this research (Arnison and Sheppard, 2002), Eq. (3.10) (Eq. (12) in the article) was incorrectly derived to include an erroneous $1/s_+$ factor. In this chapter, all equations and figures have been corrected and updated as appropriate. An erratum for *Optics Communications* is in preparation.

3.2 Three–dimensional vectorial optical transfer function

For incoherent imaging, we are interested in using the OTF to describe the frequency components of the intensity $\mathbf{E}\cdot\mathbf{E}^*$ of the PSF. From Eq. (3.1) and the Fourier autocorrelation theorem (Bracewell, 1978),

$$|f(\mathbf{x})|^2 \Longleftrightarrow \iiint F(\mathbf{m}+\frac{\mathbf{m}'}{2})F^*(\mathbf{m}-\frac{\mathbf{m}'}{2})\mathrm{d}\mathbf{m} \tag{3.14}$$

(where $\mathbf{F}(\mathbf{m})$ is the Fourier transform of $\mathbf{f}(\mathbf{x})$), we can obtain the OTF $C(\mathbf{K})$ by taking the autocorrelation of the pupil function $\mathbf{Q}$,

$$C(\mathbf{K}) \;=\; \iiint \mathbf{Q}(\mathbf{m}+\tfrac{1}{2}\mathbf{K})\cdot\mathbf{Q}^*(\mathbf{m}-\tfrac{1}{2}\mathbf{K})\mathrm{d}\mathbf{m}\,. \tag{3.15}$$

Substituting the spherical pupil function from Eq. (3.4) and again normalising the radius to $k=1$ we have

$$\begin{aligned} C(\mathbf{K}) \;=\; & \iiint \mathbf{Q}_\mathrm{s}(\mathbf{m}+\tfrac{1}{2}\mathbf{K})\delta(\left|\mathbf{m}+\tfrac{1}{2}\mathbf{K}\right|-1) \\ & \cdot\mathbf{Q}_\mathrm{s}^*(\mathbf{m}-\tfrac{1}{2}\mathbf{K})\delta(\left|\mathbf{m}-\tfrac{1}{2}\mathbf{K}\right|-1)\mathrm{d}\mathbf{m}\,. \end{aligned} \tag{3.16}$$

The spatial frequency $\mathbf{K}=(m,n,s)$ may be represented geometrically as the shift of one copy of the pupil sphere relative to the other. The total value of the integral for a given spatial frequency $\mathbf{K}$ is given by the total volume of intersection of the shifted spherical shells, multiplied at each intersection point by the values of the pupil functions at that location.

The spheres intersect in a circle perpendicular to the direction of the shift between them, which we call the *circle of intersection*, as shown schematically in figure 3.3. When the spheres are shifted so far that they no longer intersect, the value of the OTF for that shift must be zero, giving the absolute spatial frequency cutoff.

At any given point along the circle of intersection, the intersection between the spherical shells has a rhombic cross-section (Fig. 3.4). Therefore for any pupil shift $\mathbf{K}$ we need to find a general equation for the circle of intersection, so that we can find the value of the shifted pupil functions along the circle, and also an equation for the area of the rhombic cross-section.

For convenience we denote the total length of the pupil shift as K

$$K=|\mathbf{K}|=\sqrt{m^2+n^2+s^2}\,. \tag{3.17}$$

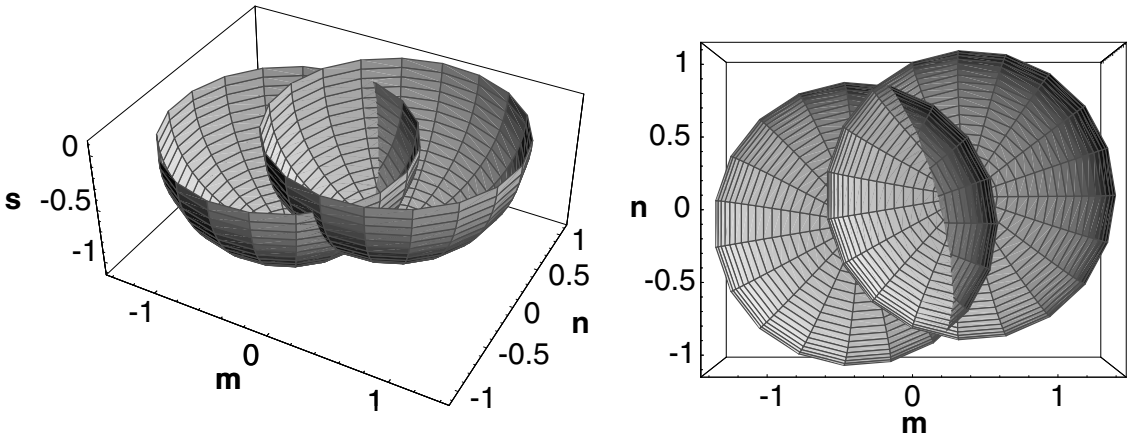

Figure 3.3: 3D views of the shifted spherical pupil caps for $K = (0.8, 0.2, 0.2)$ and $\alpha = \pi/2$. The intersection can be seen as the arc of a circle.

Figure 3.4: The rhombic area of overlap between two spherical pupil caps.

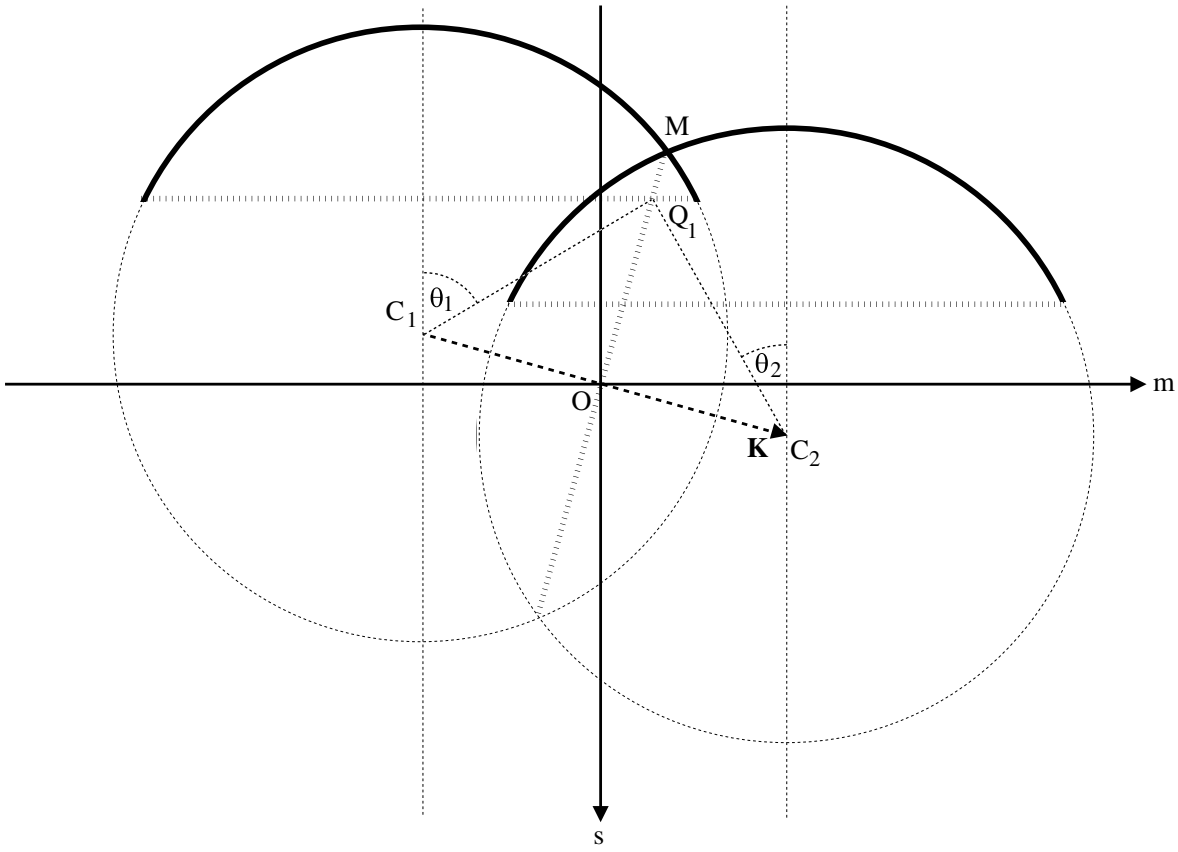

Figure 3.5: A cross-section through the intersecting spheres for a given offset between them of **K**. For the purposes of this figure, we assume $n = 0$. The radius r_0 of the arc of intersection is shown here as OM. Q_1 is the projection of P_1 from figure 3.6, the endpoint of the arc of intersection where $\beta = \beta_1$.

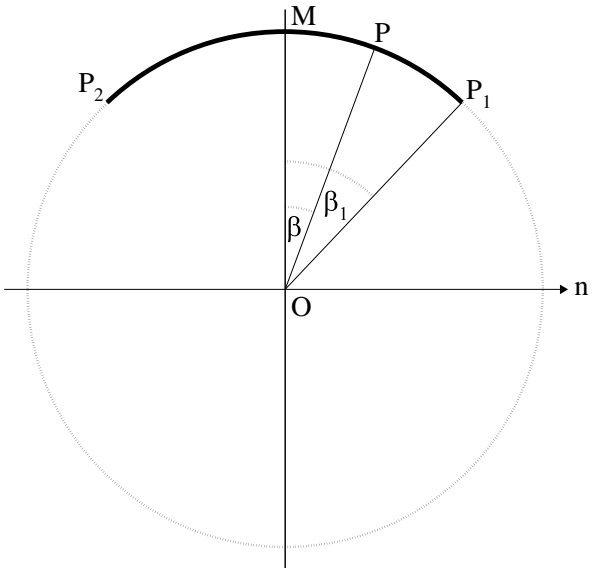

Figure 3.6: The circle of intersection, in the plane along the line MO that is perpendicular to the (m,s) plane of figure 3.5 (again assuming $n = 0$ for the purposes of the figure). The arc of intersection is shown as P_1MP_2, which varies with spatial frequency $\mathbf{K}$ and aperture angle α. For a constant pupil, the length of this arc, $2\beta_1(\mathbf{K},\alpha)$, is proportional to the strength of the transfer function for a given spatial frequency $\mathbf{K}$.

Cross-sections of the geometry for the intersecting spheres are shown in figures 3.5 and 3.6. The shifted pupil spheres can be described using vectors as

$$|\mathbf{m} \pm \mathbf{K}/2| = 1 \tag{3.18}$$

allowing us to solve for the radius of the circle of intersection of the two spheres

$$r_0 = |\mathbf{r}_0| = \sqrt{1 - \frac{K^2}{4}}\,. \tag{3.19}$$

If we can fully specify the circle of intersection using a vector equation for one case, we can use vector scaling and rotation to produce the circle of intersection for any given $\mathbf{K}$. Setting $\mathbf{K}_0 = (K,0,0)$, the circle of intersection for this case is

$$\mathbf{r}_0(\mathbf{K}_0,\beta) = \begin{pmatrix} 0 \\ r_0 \sin\beta \\ -r_0 \cos\beta \end{pmatrix} \tag{3.20}$$

where β is introduced as a parameter to isolate a point on the circle by its angle with the s axis.

We now generalise for arbitrary $\mathbf{K}$. Changes in the length of $\mathbf{K}$ are accommodated already by Eq. (3.20). Rotation of $\mathbf{K}$ whilst keeping $\beta = 0$ at the lowest s co-ordinate on the circle can be described using a pair of counter-clockwise Euler rotations,

$$\mathbf{R}_n(\theta) = \begin{pmatrix} \cos\theta & 0 & -\sin\theta \\ 0 & 1 & 0 \\ \sin\theta & 0 & \cos\theta \end{pmatrix} \tag{3.21}$$

$$\mathbf{R}_s(\phi) = \begin{pmatrix} \cos\phi & \sin\phi & 0 \\ -\sin\phi & \cos\phi & 0 \\ 0 & 0 & 1 \end{pmatrix} \tag{3.22}$$

first about the n axis, then around the s axis, giving a general form for the circle of intersection,

$$\mathbf{r}_0(\mathbf{K},\beta) = \mathbf{R}_s[-\arctan(n/m)]\mathbf{R}_n[\pi/2 - \arccos(s/K)]\mathbf{r}_0(\mathbf{K}_0,\beta) \tag{3.23}$$

$$= \begin{pmatrix} r_0 \frac{1}{lK}\left[ms\cos\beta - nK\sin\beta\right] \\ r_0 \frac{1}{lK}\left[ns\cos\beta + mK\sin\beta\right] \\ -r_0 \frac{l}{K}\cos\beta \end{pmatrix} \tag{3.24}$$

where $\arctan(n/m)$ takes account of which quadrant (m,n) is in.

Finally, we need to incorporate the rhombic shape of each intersection area along the circle of intersection (Fig. 3.4). By geometry, this shape will be constant around any given circle, but will vary according to the shift $\mathbf{K}$ between the pupils. The area A of the rhombus is given by

$$A(\mathbf{K}) = \frac{(\delta k)^2}{K r_0}\,, \tag{3.25}$$

for $K > 0$, giving a line integral. For $K = 0$ the integral becomes a surface integral proportional to δk. For infinitely thin shells, the line and surface integrals cannot be numerically compared. Since we are obviously more interested in the range $K > 0$, we focus on the line integral in this paper, for which $C(\mathbf{0}) \to \infty$. This represents the average value of the PSF intensity, which diverges due to the spatially unbounded behaviour of the PSF in Eq. (3.1).

Having accounted for the changing cross-section, we can now recast the autocorrelation, using the delta functions in Eq. (3.16) to sift out the vectorial pupil cap function $\mathbf{P}_+(m,n)$ of

Eq. (3.6), leaving a one dimensional integral along an arc of the circle of intersection. We obtain an unnormalised equation for the autocorrelation

$$C_{\mathrm{UnNorm}}(\mathbf{K}) = \frac{1}{Kr_0}\int_{-\beta_1}^{\beta_1} \mathbf{P}_+\left[\mathbf{r}_0(\mathbf{K},\beta)+\tfrac{1}{2}\mathbf{K}\right]\cdot\mathbf{P}_+^*\left[\mathbf{r}_0(\mathbf{K},\beta)-\tfrac{1}{2}\mathbf{K}\right] r_0 \mathrm{d}\beta\,, \tag{3.26}$$

where β_1 is the highest possible angle β on the circle of intersection for a given aperture α, shown as MOP_1 in figure 3.6, and defined below in Eq. (3.32). This allows us to integrate along the complete arc of intersection between the spheres.

Two dimensional and one dimensional OTFs are usually normalised against the zero frequency value. However, for the 3D case, Eq. (3.26) gives a singularity at $C(\mathbf{0})$, so we choose to normalise against the total volume of the OTF. By the Fourier definite integral theorem, this is equivalent to the central value of the intensity PSF, which we can easily determine (Richards and Wolf, 1959). We use uniform (Herschel) apodisation for determining the normalisation. Setting $|\mathbf{E}(\mathbf{0})|^2 = 1$, the normalisation factor is

$$N(\alpha) = \left\{\tfrac{1}{4}(3+\cos^2\alpha)\sin^4\frac{\alpha}{2}\right\}^2\,. \tag{3.27}$$

We now arrive at a normalised form of the 3D vectorial OTF that is easy, albeit time consuming, to calculate:

$$C(\mathbf{K}) = \frac{1}{KN(\alpha)}\int_{-\beta_1}^{\beta_1} \mathbf{P}_+\left[\mathbf{r}_0(\mathbf{K},\beta)+\tfrac{1}{2}\mathbf{K}\right]\cdot\mathbf{P}_+^*\left[\mathbf{r}_0(\mathbf{K},\beta)-\tfrac{1}{2}\mathbf{K}\right] \mathrm{d}\beta\,. \tag{3.28}$$

Note that we have made no assumptions about the symmetry of the pupil function $\mathbf{P}_+$ nor any assumptions of low aperture, and therefore this equation is suitable for calculating the 3D vectorial OTF with arbitrary pupil functions and apertures. However, there remains some symmetry in $C(\mathbf{K})$ by virtue of the fact that we defined it as the Fourier transform of a real function, the intensity PSF. This constraint results in Hermitian symmetry in the OTF,

$$C(\mathbf{K}) = C^*(-\mathbf{K})\,. \tag{3.29}$$

It is helpful to note that the angles $\theta_{1,2}$ at the centres of the spheres between the s axis and the point of intersection, as shown in figure 3.5, are given by

$$\begin{aligned}\cos\theta_{1,2}(\mathbf{K},\beta) &= -\mathbf{r}_0(\mathbf{K},\beta)\cdot\hat{\mathbf{s}}\mp\tfrac{s}{2}\\ &= r_0\tfrac{l}{K}\cos\beta\mp\tfrac{s}{2}\,.\end{aligned} \tag{3.30}$$

We now need to find the appropriate limits on the integration to ensure we only calculate in physical zones, avoiding regions where the spherical caps do not intersect. These conditions define the spatial frequency cutoff:

1. If the *spheres* are shifted by more than twice their radius, then they will never intersect. Therefore:
$$K \leq 2 \,. \tag{3.31}$$

2. The aperture will set a limit $|\beta| \leq \beta_1$ on the *length of the arc* of the circle of intersection. This limit can be found by geometry, substituting $\theta_1 = \alpha$ into Eq. (3.30) and solving for β
$$\beta_1(\mathbf{K},\alpha) = \begin{cases} \arccos\left\{\frac{K}{lr_0}(\frac{|s|}{2}+\cos\alpha)\right\} & \frac{K}{lr_0}\left|\frac{|s|}{2}+\cos\alpha\right| \leq 1 \\ 0 & \mathrm{Re}\left\{\frac{K}{lr_0}(\frac{|s|}{2}+\cos\alpha)\right\} > 1 \\ \pi & \mathrm{Re}\left\{\frac{K}{lr_0}(\frac{|s|}{2}+\cos\alpha)\right\} < -1 \,. \end{cases} \tag{3.32}$$
The second case is when the full spheres intersect, but the aperture α truncates the caps before that point. The third case is for regions where for large apertures $\alpha > \pi/2$ the arc of intersection completes a full circle.

3. It is useful for certain calculations to know the spatial frequency cutoff in terms of limits on $\mathbf{K}$, which may be determined using (Sheppard et al., 1994)
$$2(l\sin\alpha - |s|\cos\alpha) = K^2 \,. \tag{3.33}$$

3.3 Results

We evaluated Eq. (3.28) for Herschel and sine apodisations at a very high aperture ($\alpha = 2\pi/5 \Rightarrow$ NA $= 0.95$ in air) and a uniform pupil filter $T = 1$, to explore the OTF behaviour under conditions unsuitable for modelling with low NA techniques. Calculations were performed using standard Mathematica integration routines, on a Linux system with an AMD Athlon 1.4 GHz processor. Large plots such as the one in figure 3.8 took about 2 hours, while figure 3.10 took 3 minutes. A major speed boost could be expected if the integration was coded in C instead of using Mathematica. See appendix B for additional computational details.

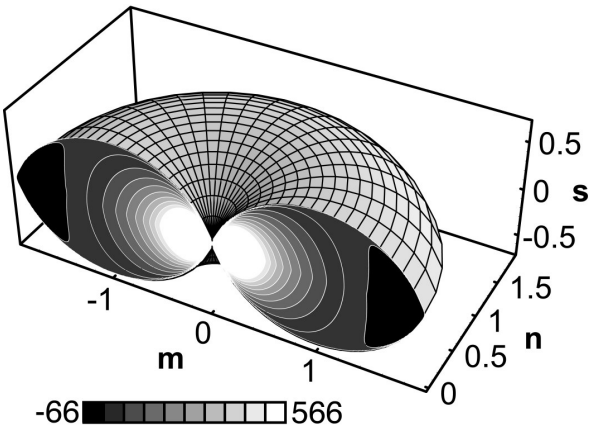

Figure 3.7: A schematic of the 3D vectorial OTF for $\alpha = 2\pi/5$ with Herschel apodisation. The mesh surface indicates the spatial frequency cutoff, outside which the OTF is zero. This surface has been sliced at $n = 0$, revealing the amplitude $C(m,0,s)$ on that plane of the 3D OTF, after taking the sum of all vector components.

Evaluating the vectorial OTF gives substantial numerical territory to explore. Each 3D point within the spatial frequency cutoff has a scalar value which may be split up into 3 contributions from the vectorial components of the pupil,

$$C = Q_x \star Q_x^* + Q_y \star Q_y^* + Q_z \star Q_z^* \tag{3.34}$$

$$= C_x + C_y + C_z \,. \tag{3.35}$$

The symbol $\star$ denotes autocorrelation. A general overview of the shape of the OTF is given in figure 3.7, showing the surface of the cutoff and the total value of the OTF for a slice through the function.

Figure 3.8 shows transverse slices through the vectorial OTF for $s = 0$, with sine apodisation. C_x shows changing asymmetry across the m and n axes. At lower frequencies, the OTF along the m axis is stronger than along the n axis, while at high frequencies the situation is reversed. C_y has a dramatic fourfold symmetry and large negative regions, but this component of the OTF is orthogonal with the input polarisation and has relatively little strength. However, C_z has substantial energy including significant negative regions. This results in a total OTF C with negative regions which indicates a contrast reversal for high frequencies parallel to the x axis in the PSF. A line plot of C along the m axis in figure 3.9 shows that while the negative region has a large width, the strength is significant relative to the mid–frequency

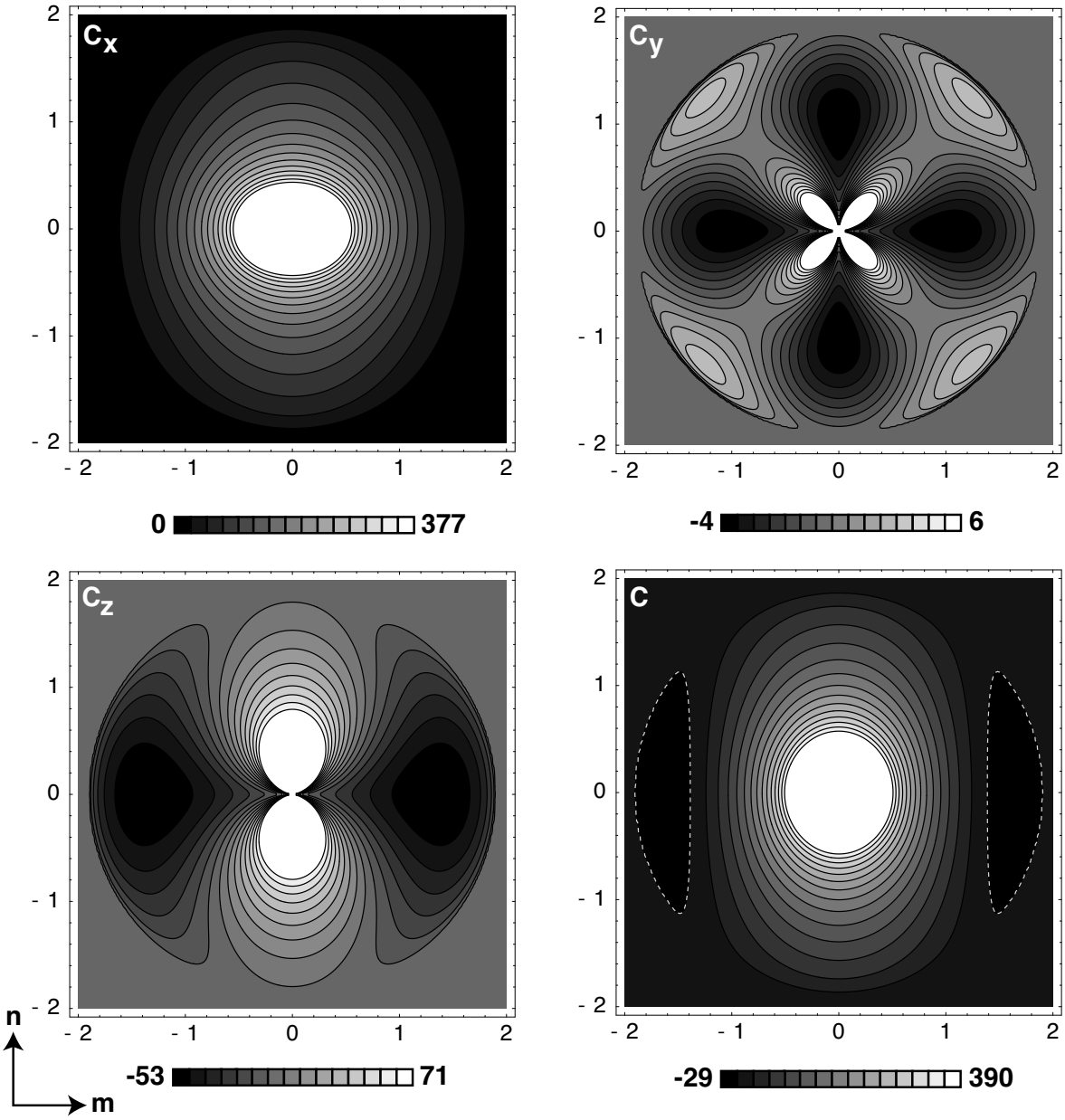

Figure 3.8: Transverse slices through the vectorial OTF for $s = 0$, with $\alpha = 2\pi/5$ and sine apodisation. The vector components and total amplitude are shown as C_x, C_y, C_z, and C. Each plot is independently scaled, due to the large differences in amplitude for the different components. Note that in this chapter we have assumed input linear polarisation along the x axis, corresponding to the m axis in frequency space. C_x shows an interesting asymmetry, with a low x frequency boost (central horizontal elongation), yet a high y frequency (vertical elongation) boost. The total amplitude C includes negative regions (indicated with a dashed contour line) at high values of m, inherited from C_z.

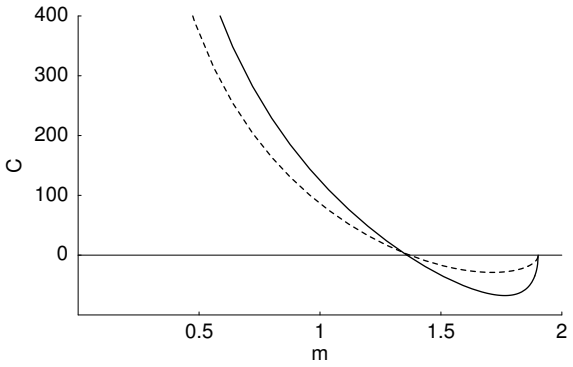

Figure 3.9: Line plot of C along the m axis with $\alpha = 2\pi/5$, for Herschel (solid) and sine (dashed) apodisation. This gives an indication of the relative strength of the negative region of C, and thus the degree of contrast reversal that can be expected at high m frequencies and low n and s frequencies.

response at $m = 1$. The strength of the negative region is smaller for sine apodisation than for Herschel apodisation.

Contrast reversal is a well known feature of the defocused 2D OTF. For the object frequencies affected, contrast reversal means that the peaks and troughs of each sinusoidal component are inverted between the object and the image. Clearly this can have a serious impact on the integrity of the image.

While the general characteristics of figure 3.8 are similar to figures 7–10 of Sheppard and Larkin (1997), we emphasise that figure 3.8 is of *slices* through the OTF rather than the projections shown in Sheppard & Larkin.

Figure 3.10 shows axial slices through the vectorial OTF for $n = 0$, with sine apodisation. For this case the most dramatic features away from the $s = 0$ plane are to be seen in the C_y component. However, again, this component contributes relatively little to the total OTF.

To enable more direct comparison with Sheppard and Larkin (1997) we calculated the *projected* OTF

$$C'(m,n) = \int C(m,n,s)\mathrm{d}s\,. \tag{3.36}$$

By the projection-slice theorem (Bracewell, 1995), this corresponds to the spatial frequencies in a transverse slice along the focal plane of the intensity PSF. We can again break up this projected OTF into components corresponding to the intensities of the polarisation components of the PSF, $C' = C'_x + C'_y + C'_z$. Figure 3.11(a) shows C'_z for Herschel apodisation, which corresponds to figure 9 of Sheppard and Larkin (1997), and with which it agrees closely. Figure 3.11(b) shows C' for sine apodisation. With a negative region of about 10%

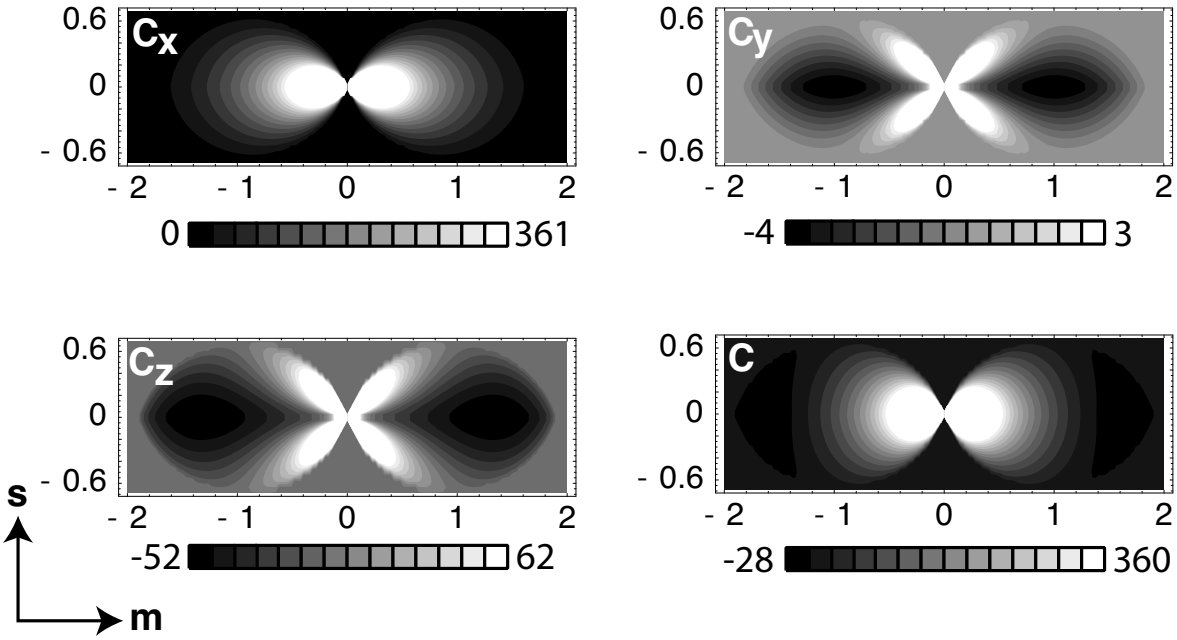

Figure 3.10: Axial slices through the vectorial OTF for $n = 0$, with $\alpha = 2\pi/5$ and sine apodisation. The vector components and total amplitude are shown. As for the transverse slices, the C_y and C_z components show interesting structure. However C_y is very weak compared with the other components, so this will not have a very large effect overall. The negative regions in C_z are seen to persist across a wide range of s frequencies, with a corresponding impact on C.

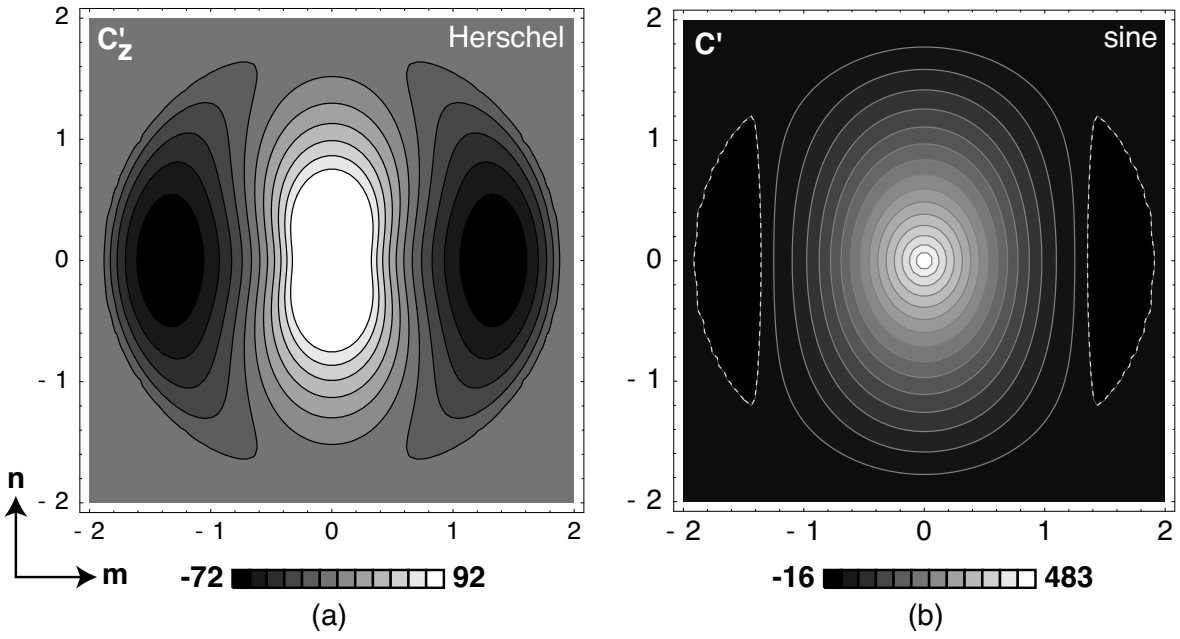

Figure 3.11: Axial projections of the vectorial OTF. (a) The strength C'_z of the projection through s of the z component of the vectorial OTF for $\alpha = 2\pi/5$ and Herschel apodisation. This is equivalent to figure 9 of Sheppard and Larkin (1997). (b) The total projection C' for $\alpha = 2\pi/5$ and sine apodisation. A special dashed contour at $C = -0.5$ indicates the negative regions.

of the value of the mid frequency response, contrast reversal can be expected for high m transverse frequencies. The n frequencies are stronger overall than the m frequencies, as has been noted before in direct studies of the vectorial PSF (Hopkins, 1943; Richards and Wolf, 1959).

Calculating the projected OTF in this manner is very time-consuming, taking about 10 hours on our Linux system. The 2D FFT approach described by Sheppard and Larkin (1997) is thus much more efficient for calculation of projections.

An alternative way to explore the 3D structure of the OTF is to view the data as isosurfaces, which are the 3D equivalent of contour lines. Figures 3.12–3.16 show isosurfaces for the total OTF C as well as the components C_x, C_y and C_z. All isosurface plots are for $\alpha = 2\pi/5$ and sine apodisation.

3.4 Discussion

The vectorial OTF is a relatively new concept in optical imaging theory, and raises substantial questions of interpretation and meaning. We have explored the vectorial OTF for unaberrated focusing. Clearly there are significant asymmetries in the vectorial OTF at high NA for polarised light. C_x has a low x frequency boost, yet a high y frequency boost, while the total C emphasises y frequencies and becomes negative for large x frequencies. The size and strength of the negative regions in the OTF means that contrast reversal is an important and unavoidable feature of vectorial focusing. These asymmetries and contrast reversals are normally absent in a 2D scalar OTF which is free of aberrations.

The application of the vectorial OTF to modelling an entire imaging system is less straightforward than for standard 2D transfer functions as used in Fourier optics. The vectorial OTF presented here is simply a representation of the frequency content of the intensity pattern in the focal region of a single lens illuminated by a linearly polarised plane wave. It could be argued, therefore, that the term vectorial OTF is not appropriate, and that it should be called instead the vectorial intensity spatial frequency spectrum. However, we have chosen to use the shorthand notation of vectorial OTF, as the OTF is well-known to represent the spatial frequency content of the intensity PSF in scalar 2D optics.

The performance of a system will depend on the imaging behaviour of at least one lens, and the vectorial response of the specimen. For example, to apply this theory to fluorescence microscopy, we need to use a model of the dipole orientation, rotation and response of the excited molecules for varying incident polarisation and spatial frequency (Török and Shep-

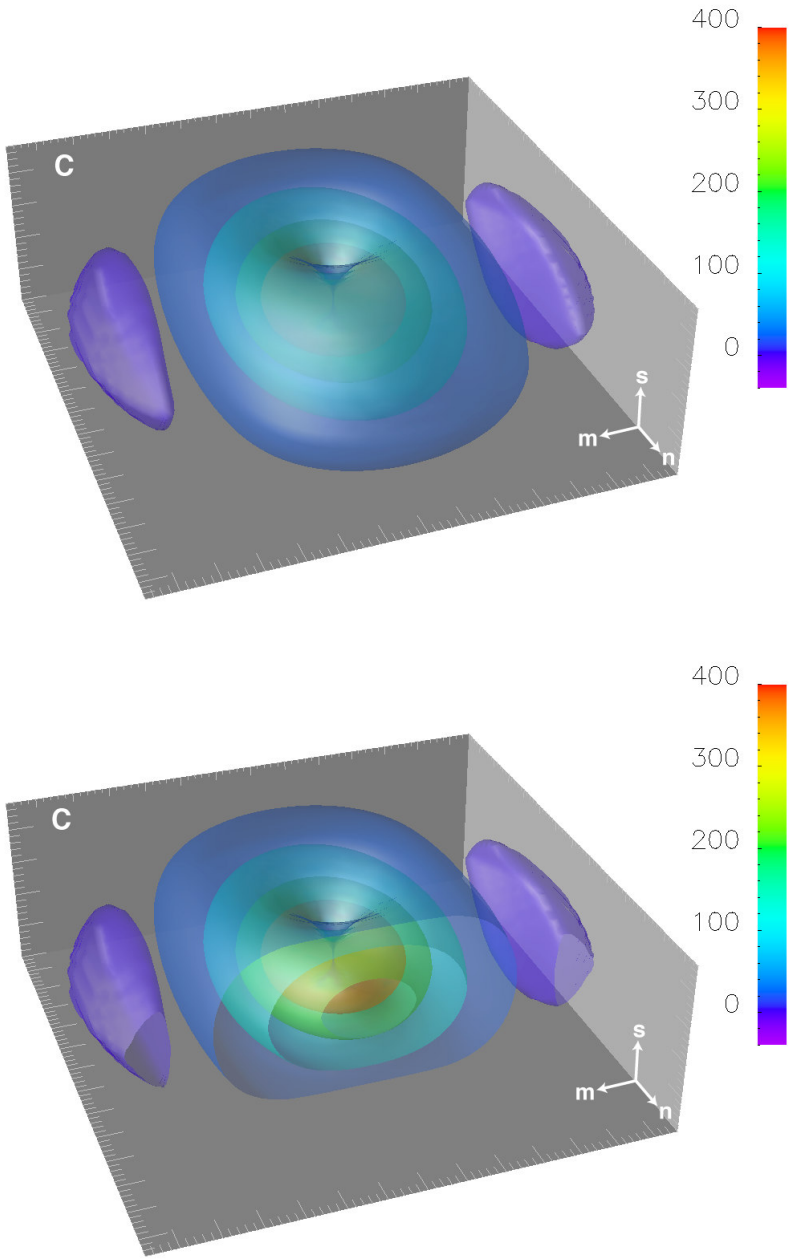

Figure 3.12: Isosurface plots of the total vectorial OTF C. All isosurfaces in this chapter are for $\alpha = 2\pi/5$ and sine apodisation. The colours indicate the value of C on each surface. The overall shape is shown in the top figure. Note the purple high m frequency side-lobes are actually negative, corresponding to contrast reversal. The bottom figure shows a cut-away, revealing a more symmetric response for low spatial frequencies.

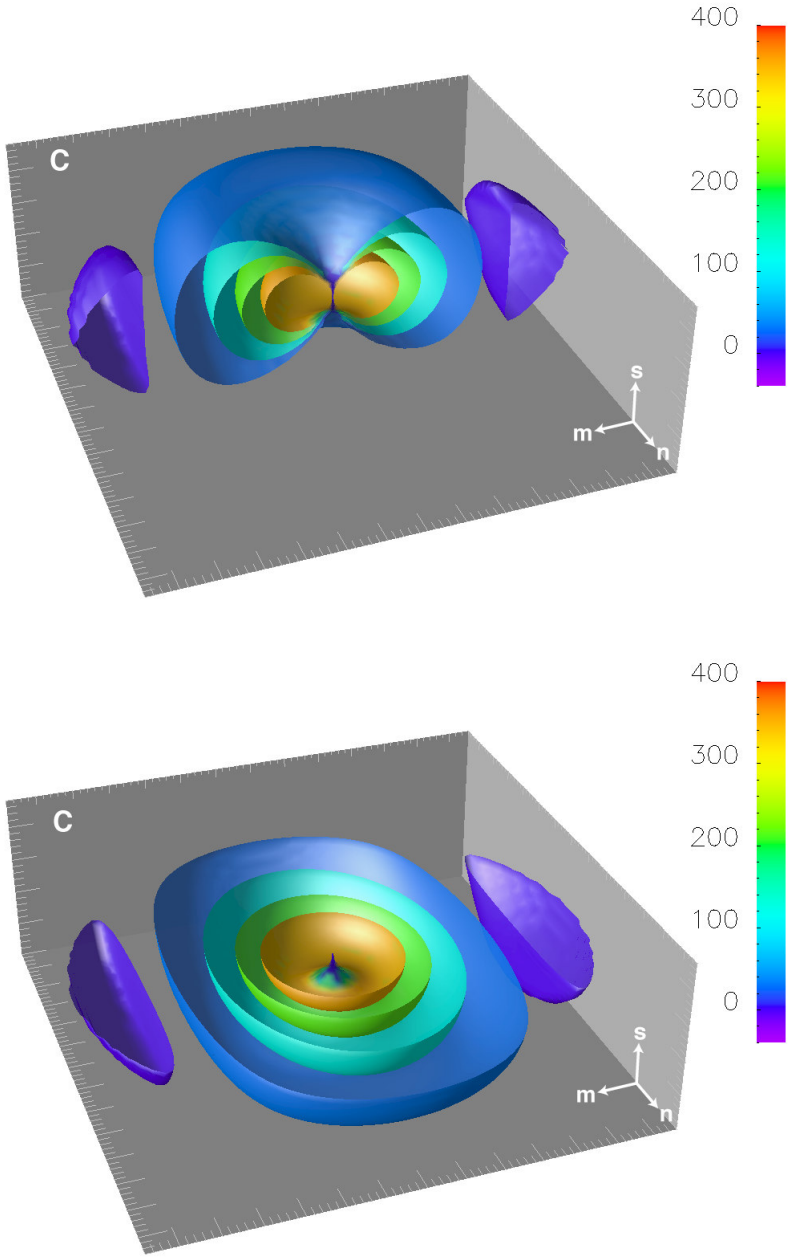

Figure 3.13: Isosurfaces of C sliced through $n = 0$ (top) and $s = 0$ (bottom). These slices correspond to figures 3.10 and 3.8 respectively.

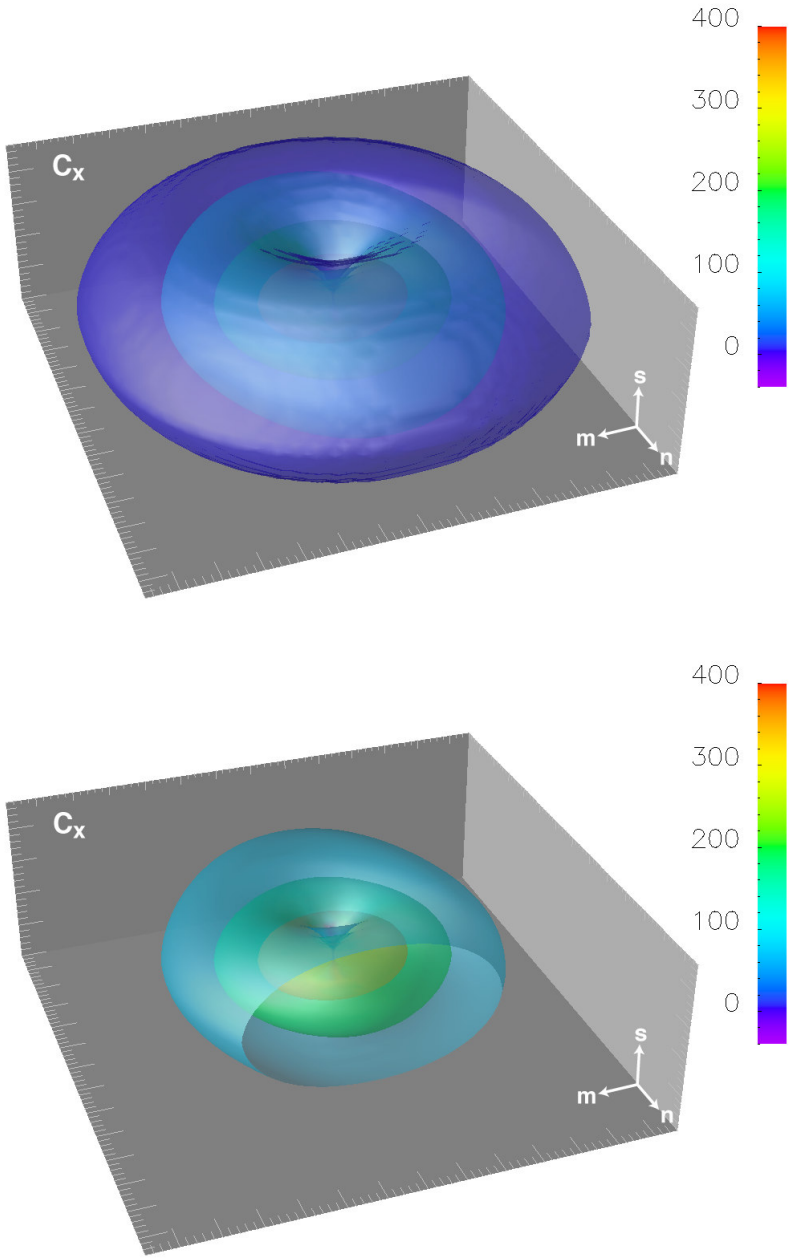

Figure 3.14: Isosurfaces of C_x. The well-known 3D OTF doughnut shape is clear in the top figure, with the missing cone in the centre. The bottom figure highlights the switch in asymmetry between favouring the n component at mid-range spatial frequencies (cyan) to favouring the m component at low-range spatial frequencies (green and orange).

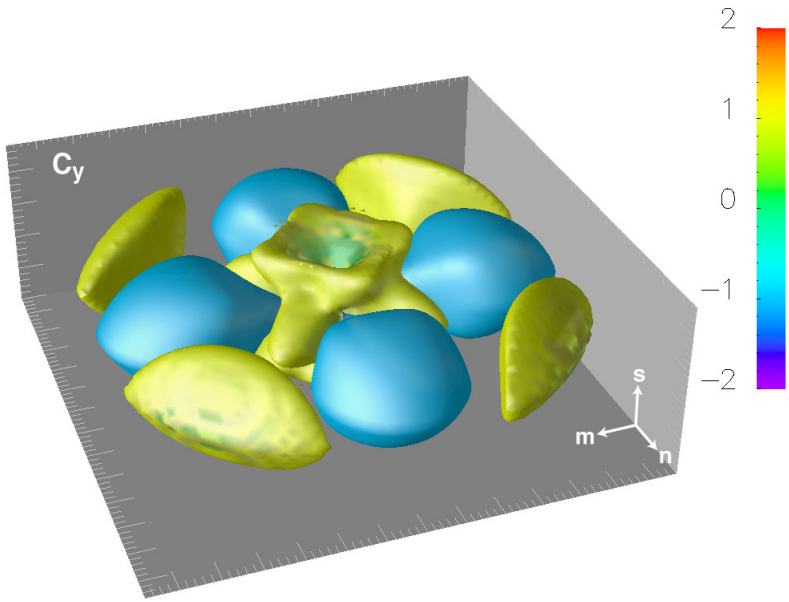

Figure 3.15: Isosurfaces of C_y. There is an interesting pattern of positive and negative spatial frequency contributions. But as the scale bar indicates, there is very little power in this component.

pard, 2002). By incorporating this dipole response model, the vectorial OTF might form an important tool in modelling the frequency response of entire imaging systems.

If the dipole can freely rotate, then the image in a confocal fluorescence microscope is the same as for an isotropic point object (Sheppard and Török, 1997b) and we can use the appropriate vectorial OTF directly. Streibl (1984b) made a similar observation in his discussion of the scalar 3D OTF, while also noting that for the OTF to be directly applicable fluorescent specimens must be "weak" (thin, small changes in refractive index and highly transparent) so that secondary scattering becomes negligible. We can therefore assume a linear system when modelling incoherent transmission microscopy of isotropic weakly scattering objects.

Our use of the Debye approximation assumes a high Fresnel number. However, unless the Fresnel number is infinite, regions of the PSF very far from focus will have smaller Fresnel numbers. Since each point in the OTF naturally encompasses Fourier components from throughout the theoretically infinite extent of the PSF, the Debye approximation places a limit on the accuracy of the OTF. While in general the contributions of regions away from focus will be small due to the concentration of power at focus, this approximation will be a concern for very strong aberrations which distribute significant energy away from the focal point.

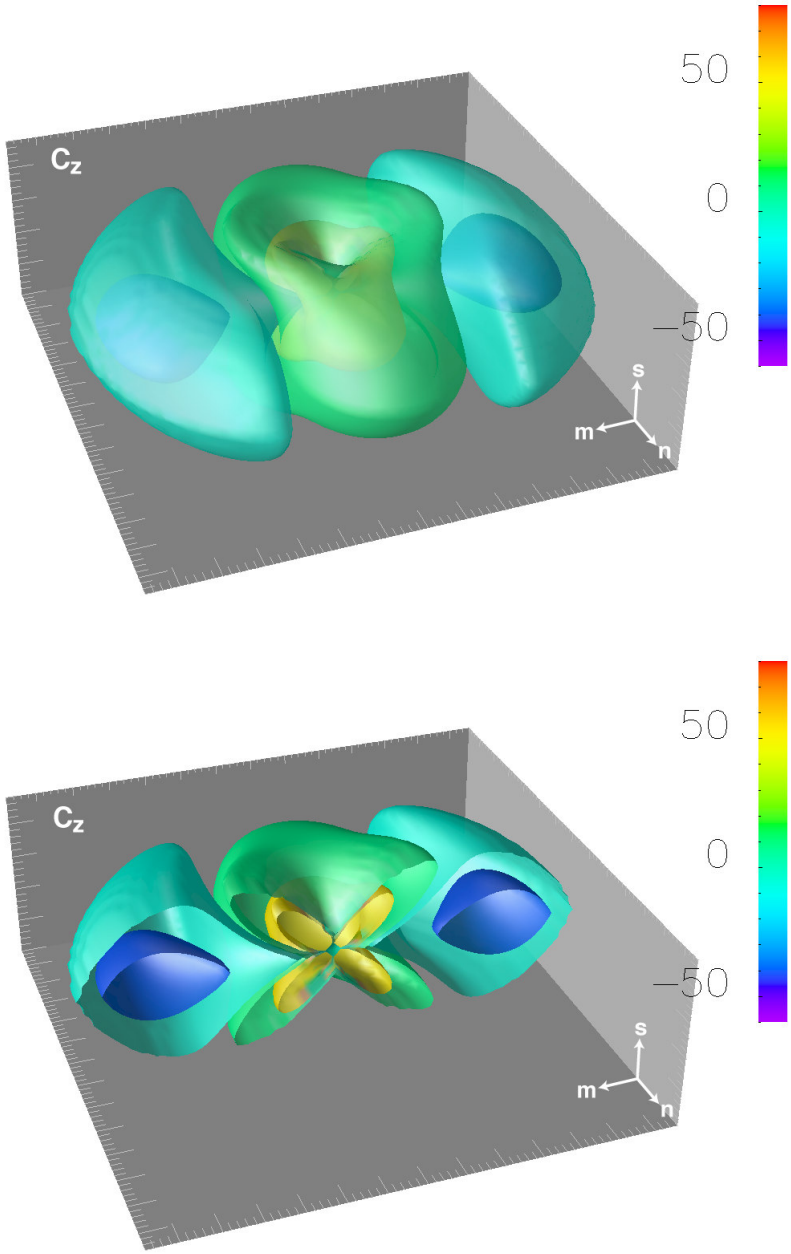

Figure 3.16: Isosurfaces of C_z. The upper figure shows the division between positive and negative strengths at low and high m respectively. The negative regions, exposed by a cut-away along the line $n = 0$ in the lower figure, are strong enough to overpower C_x at high m frequencies and push the overall OTF C into a negative response. This illustrates how high aperture depolarisation of linearly polarised illumination is responsible for high frequency contrast reversal, and how this influence derives from the axially polarised component of the focal field.

Typically aberrations in paraxial systems are modelled using Zernike polynomials describing the phase variation across a circular pupil (Born and Wolf, 1999), and this is a useful tool in Fourier optics. Some aberrations, such as defocus or spherical aberration, can be described using the radial pupil co-ordinate alone, but, in general, aberrations depend on both the radial and polar co-ordinate. Although Zernike polynomials are not orthogonal for high aperture systems, due to their assumption of a flat 2D pupil, clearly any general description of aberrations will allow for radial asymmetry. This provides a further justification for OTF calculation methods which make no assumptions of symmetry.

A high NA equivalent of the Zernike functions is needed, defined on the cap of a sphere rather than across a circle, to describe focusing aberrations (Sheppard, 1997). In addition, the causes of aberrations, such as a refractive index change in the specimen, need to be carefully mapped from rigorous PSF models onto the pupil function (Török et al., 1995; Török, 1999; Schönle and Hell, 2002; Rohrbach and Stelzer, 2002a).

Modelling amplitude and phase masks placed in the back focal plane of the lens is somewhat simpler — they can be applied directly to the model presented here using the complex transmission filter $T(m,n)$.

In conclusion, we have presented an autocorrelation based method for evaluating the high NA vectorial OTF using a simple line integral. Arbitrary pupil functions may be used without the need for cylindrical symmetry. We have plotted slices, isosurfaces and a projection through the vectorial OTF for unaberrated focusing with sine and Herschel apodisation. Although in principle the same information is contained in the PSF, the OTF makes it easier to see frequency-based focusing characteristics.

For OTF projections, FFT–based methods are more efficient as long as care is taken with accuracy and sampling effects. In addition, such projections of the OTF only carry information about a single plane of the PSF, and caution is required before including them as part of a system model.

In general, our autocorrelation method for calculating the vectorial OTF has the advantage of being straightforward to evaluate for arbitrary pupil functions and arbitrary points in the OTF.

Part II

High aperture wavefront coding

Chapter 4

Wavefront coding theory

This chapter investigates theoretical models for wavefront coding microscopy. We select the cubic phase mask (CPM) for study as an example waveplate used in wavefront coding to extend the depth of field by making the system optical transfer function (OTF) insensitive to defocus. This has been demonstrated by our experiments using wavefront coding with high resolution microscopy, as described in chapter 5.

Here we present a summary of the development of the cubic phase function and the paraxial theory initially used to model it. We then analyse the system using vectorial high aperture theory, which is normally required for accurate modelling of systems using a 1.3 NA lens, as in our experiments.

High aperture vectorial models of the PSF for a fluorescence microscope are well developed (Higdon et al., 1999; Török and Sheppard, 2002; Török et al., 1995, 1997). The Fourier space equivalent, the OTF, also has a long history (Frieden, 1967; McCutchen, 1964; Sheppard et al., 1994). However, the CPM is an unusual microscope element:

1. Microscope optics usually have radial symmetry around the optical axis, which the CPM does not.

2. The CPM gives a very large phase aberration of up to 60 waves, whilst most aberration models are oriented towards phase strengths on the order of a wave at most.

3. In addition, the CPM spreads the light over a very long focal range, whilst most PSF calculations can assume the energy drops off very rapidly away from focus.

These peculiarities have meant we needed to take particular care with numerical computation in order to ensure accuracy. In the case of the OTF, modelling a radially asymmetric pupil motivated the reformulation of previous symmetric OTF theory, as presented in chapter 3.

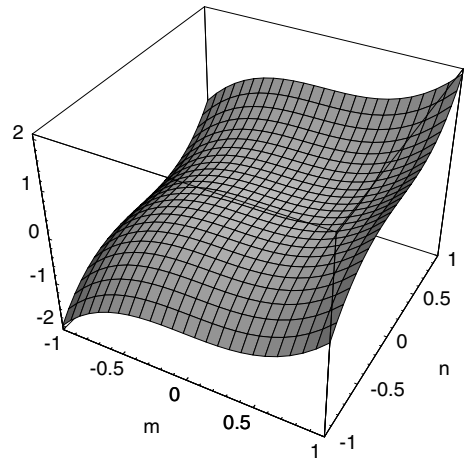

Figure 4.1: Height variation across the cubic phase mask given in Eq. (4.3), for $A = 1$.

4.1 Derivation of the cubic phase function

There are various methods that may be used to derive a pupil phase function which has the desired characteristics for EDF imaging. The general form of a phase function in Cartesian co-ordinates is

$$T(m,n) = \exp[\mathrm{i}k\varphi(m,n)] \,, \tag{4.1}$$

where m,n are the lateral pupil co-ordinates and $k = 2\pi/\lambda$ is the wave-number. The cubic phase function was developed by Dowski and Cathey (1995) using paraxial optics theory. They began by assuming that the desired phase function is a simple 1D function of the form

$$\varphi(m) = Am^{\gamma},\ \gamma \neq \{0,1\},\ A \neq 0 \,. \tag{4.2}$$

Searching for the values of A and γ which give an OTF which does not change through focus, they found that the best solution was for $A \gg 20/k$ and $\gamma = 3$. Multiplying out to 2D, this gives the cubic phase function

$$\varphi(m,n) = A(m^3 + n^3) \,, \tag{4.3}$$

where m and n are the Cartesian co-ordinates across the pupil and A is the strength of the phase mask (see Fig. 4.1).

Dowski and Cathey's derivation relies on the stationary phase approximation (Born and Wolf, 1999) and the ambiguity function (Brenner et al., 1983). The stationary phase approximation is useful in optical integrals where the integrand includes a rapidly oscillating

phase term. In such cases the largest contributions to the integral come from the places where the phase derivative is zero, or in other words where the phase is stationary. This observation is the basis of the stationary phase approximation. The ambiguity function is a 2D polar display of the defocused OTF for a rectangularly symmetric paraxial system. The radial position maps to the OTF frequency and the polar angle maps to defocus. Dowski and Cathey simplified the ambiguity function by applying the stationary phase approximation. The resulting function enabled them to optimise their pupil phase function for minimal OTF variation with defocus, and hence produce EDF behaviour.

4.2 Theoretical models

4.2.1 Paraxial model

Using the Fraunhofer approximation, as suitable for low NA, we can write down a 1D pupil transmission function encompassing the effects of cubic phase and defocus,

$$T(m) = \exp[\mathrm{i}k\varphi(m)]\exp(\mathrm{i}m^2\psi)\ , \tag{4.4}$$

where ψ is a defocus parameter. We then find the 1D PSF is

$$E(x) = \int_{-1}^{1} T(m)\exp(\mathrm{i}xm)\mathrm{d}m\ , \tag{4.5}$$

where x is the lateral co-ordinate in the PSF . The 1D OTF is

$$C(m) = \int_{-1}^{1} T(m'+m/2)\mathrm{T}^*(m'-m/2)\mathrm{d}m'\ . \tag{4.6}$$

The 2D PSF is simply $E(x)E(y)$.

Naturally this 1D CPM gives behaviour in which, for low aperture systems at least, the lateral x and y imaging axes are independent of each other. This gives significant speed boosts in digital post–processing. Another important property of the CPM is that the OTF does not reach zero below the spatial frequency cutoff, which means that deconvolution can be carried out in a single step. The lengthy iterative processing of widefield deconvolution is largely due to the many zeros in the conventional defocused OTF. Another important feature of Fraunhofer optics is that PSF variation with defocus is limited to scaling changes. Structural changes in the PSF pattern are not possible.

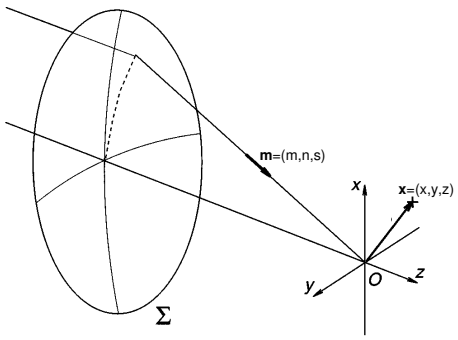

Figure 4.2: Diagram of the light focusing geometry used in calculating the high NA PSF, indicating the focal region co-ordinate **x** and the pupil co-ordinate **m**, the latter of which may also be thought of as a unit vector aligned with a ray from the pupil to the focal point O.

This paraxial model for the cubic phase mask has been thoroughly verified experimentally for low NA systems (Bradburn et al., 1997; Tucker et al., 1999).

4.2.2 High aperture PSF model

We now explore the theoretical behaviour for a high NA cubic phase system. Normally we need high aperture theory for accurate modelling of lenses with NA > 0.5. However large aberrations like our cubic phase mask can sometimes overwhelm the high NA aspects of focusing. By comparing the paraxial and high NA model results we can determine the accuracy of the paraxial approximation for particular wavefront coding systems.

We follow a similar line of development to section 3.1, revisiting Eqs. (3.1), (3.4), (3.5), (3.7), and (3.9) in the context of PSF calculation.

The theory of Richards and Wolf (1959) describes how to determine the electric field in the focal region of a lens which is illuminated by a plane polarised quasi-monochromatic light wave. Their analysis assumes very large values of the Fresnel number, equivalent to the Debye approximation. We can then write the equation for the vectorial amplitude PSF $\mathbf{E}(\mathbf{x})$ of a high NA lens illuminated with a plane polarised wave as the Fourier transform of the complex vectorial pupil function $\mathbf{Q}(\mathbf{m})$ (McCutchen, 1964),

$$\mathbf{E}(\mathbf{x}) = -\frac{\mathrm{i}k}{2\pi} \int\int\int \mathbf{Q}(\mathbf{m}) \exp(\mathrm{i}k\mathbf{m}\cdot\mathbf{x}) \mathrm{d}\mathbf{m} \,. \tag{4.7}$$

Here $\mathbf{m} = (m,n,s)$ is the Cartesian pupil co-ordinate, and $\mathbf{x} = (x,y,z)$ is the focal region co-ordinate. The z axis is aligned with the optical axis, and s is the corresponding pupil co-ordinate, as shown in Fig. 4.2. The vectorial pupil function $\mathbf{Q}(\mathbf{m})$ describes the effect of

a lens on the polarisation of the incident field, the complex value of any amplitude or phase filters across the aperture, and any additional aberration in the lens focusing behaviour from that which produces a perfect spherical wavefront converging on the focal point.

From the Helmholtz equation for a homogeneous medium, assuming constant refractive index in the focal region, we know that the pupil function is only non-zero on the surface $\mathbf{Q}_\mathrm{s}(\mathbf{m})$ of a sphere with radius k,

$$\mathbf{Q}(\mathbf{m}) = \mathbf{Q}_\mathrm{s}(\mathbf{m})\delta(|\mathbf{m}| - k)\,. \tag{4.8}$$

Because the pupil function only exists on the surface of a sphere, we can slice it along the $s = 0$ plane into a pair of functions

$$\mathbf{Q}(\mathbf{m}) = \mathbf{Q}_\mathrm{s}(\mathbf{m})\delta(s - \sqrt{k^2 - l^2}) + \mathbf{Q}_\mathrm{s}(\mathbf{m})\delta(s + \sqrt{k^2 - l^2})\,, \tag{4.9}$$

representing forward and backward propagation (Arnison and Sheppard, 2002; Sheppard and Larkin, 1997). Here we have introduced a radial co-ordinate $l = \sqrt{m^2 + n^2}$. Now we examine the axial projections $\mathbf{P}'_\pm(m,n)$ of the pupil function,

$$\mathbf{P}'_+(m,n) = \int_0^\infty \mathbf{Q}(\mathbf{m})\mathrm{d}s \tag{4.10}$$

$$\mathbf{P}'_-(m,n) = \int_{-\infty}^0 \mathbf{Q}(\mathbf{m})\mathrm{d}s\,, \tag{4.11}$$

which represent forward and backward propagation respectively. Together these 2D functions give a complete description of the 3D pupil function $\mathbf{Q}(\mathbf{m})$.

Restricting our attention to the forward propagation case, we can write

$$\mathbf{P}'_+(m,n) = \int_0^\infty \mathbf{Q}_\mathrm{s}(\mathbf{m})\delta(s - \sqrt{k^2 - l^2})\mathrm{d}s \tag{4.12}$$

$$= \mathbf{Q}_\mathrm{s}(m,n,s_+)\frac{1}{s_+}\,, \tag{4.13}$$

where the prime denotes projection. The $1/s_+$ factor accounts for the change in projected thickness of the spherical shell for declination angles away from the s axis. We have normalised the radius to $k = 1$ and indicated the constraint on s to the surface of the sphere with

$$s_+ = \sqrt{1 - l^2}\,. \tag{4.14}$$

For incident light which is plane-polarised along the x axis, we can derive a vectorial strength function $\mathbf{a}(m,n)$, from the strength factors used in the vectorial point spread function integrals (Mansuripur, 1986; Richards and Wolf, 1959; Sheppard and Larkin, 1997)

$$\mathbf{a}(m,n) = \begin{pmatrix} (m^2 s_+ + n^2)/l^2 \\ -mn(1-s_+)/l^2 \\ -m \end{pmatrix} \tag{4.15}$$

where we have converted from the Richards and Wolf spherical polar representation into Cartesian co-ordinates.

We can now model polarisation, apodisation and aperture filtering as amplitude and phase functions over the projected pupil,

$$\mathbf{P}'_+(m,n) = \frac{1}{s_+}\,\mathbf{a}(m,n)S(m,n)T(m,n) \tag{4.16}$$

representing forward propagation only ($\alpha \leq \pi/2$), where $S(m,n)$ is the apodisation function, and $T(m,n)$ is any complex transmission filter applied across the aperture of the lens. T can also be used to model aberrations.

Microscope objectives are usually designed to obey the sine condition, giving aplanatic imaging (Hopkins, 1943), for which we write the apodisation as

$$S(m,n) = \sqrt{s_+}\,. \tag{4.17}$$

By applying low angle and scalar approximations, we can derive from Eq. (4.16) a paraxial pupil function,

$$P'_+(m,n) \approx T(m,n)\,. \tag{4.18}$$

Returning to the PSF, we have

$$\mathbf{E}(\mathbf{x}) = -\frac{\mathrm{i}k}{2\pi}\int\int_\Sigma \mathbf{P}'_+(m,n)\exp(\mathrm{i}k\mathbf{m}_+\cdot\mathbf{x})\mathrm{d}m\mathrm{d}n\,, \tag{4.19}$$

integrated over the axial projection of the pupil area Σ. The geometry is shown in Fig. 4.2. We use $\mathbf{m}_+ = (m,n,s_+)$ to indicate that $\mathbf{m}$ is constrained to the pupil sphere surface.

For a clear circular pupil of aperture half–angle α, the integration area Σ_{circ} is defined by

$$0 \leq l \leq \sin\alpha\,, \tag{4.20}$$

while for a square pupil which fits inside that circle, the limits on Σ_{sq} are

$$\begin{array}{l} |m| \leq \sin\alpha/\sqrt{2} \\ |n| \leq \sin\alpha/\sqrt{2} \end{array} . \tag{4.21}$$

The transmission function T is unity for a standard widefield system with no aberrations, while for a cubic phase system Eq. (4.1) and Eq. (4.3) give

$$T_{\mathrm{c}}(m,n) = \exp[\mathrm{i}kA(m^3+n^3)] . \tag{4.22}$$

4.2.3 High aperture OTF model

A high aperture analysis of the OTF is important, because the OTF has proven to be more useful than the PSF for design and analysis of low aperture wavefront coding systems. For full investigation of the spatial frequency response of a high aperture microscope, we would normally look to the 3D OTF (Frieden, 1967; McCutchen, 1964; Sheppard and Cogswell, 1990; Sheppard et al., 1994). Chapter 3 describes a method for calculating the 3D OTF suitable for arbitrary pupil filters which can be applied directly to find the OTF for a cubic phase plate. But since an EDF system involves recording a single image at one focal depth, a frequency analysis of the 2D PSF at that focal plane is more appropriate. This can be performed efficiently using a high NA vectorial adaptation of 2D Fourier optics (Sheppard and Larkin, 1997).

This adaptation relies on the Fourier projection–slice theorem (Bracewell, 1995), which states that a slice through real space is equivalent to a projection in Fourier space:

$$f(x,y,0) \Longleftrightarrow \int F(m,n,s)\mathrm{d}s \tag{4.23}$$

where $F(m,n,s)$ is the Fourier transform of $f(x,y,z)$. We have already obtained the projected pupil function $\mathbf{P}'_{+}(m,n)$ in Eq. (4.16). Taking the 2D Fourier transform and applying Eq. (4.23) gives the PSF in the focal plane

$$\mathbf{E}(x,y,0) \Longleftrightarrow \mathbf{P}'_{+}(m,n) . \tag{4.24}$$

Since fluorescence microscopy is incoherent, we then take the intensity and 2D Fourier transform once more to obtain the OTF of that slice of the PSF

$$|\mathbf{E}(x,y,0)|^2 \Longleftrightarrow C(m,n) . \tag{4.25}$$

We can implement this approach using 2D fast Fourier transforms to quickly calculate the high aperture vectorial OTF for the focal plane.

4.2.4 Defocused OTF and PSF

To investigate the EDF performance, we need to calculate the defocused OTF. Defocus is an axial shift z_d of the point source being imaged relative to the focal point. By the Fourier shift theorem, a translation z_d of the PSF is equivalent to a linear phase shift in the 3D pupil function,

$$\mathbf{E}(x,y,0+z_\mathrm{d}) \Longleftrightarrow \exp(\mathrm{i}ksz_\mathrm{d})\mathbf{Q}(m,n,s)\,. \tag{4.26}$$

Applying the projection-slice theorem as before gives a modified version of Eq. (4.24)

$$\mathbf{E}(x,y,z_\mathrm{d}) \Longleftrightarrow \int \exp(\mathrm{i}ksz_\mathrm{d})\mathbf{Q}(m,n,s)\mathrm{d}s\,, \tag{4.27}$$

allowing us to isolate a pupil transmission function that corresponds to a given defocus z_d,

$$T_\mathrm{d}(m,n,z_\mathrm{d}) = \exp(\mathrm{i}ks_+z_\mathrm{d})\,, \tag{4.28}$$

which we incorporate into the projected pupil function $\mathbf{P}'_+(m,n)$ from Eq. (4.16), giving

$$\mathbf{P}'_+(m,n,z_\mathrm{d}) = \frac{1}{s_+}\,\mathbf{a}(m,n)S(m,n)T_\mathrm{d}(m,n,z_\mathrm{d})T_\mathrm{c}(m,n)\,. \tag{4.29}$$

Note that the defocus phase factor $\exp(\mathrm{i}ks_+z)$ was already presented in Eq. (4.19), however it is conceptually and mathematically convenient to explicitly include it as an aberration factor across the projected pupil within a standard 2D Fourier integral. For example, if we assume a low aperture pupil, we can approximate Eq. (4.14) to second order, giving the well known paraxial aberration function for defocus

$$T_\mathrm{d}(m,n,z_\mathrm{d}) \approx \exp\left(-\mathrm{i}kz_\mathrm{d}\frac{l^2}{2}\right)\,. \tag{4.30}$$

Finally, using $\mathcal{F}$ to denote a Fourier transform, we write down the full algorithm for calculating the OTF of a transverse slice through the vectorial PSF:

$$C(m,n,z_\mathrm{d}) = \mathcal{F}_\mathrm{2D}^{-1}\left\{\left|\mathcal{F}_\mathrm{2D}\left[\mathbf{P}'_+(m,n,z_\mathrm{d})\right]\right|^2\right\}\,. \tag{4.31}$$

It is convenient to calculate the vectorial defocused PSF using only the first step of this approach

$$\mathbf{E}(x,y,z_{\mathrm{d}}) = \mathcal{F}_{2\mathrm{D}}\left[\mathbf{P}'_{+}(m,n,z_{\mathrm{d}})\right] \ . \tag{4.32}$$

Mansuripur (1986, 1989, 1993) obtained the same result but there are differences in detail and emphasis between his approach and what I have presented.

4.2.5 Refractive index change model

Spherical aberration is a common problem in high aperture fluorescence microscopy. There are several potential causes based on planar refractive index changes:

- a refractive index mismatch between the immersion medium of the lens (e.g. oil) and the mounting medium of the specimen (e.g. water);
- high aperture objectives may be designed to perform best with immersion oil of a particular refractive index, but a small change in temperature or composition of the oil can produce a variation in its refractive index; and
- the coverglass thickness may not precisely match the specifications of the objective.

Since it is not always easy to control these factors experimentally, additional options for reducing the impact of spherical aberration are desirable. Some objectives have correction collars, which compensate for refractive index changes. However, turning such collars can be imprecise as each adjustment of the collar also changes the focal point of the lens. Finding the best setting involves hunting with both the collar and the focus of the microscope while looking for the best image. More complex correction methods may involve physical or computational adaptive optics (Booth et al., 2002; Kam et al., 2001).

Wavefront coding is designed to achieve focus invariance. However, it turns out that wavefront coding also reduces the impact of spherical aberration on imaging performance, as described for the paraxial case by Mezouari and Harvey (2003). To explore the situation for high aperture imaging, we implemented a focusing model which includes both the CPM and a refractive index change in the focal region.

There are several different approaches to high aperture modelling of refractive index changes. Török et al. (1995) extended the Debye–Wolf integral (Eq. (2.11)) to include a planar refractive index boundary. They mentioned that the effects of the refractive index change on the PSF can be modelled as a pupil surface aberration function, which is the approach used in calculations by Rohrbach and Stelzer (2002a) and Schönle and Hell (2002).

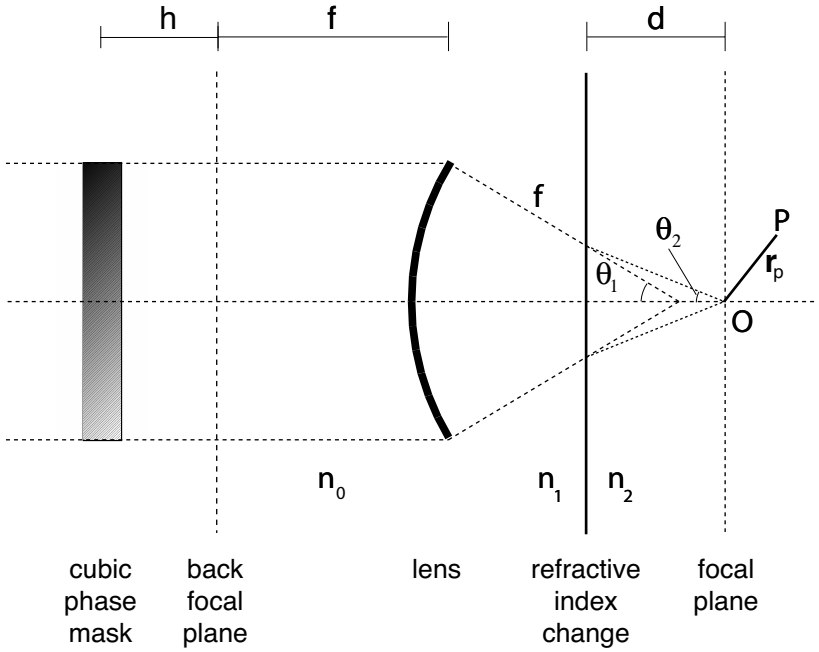

Figure 4.3: Cubic phase mask focusing model including a refractive index change in the focal region. P is the observation point. The case for $n_2 > n_1$ is indicated by the decrease in angle $\theta_2 < \theta_1$. In this chapter we show results for an oil to water interface, for which the Gaussian focal point O moves towards the lens rather than away from it as illustrated here. Also in this chapter the CPM is always in the back focal plane ($h = 0$).

Egner et al. (Egner and Hell, 1999; Egner et al., 1998) describe an alternate refractive index mismatch theory, which is derived from the Huygens–Fresnel theory without using the Debye–Wolf approximation. They say this Huygens–Fresnel based model works for arbitrary Fresnel number N, and give comparisons for various cases of N. Egner and Hell also show that their theory is equivalent to that of Török et al. (1995) when $N \to \infty$.

We chose the Török et al. (1995) model for our PSF simulations. The physical layout for this model is shown in Fig. 4.3. Since this model modifies the Debye–Wolf integral it is also Fourier transform based, but it uses spherical polar co-ordinates rather than Cartesian co-ordinates as used previously in this chapter.

We once again assume that the input beam is plane polarised. The refractive index change is introduced at a distance d from the Gaussian focal point O. We use the Debye–Wolf integral in the first medium to calculate the electric field at the plane of the refractive index change using the superposition of plane waves, which has the form of a Fourier transform. This field is then transformed across the interface by applying the Fresnel refraction formulas to the plane waves which make up the field. The field in the second medium is then

propagated from this boundary to the observation point P by once again calculating the superposition of plane waves.

For an observation point P that is far away from the aperture, we arrive at the following expressions for the components of the electromagnetic field:

$$\begin{aligned}
E_x &= +\frac{\mathrm{i}K}{2\pi}\int_0^{\alpha}\int_0^{2\pi}(\cos\theta_1)^{\frac{1}{2}}(\sin\theta_1) \\
&\quad \times[(\tau_p\cos\theta_2+\tau_s)+(\cos 2\phi)(\tau_p\cos\theta_2-\tau_s)] \\
&\quad \times\exp\left\{\mathrm{i}k_0\left[r_p\kappa+\Psi(\theta_1,\theta_2,-d)+\varphi(\theta_1,\phi)\right]\right\}\mathrm{d}\theta_1\mathrm{d}\phi\,, \\
E_y &= +\frac{\mathrm{i}K}{2\pi}\int_0^{\alpha}\int_0^{2\pi}(\cos\theta_1)^{\frac{1}{2}}(\sin\theta_1)(\sin 2\phi) \\
&\quad \times(\tau_p\cos\theta_2-\tau_s) \\
&\quad \times\exp\left\{\mathrm{i}k_0\left[r_p\kappa+\Psi(\theta_1,\theta_2,-d)+\varphi(\theta_1,\phi)\right]\right\}\mathrm{d}\theta_1\mathrm{d}\phi\,, \\
E_z &= -\frac{\mathrm{i}K}{\pi}\int_0^{\alpha}\int_0^{2\pi}(\cos\theta_1)^{\frac{1}{2}}(\sin\theta_1)\tau_p\sin\theta_2\cos\phi \\
&\quad \times\exp\left\{\mathrm{i}k_0\left[r_p\kappa+\Psi(\theta_1,\theta_2,-d)+\varphi(\theta_1,\phi)\right]\right\}\mathrm{d}\theta_1\mathrm{d}\phi\,. \qquad (4.33)
\end{aligned}$$

In these expressions,

$$K=\frac{k_2^2 f l_0}{2k_1}\,, \qquad (4.34)$$

α is the aperture half angle, the subscripts 0 , 1 , and 2 refer to vacuum, the first material, and the second material respectively, θ is the azimuthal pupil angle, ϕ is the polar pupil angle, τ_p and τ_s are the Fresnel coefficients, $k=2\pi/\lambda$ is the wave number, n is the refractive index, r_p is the length of the position vector (r_p,θ_p,ϕ_p) pointing from the origin (at the focal point) to the observation point, f is the focal length of the lens, l_0 is an amplitude factor, and

$$\kappa=n_1\sin\theta_1\sin\theta_p\cos(\phi-\phi_p)+n_2\cos\theta_2\cos\theta_p \qquad (4.35)$$

and

$$\Psi(\theta_1,\theta_2,-d)=-d(n_1\cos\theta_1-n_2\cos\theta_2) \qquad (4.36)$$

define the co-ordinate transform between the two materials. $\varphi(\theta_1, \phi)$ is the CPM aberration function across the aperture of the lens from Eq. (4.3). The Fresnel coefficients are defined in the usual way

$$\tau_s = \frac{2\sin\theta_2\cos\theta_1}{\sin(\theta_1+\theta_2)} \tag{4.37}$$

$$\tau_p = \frac{2\sin\theta_2\cos\theta_1}{\sin(\theta_1+\theta_2)\cos(\theta_1-\theta_2)}\,. \tag{4.38}$$

4.2.6 Implications of the Debye approximation

The high aperture theory in this chapter depends on the Debye approximation. High aperture microscope lens focusing generally has a high Fresnel number. But with increasing angular apertures, it becomes difficult to place the back aperture exactly in the back focal plane. It is also difficult to place any pupil filters exactly in the back focal plane because that plane may be physically within the objective casing. These constraints prevent high aperture lenses from having an infinite Fresnel number.

If the Fresnel number is finite, then increasing object distances from the focal plane and increasing aberrations will start to push the Fresnel number down into the region where the Debye approximation is no longer accurate and we should turn to more rigorous solutions of Maxwell's equations. For example we could incorporate a CPM into the Egner et al. (1998) model for specimen refractive index change.

In addition, for full accuracy we should propagate the CPM from its position behind the lens through to the back focal plane before applying it as a pupil transmission filter in the model presented here. We have attempted Rayleigh–Sommerfield propagation of the CPM and we found the computation took an impractical length of time to converge for distances on the order of millimetres.

Gan et al. (1997) simulated a similar situation using Fresnel propagation with annular masks for confocal imaging and encountered mixed results. The transverse resolution of the system changes very little with increasing distance of the annulus from the back focal plane. Meanwhile, the axial response becomes asymmetric, but also becomes sharper. A similar angular spectrum model of CPM propagation would be useful in evaluating the impact of the CPM distance from the back focal plane of the objective.

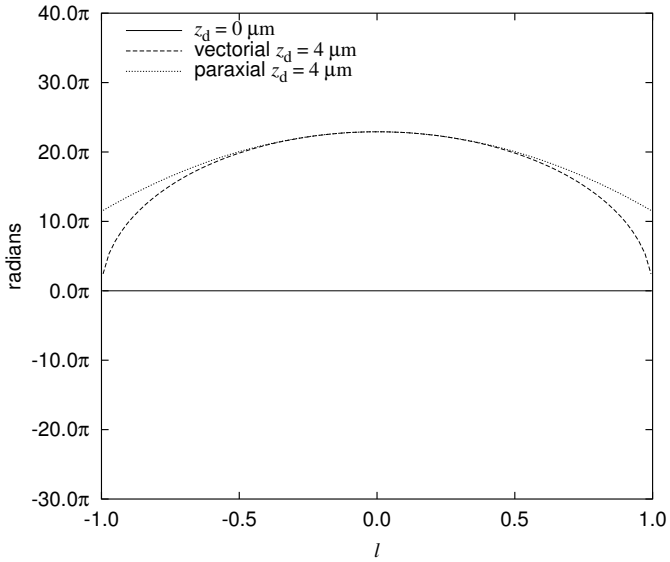

(a)

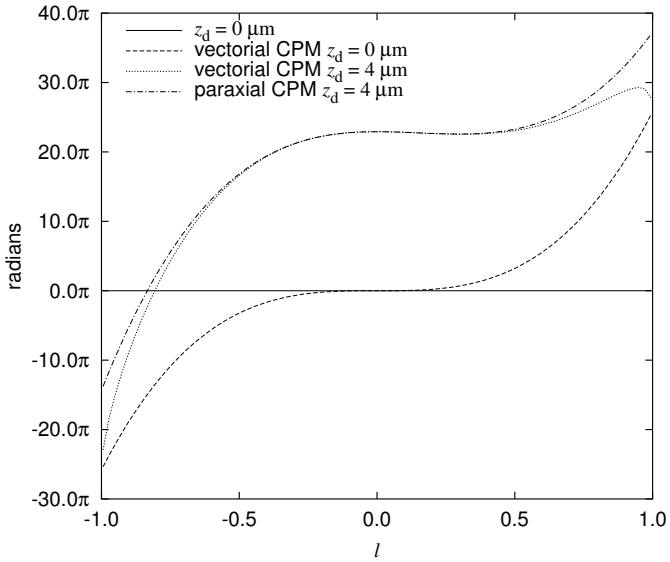

(b)

Figure 4.4: Pupil phase for defocus and the CPM, for a square aperture sized to just fit inside a circular pupil with $\alpha = \pi/2$. Line plots are shown along the axis $m = n$, with $l = \sqrt{m^2 + n^2}$ as the radial pupil co-ordinate. (a) Comparison of paraxial defocus Eq. (4.30) with high aperture defocus Eq. (4.28). (b) Combination of a strong CPM with defocus. The basic cubic shape is maintained even with high defocus for both the paraxial and high aperture defocus models.

Table 4.1: Optical parameters used for PSF and OTF simulations

Optical parameter	Simulation value
Wavelength	530 nm
Numerical aperture	NA $= 1.3$ oil
Oil refractive index	$n_1 = 1.518$
Water refractive index	$n_2 = 1.33$
Aperture half angle	$\alpha = \pi/3$
Pupil shape	Square
Pupil width	7.1 mm
Cubic phase strength	25.8 waves peak to valley

4.3 Numerical integration issues

We have applied both the pupil projection integral Eq. (4.32) and the refractive index change integral Eq. (4.33) to simulate our wavefront coding experiments (described in chapter 5), using the parameters given in Table 4.1. Both models involve a 2D integral over the pupil.

The key effects we were interested in were all phase variations across the pupil: defocus, refractive index change, and the CPM. Figure 4.4 shows the strength of pupil phase variations for the cases we wanted to model. These large phase variations across the pupil produce an integrand with many oscillations, since the phase is wrapped at 2π intervals by the exponential. The most straightforward method for dealing with rapid oscillations in the integrand is to increase the number of sample points taken during integration, as discussed in detail by Mansuripur (1989).

The pupil projection integral was evaluated using a 2D fast Fourier transform in Cartesian co-ordinates. The kernel of the Fourier transform was the 2D projected pupil $\mathbf{P}'_+(m,n)$ from Eq. (4.29), using Eq. (4.21) for the aperture cutoff. The pupil was sampled using a uniformly spaced grid of $N \times N$ complex numbers. We then padded this array out to $4N \times 4N$ to allow for sufficiently fine sampling of the resulting PSF, before employing the algorithms in Eq. (4.32) and Eq. (4.31) to calculate the PSF and OTF respectively. Each execution of Eq. (4.31) with $N = 1024$ took about 8 minutes on a Linux Athlon 1.4 GHz computer with 1 GB of RAM. The results presented were calculated with either $N = 512$ or $N = 1024$. Details of the projected pupil integration code and the steps taken to verify it are set out in appendix B.

The refractive index change integral samples the pupil in spherical polar co-ordinates. Debye–Wolf integrals are often evaluated in spherical polar form when the optical system

being modelled has cylindrical symmetry about the optical axis. Even for linearly polarised illumination the integration over ϕ can be solved analytically in terms of Bessel functions, as long as the pupil function is cylindrically symmetric, leaving only a single integration to be done numerically.

Due to the rectangular nature of the CPM, this simplification cannot be made, and both dimensions must be integrated numerically. For small numbers of sample points, spherical polar co-ordinates will produce aliasing along the edge of the square pupil. However, we sampled the pupil very finely to capture the strong phase variations, which also meant aperture edge shape aliasing effects were minimised.

A 2D Gauss–Legendre approach (Press et al., 1993) was used to evaluate Eq. (4.33). This involved dividing the integrand up into sections of varying length, and applying to each section a weight which is inversely proportional to the length. This was repeated for the second dimension of the integral. Gauss–Legendre samples the edges of the integrand more closely than the middle, which is appropriate as our integrand changes more rapidly at the edges, as demonstrated in Fig. 4.4.

The number of integrand sample points N^2 required for accurate integration increases with both the strength of the cubic phase function, and with the distance PO of the observation point from the Gaussian focal point (see Fig. 4.3).

To determine the value of N required to achieve the accuracy we desired, we took a sample observation point, and tested the convergence of the integral result at that point. First we stored the result calculated with a very large number of iterations ($N = 2000$, giving $N^2 = 4 \times 10^6$ sample points) and then we reduced N to a much lower value ($N = 100$) and steadily increased it, until the result converged with desired accuracy to match the value found at $N = 2000$. The results shown below were calculated with $N = 400$. The calculation of a 250×250 wz axial slice through the PSF with $N = 400$ took about 5 hours on our Linux Athlon system (w is a transverse co-ordinate along the line $x = y$). Details of the refractive index change integration code and the steps taken to verify it are set out in appendix B.

All the results presented in the next section were calculated using the projected pupil code, apart from Fig. 4.8 which used the refractive index change code. The projected pupil code was useful for calculating transverse planes of the PSF, and the corresponding OTFs, with a very fine sampling. Although the refractive index change code was at least $10\times$ slower for producing equivalent transverse plane results, it was more useful for line plots or wz sections, as each observation point was evaluated independently, whereas the pupil projection code had to calculate a whole transverse plane for each z step. Such wz sections are convenient as spherical aberration produces features which are more clearly seen in wz

sections than in transverse planes. The projected pupil integral could be made much more efficient for calculating *wz* PSF sections by projecting the pupil along a line orthogonal to the axis, for example along the *m* axis, rather than along the *s* axis as done in Eq. (4.12) (Larkin, 1999).

4.4 Simulation results

We begin by exploring the effect of defocus on the paraxial and vectorial frequency content in a widefield system. We define a widefield system as having a circular pupil with no CPM. The discrepancy between the two models is shown in Fig. 4.5(a) for the focal plane widefield OTF. We show a similar comparison of the defocused widefield OTF in Fig. 4.5(b). We can see there is a major difference in the predictions of the two models, especially at high frequencies. The discrepancy between the models increases markedly with defocus.

Wavefront coding relies on an inverse filter to deconvolve the blurred image and retrieve a high resolution EDF image. The inverse filter for our experiments was derived from a paraxial simulation of the widefield (no CPM) OTF and the measured CPM OTF. The discrepancy between the vectorial and paraxial results in Fig. 4.5(a) implies that the best deconvolution accuracy will be obtained by using the simulated vectorial OTF when constructing the digital inverse filter for a high aperture system.

The CPM is designed to produce focus invariance. In practice, for both simulations and experiments, a CPM strength of 25.8 waves peak to valley provided a workable EDF range of about $8\,\mu\text{m}$. Since the CPM PSF is symmetric on either side of the focal plane, the end points of this EDF range are at $z_\text{d} = \pm 4\,\mu\text{m}$. Fig. 4.5(b) illustrates the dramatic changes introduced by this amount of defocus in a widefield system.

Our models assume the illumination is linearly polarised. This produced a minor asymmetry in the PSF and OTF results, with slightly different responses along the *x* and *y* axes. However, this effect tended to be overshadowed by other factors, so we have not explicitly emphasised it in the results shown here.

We now investigate the simulated behaviour of a CPM system according to our vectorial theory. Figures 4.6 and 4.7 show the vectorial high aperture PSF and OTF for the transverse focal plane with a strong CPM. The dramatic effect of the CPM is clearly visible in the PSF results. The shape of the CPM PSF in Fig. 4.6(c) has a grid–like structure which is quite different to the normal point focus produced without a CPM shown in Fig. 4.6(a). EDF behaviour is apparent in the barely visible change between Fig. 4.6(c) and 4.6(d), compared with the usual rapid blurring defocus produces as seen in Fig. 4.6(b).

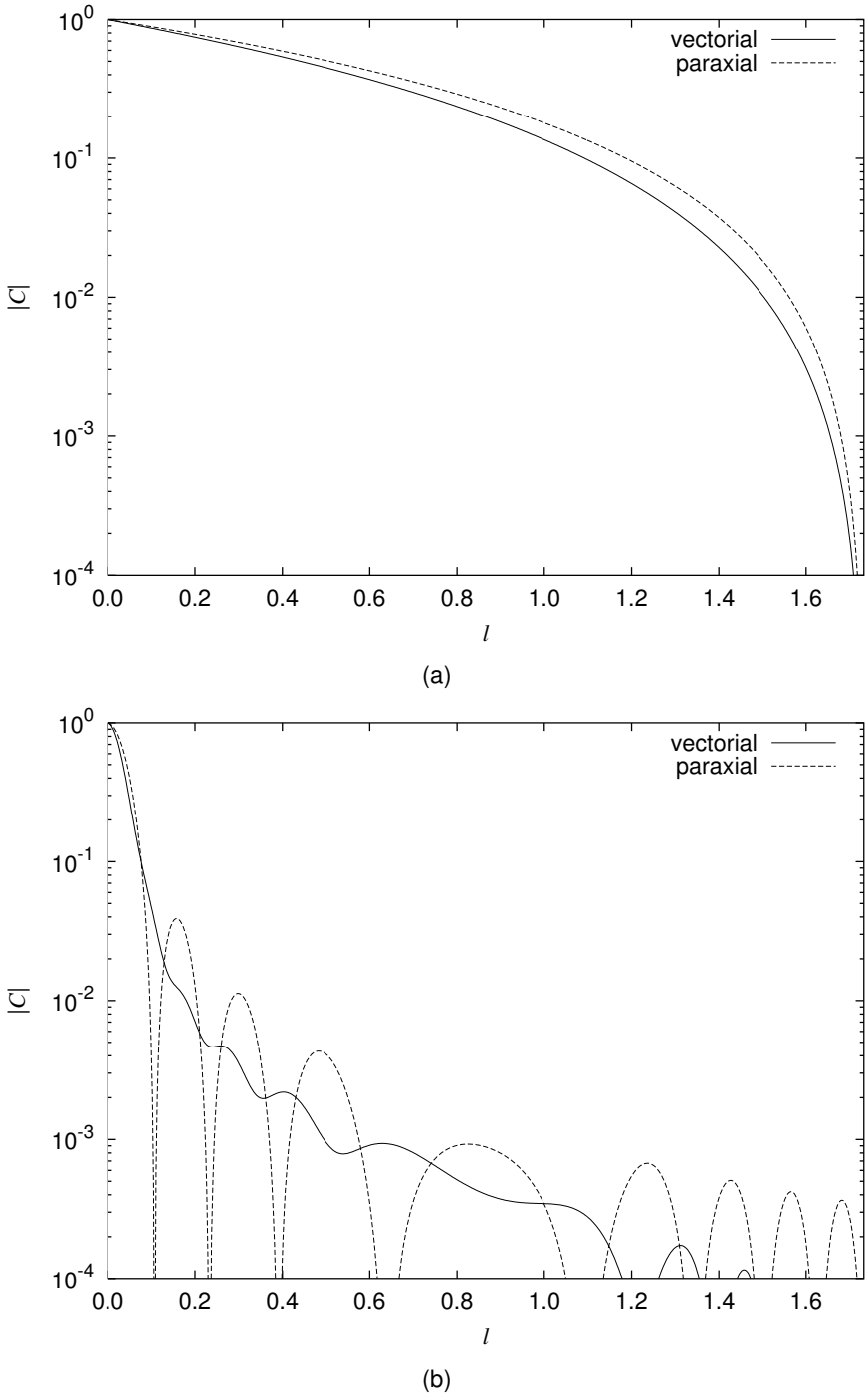

Figure 4.5: A comparison of widefield (no CPM) OTFs using our vectorial (*solid line*) and paraxial (*dashed line*) simulations: (a) in–focus at $z_d = 0\,\mu m$ and (b) defocused to $z_d = 4\,\mu m$. For a diagonal line through the OTF along $m = n$, we have plotted the value of the 2D projected OTF for each case. While the structure of the in–focus OTF curves is similar for the two models, the relative difference between them increases with spatial frequency, reaching over 130% at the cutoff. Once defocus is applied, the two models predict markedly different frequency response in both structure and amplitude.

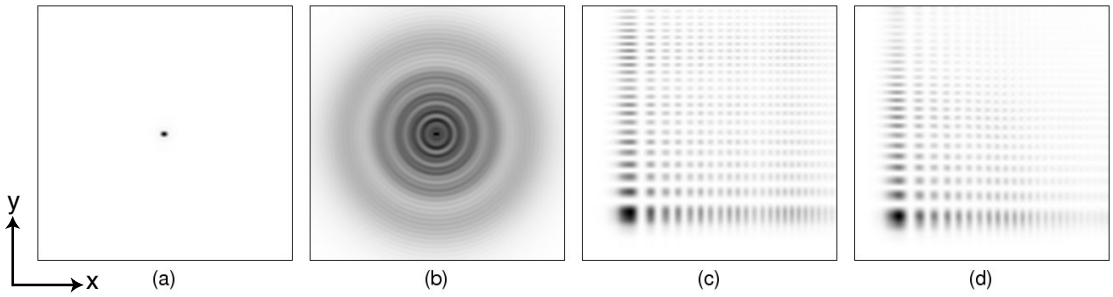

Figure 4.6: The simulated vectorial high aperture PSF for widefield and wavefront coding, showing the effect of defocus: (a) widefield in–focus $z_d = 0\,\mu m$, (b) widefield defocused $z_d = 4\,\mu m$, (c) CPM in–focus $z_d = 0\,\mu m$, (d) CPM defocused $z_d = 4\,\mu m$. This amount of defocus introduces very little discernible difference between the CPM PSFs. Indeed paraxial CPM simulations (not shown here) are also similar in structure. See Fig. 5.4 to compare with measured PSFs. The incident polarisation is in the x direction. The images are normalised to the peak intensity of each case. Naturally the peak intensity decreases with defocus, but much less rapidly in the CPM system. The area shown for each PSF is $13\,\mu m \times 13\,\mu m$.

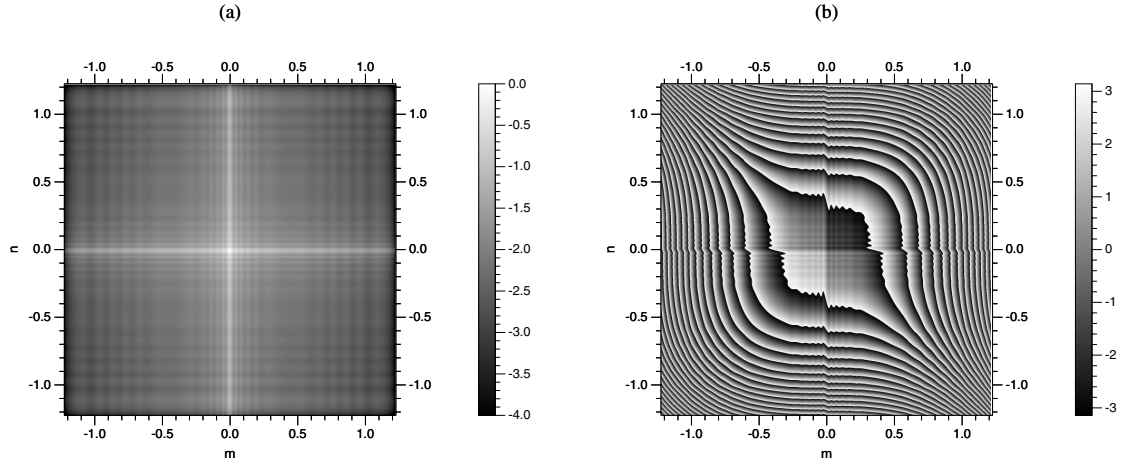

Figure 4.7: The simulated vectorial high aperture in–focus CPM OTF: (a) is the magnitude of the OTF in $\log_{10}$ scale, and (b) is the wrapped phase in radians. While the frequency response is much stronger along the m and n axes, the magnitude remains above 10^{-3} throughout the spatial frequency cutoff. Compensating for the OTF phase is important in digital restoration. The phase of the OTF is very similar to the cubic phase in the pupil. The $z_d = 4\,\mu m$ defocused OTF (not shown) has a similar appearance to this in–focus case. See Fig. 5.5 to compare with the measured OTFs.

The CPM OTF in Fig. 4.7 shows that frequency responses are strongest along the m and n axes, while the phase varies strongly across the OTF. Neither of these features are present in the widefield OTF when no CPM is applied.

Figure 4.8 shows axial slices through the simulated widefield and CPM PSF for different depths below a refractive index change. The characteristic "banana" shape of the axial CPM PSF is clearly shown in Fig. 4.8(a). The focal spot of widefield focusing, shown for comparison in Fig. 4.8(d), is stretched axially by the CPM to become a line with increasing curvature away from the focal plane. This curvature will produce a slight warping of the EDF image away from a strictly perspective projection, even though the bending is minor within the EDF range $z_\mathrm{d} = \pm 4\,\mu\mathrm{m}$. Also notable is that there are two maxima (shown in red at $z_\mathrm{d} \approx \pm 9\,\mu\mathrm{m}$) in the CPM pattern. Although these maxima proved to be numerically stable, we have been unable to confirm or deny them in measured CPM PSFs.

The addition of a refractive index change, shown in Figs. 4.8(b-c), shifts the CPM PSF towards the lens, rotates it slightly clockwise as viewed in these slices, and distorts the transverse tail of the PSF. However, after taking into account the axial shift, the central $8\,\mu\mathrm{m}$ axial region of the spherically aberrated PSF in Fig. 4.8(b) has a similar structure to the CPM PSF in Fig. 4.8(a) without spherical aberration.

This implies that for the simulated conditions the CPM aberration dominates the aberrations caused by a refractive index change, and that imaging with the CPM will be somewhat resistant to both defocus and spherical aberration. A similar resistance to spherical aberration has been reported for paraxial imaging with logarithmic wavefront coding filters (Mezouari and Harvey, 2003). However, just as with defocus, there are limits to how much spherical aberration the CPM can cope with. The $d = 40\,\mu\mathrm{m}$ case in Fig. 4.8(c) shows increased distortion of the CPM PSF, which implies that the final deconvolved image would be visibly degraded.

These results also allow us to compare the relative peak intensity of the different cases. The widefield PSF slice shown in Fig. 4.8(d) has twice the peak intensity of the $d = 40\,\mu\mathrm{m}$ widefield case shown in Fig. 4.8(f), and 30 times the peak intensity of the CPM PSF slices in Figs. 4.8(a-c). This dramatic reduction in peak intensity caused by the CPM is inevitable when spreading the focused light over a much longer focal range, and is the chief reason for the reduction in SNR when using a CPM for EDF imaging. However, the $d = 40\,\mu\mathrm{m}$ CPM PSF in Fig. 4.8(c) still has 85% of the peak intensity of the unaberrated CPM PSF in Fig. 4.8(a), which again indicates the resistance the CPM PSF has against spherical aberration.

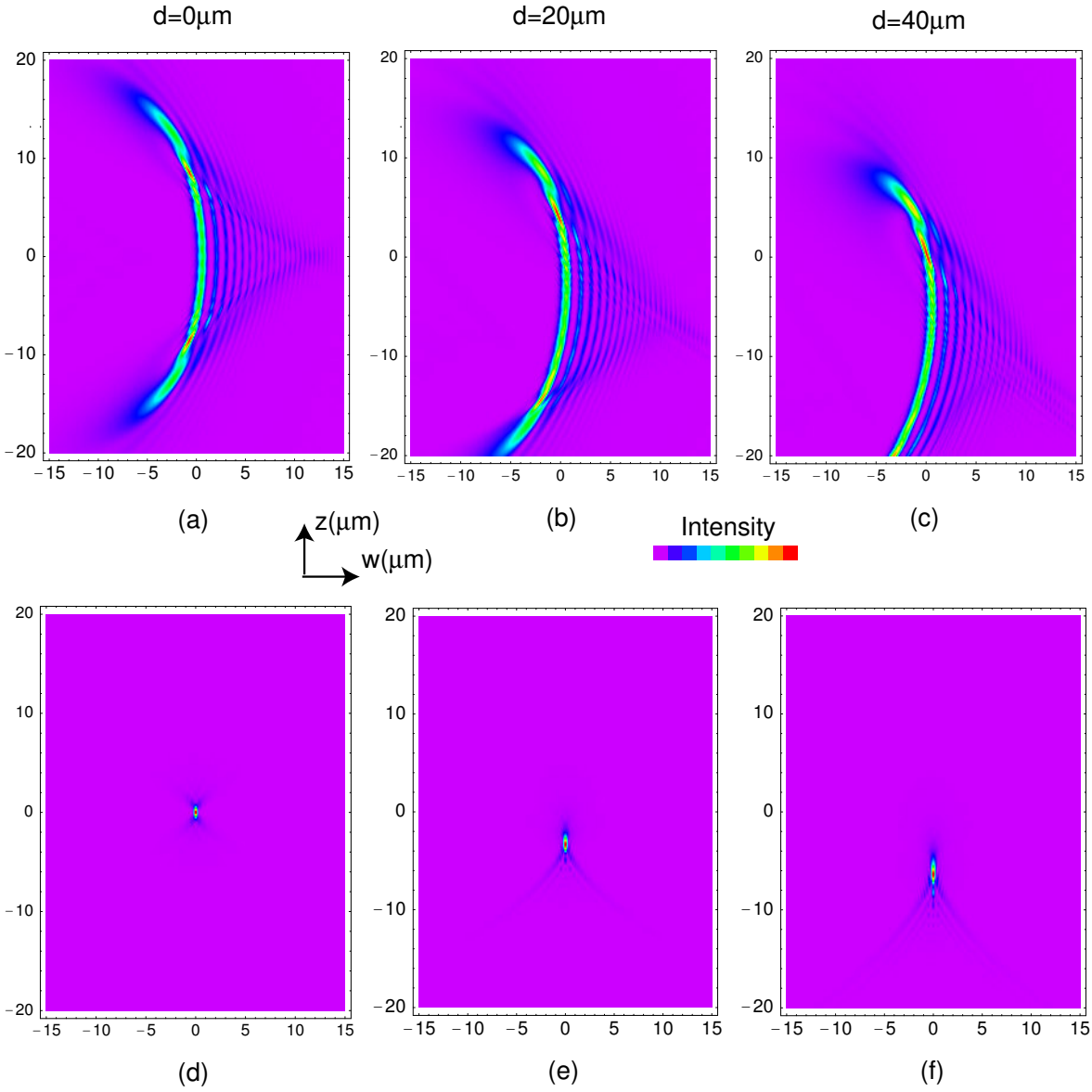

Figure 4.8: The effect of a refractive index change on axial wz slices through the PSF for CPM and widefield cases, using a vectorial model. The transverse co-ordinate w runs along the line $x = y$. The top row shows the CPM axial "banana" shape with (a) no refractive index change, (b) focal depth $d = 20\,\mu\text{m}$ below the refractive index boundary, and (c) $d = 40\,\mu\text{m}$. The bottom row shows widefield (yet square aperture for Fig. 4.8 only) PSFs for (d) no refractive index change, (e) $d = 20\,\mu\text{m}$, and (f) $d = 40\,\mu\text{m}$. These simulations can be compared against the measured CPM PSF shown in Fig. 5.7.

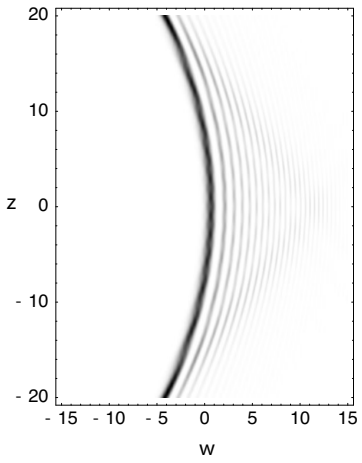

Figure 4.9: Axial slice through the paraxial CPM PSF along the same *wz* plane as Fig. 4.8. The paraxial PSF is axially stretched in comparison with the vectorial case, with no blurring visible in the paraxial PSF for the focal range shown. The paraxial case also shows a simpler transverse pattern than the vectorial case.

The CPM PSF does have some interesting similarities with the spherically aberrated PSF. By comparing Fig. 4.6(c) with Figs. 1–3 in Sheppard and Török (1997a), we can see that the structure of the CPM PSF in the transverse plane is similar to the structure of the spherically aberrated PSF in the axial plane.

The axial slice through the vectorial CPM PSF in Fig. 4.8(a) also provides a good basis for comparison with the paraxial approximation shown in Fig. 4.9. As is to be expected, the paraxial results display a simpler PSF structure than the vectorial results. The paraxial approximation is relatively stretched in the axial direction. A longer EDF range would be predicted from the paraxial model than from the vectorial model.

Returning to frequency space, the defocused $z_{\mathrm{d}} = 4\,\mu\mathrm{m}$ vectorial CPM OTF (not shown) and the paraxial in–focus and defocused $z_{\mathrm{d}} = 4\,\mu\mathrm{m}$ CPM PSFs and OTFs (not shown) are all qualitatively similar to the vectorial $z_{\mathrm{d}} = 0\,\mu\mathrm{m}$ case shown in Figs. 4.6 and 4.7. However, if we perform a quantitative comparison we see that there are marked differences. Figure 4.10 shows the relative strength of the CPM OTF for a diagonal cross section. For the in–focus case, the differences between the vectorial and paraxial models are similar to those for the widefield OTF in Fig. 4.5(a), with up to 100% difference at high spatial frequencies. However, as the defocus increases, the structure of the vectorial CPM OTF begins to diverge from the paraxial model, as does the point where the OTF strength drops below 10^{-4}. This is still a much lower discrepancy than the widefield model for similar amounts of defocus, as is clear by comparison with Fig. 4.5.

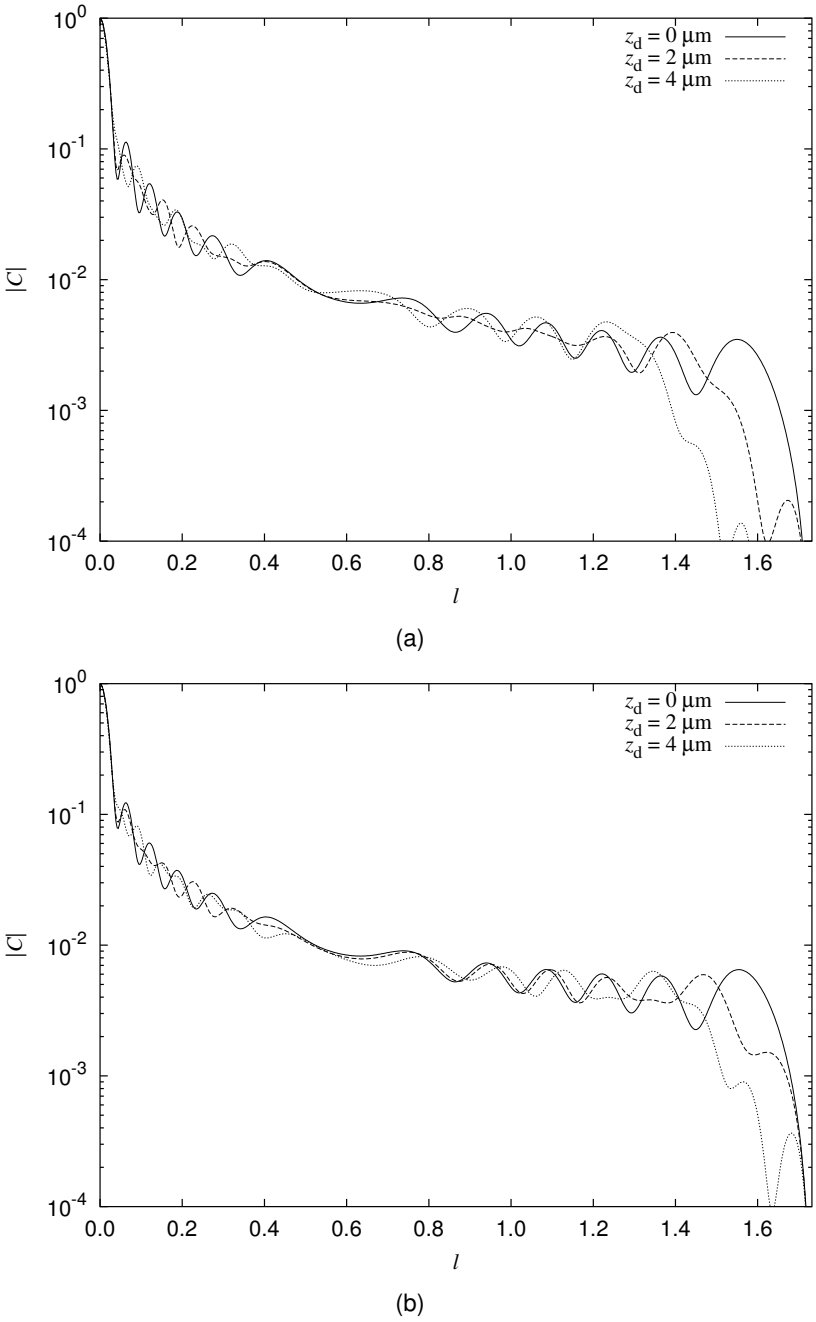

Figure 4.10: The magnitude of the wavefront coding OTF for the (a) vectorial and (b) paraxial models, plotted along a diagonal line $m = n$ through the OTF, with different values of defocus: in–focus $z_d = 0\,\mu m$ (*solid line*), defocused $z_d = 2\,\mu m$ (*dashed line*), defocused $z_d = 4\,\mu m$ (*dotted line*). In common with the widefield system, the models differ the most at high spatial frequencies, up to 100% at large l for the in–focus case. As defocus increases, the differences become more extreme, with the vectorial simulation predicting a quicker reduction in effective cutoff.

These plots allow us to assess the SNR requirements for recording images with maximum spatial frequency response. For both widefield and CPM systems, the experimental dynamic range will place an upper limit on the spatial frequency response. In widefield a 10^3 SNR will capture nearly all spatial frequencies up to the cutoff (see Fig. 4.5(a)), allowing for good contrast throughout. Further increases in SNR will bring rapidly diminishing returns, only gradually increasing the maximum spatial frequency response.

For CPM imaging the same 10^3 SNR will produce good contrast only for low spatial frequencies, with the middle frequencies lying less than a factor of ten above the noise floor, and the upper frequencies dipping below it. However, a SNR of 10^4 will allow a more reasonable contrast level across the entire OTF. For this reason, a 16 bit camera, together with other noise control measures, is needed for a CPM system to achieve the full resolution potential of high aperture lenses. This need for high dynamic range creates a trade off for rapid imaging of living specimens — faster exposure times will reduce the SNR and lower the resolution.

Arguably the most important OTF characteristic used in EDF digital deconvolution is the phase. As can be seen from Fig. 4.7 the CPM OTF phase oscillates heavily due to the strong cubic phase. This corresponds to the numerous contrast reversals in the PSF. The restoration filter is derived from the OTF, and therefore accurate phase in the OTF is needed to ensure that any contrast reversals are correctly restored.

A comparison of the amount of OTF phase difference between focal planes for the vectorial and paraxial models is shown in Fig. 4.11. We calculated this using the unwrapped phase, obtained by taking samples of the OTF phase along a line $m = n$, then applying a 1D phase unwrapping algorithm to those samples. After finding the unwrapped phases for different focal planes, $z_\mathrm{d} = 2\,\mu\mathrm{m}$ and $z_\mathrm{d} = 4\,\mu\mathrm{m}$, we then subtracted them from the in-focus case at $z_\mathrm{d} = 0\,\mu\mathrm{m}$.

Ideally the OTF phase difference between planes within the EDF range should be very small. It is clear however that there are some notable changes with defocus. Both paraxial and vectorial models show a linear phase ramp, with oscillations.

This linear phase ramp is predicted by the stationary phase approximation to the 1D CPM OTF, Eq. (A12) in Dowski and Cathey (1995). Since the Fourier transform of a phase ramp is a lateral displacement, this gives a lateral motion of the PSF for different transverse planes. In practice this has the effect of giving a slightly warped projection. A mismatch between the microscope OTF and the inverse filter of this sort will simply result in a corresponding lateral offset of image features from that transverse plane of the object. Otherwise spatial frequencies should be recovered normally.

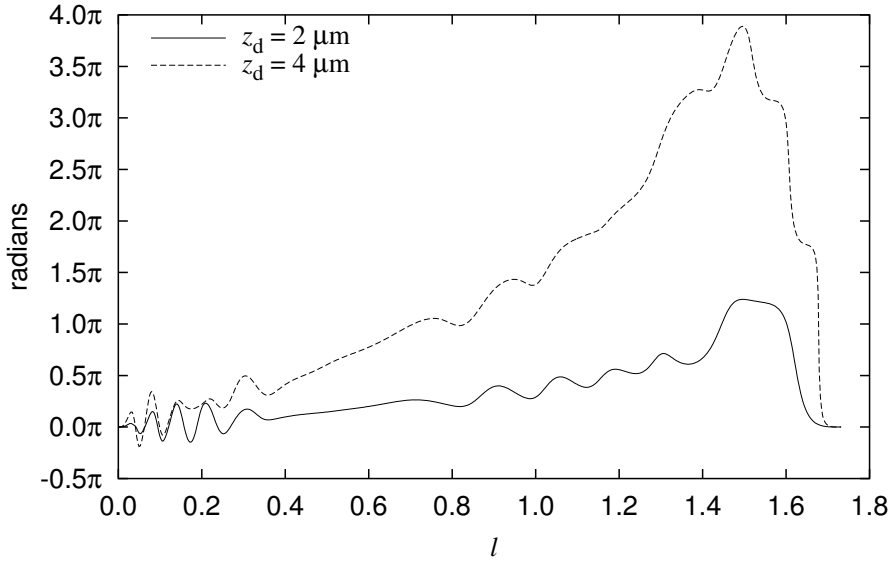

(a)

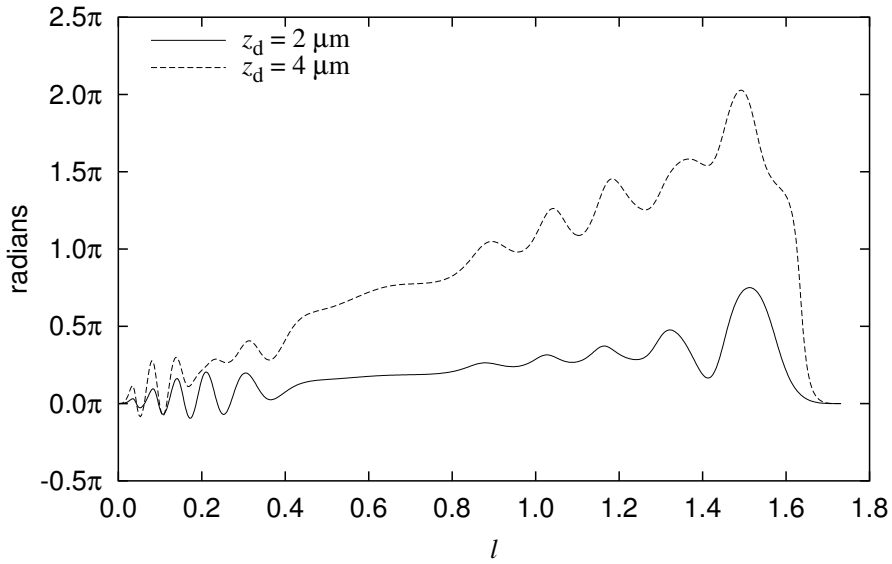

(b)

Figure 4.11: The relative OTF phase angle between focal planes, along a diagonal line $m = n$ through the CPM OTF, for (a) the vectorial model, and (b) the paraxial model. For both (a) and (b) we show two cases, the unwrapped phase difference between the $z_d = 0\,\mu\text{m}$ and $z_d = 2\,\mu\text{m}$ OTF (*solid line*) and the unwrapped phase difference between $z_d = 0\,\mu\text{m}$ and $z_d = 4\,\mu\text{m}$ (*dashed line*). All cases show a linear phase ramp with an oscillation of up to $\pi/2$. This phase ramp corresponds to a lateral shift of the PSF. The vectorial case shows an additional curvature and larger overall phase differences of up to π radians (or 0.5 waves) across the spectrum.

The oscillations will have a small effect; they are rapid and not overly large in amplitude: peaking at $\pi/2$ for both vectorial and paraxial models. This will effectively introduce a source of noise between the object and the final recovered image. Whilst these oscillations are not predicted by the stationary phase approximation, they are still evident for the paraxial model.

The most dramatic difference between the two models is in the curvature of the vectorial case, which is particularly striking in the $z_d = 4\,\mu m$ plane, and not discernible at all in the paraxial case. The primary effect of this curvature will be to introduce some additional blurring of specimen features in the $z_d = 4\,\mu m$ plane, which the inverse filter will not be able to correct. The total strength of this curvature at $z_d = 4\,\mu m$ is about π across the complete $m = n$ line, or 0.5 waves, which is a significant aberration.

4.5 Discussion

The CPM produces a strong aberration which appears to overshadow the effects of defocus, spherical aberration and vectorial high aperture focusing. The paraxial approximation of CPM focusing certainly loses accuracy for larger values of defocus when compared with the vectorial model, but not nearly so much accuracy is lost as in the paraxial approximation of widefield focusing. Yet significant differences remain between the two models, notably 0.5 waves of curvature aberration in the vectorial case, and this suggests that vectorial high aperture theory will be important in the future design of high aperture wavefront coding systems.

We can also look at the two models as providing an indication of the difference in performance of CPM wavefront coding between low aperture and high aperture systems. The curvature aberration in the high aperture case varies with defocus, which means that it cannot be incorporated into any single-pass 2D digital deconvolution scheme. This effectively introduces an additional blurring of specimen features in planes away from focus, lowering the depth of field boost from what can be achieved with the same CPM strength in a low aperture wavefront coding system.

In general the CPM performs a little better at low apertures for EDF applications. But the high aperture CPM system still maintains useful frequency response across the full spectrum of an equivalent widefield system, especially for on–axis frequencies. With a CPM strength of 25.8 waves, this steady frequency response is only just starting to decay at either end of an $8\,\mu m$ EDF working range, which is a dramatic boost on the $1\,\mu m$ depth of field predicted for a 1.3 NA lens in widefield (see Fig. 1.1).

Why does the CPM create such a stable pattern under challenging conditions? Nye (1999) points out that creating a small spot using perfect lens focusing is actually highly unnatural and unstable. The smallest perturbation to the system creates dramatic changes in the focal spot. Natural focusing, on the other hand, creates more stable concentrations of energy, as seen in the bright lattice of lines at the bottom of a swimming pool on a sunny day. Large changes in the water surface do not fundamentally disrupt the linear shape of the focused light.

A major theme of this thesis is combining optical and digital design to find new solutions to imaging problems. Within a hybrid system, the linear focus shape seen in Fig. 4.8(a) turns out to be a useful and resilient way of probing the specimen when maintaining the absolute maximum dynamic range and resolution is not the first priority. Ironically, we have used wavefront coding as part of an advanced hybrid optical–digital microscope to deliberately design a system which is robust against defocus effects, only to find that nature got there first.

Chapter 5

High aperture cubic phase experiments

A wavefront coding microscope is a relatively simple modification of a modern microscope. A system overview is shown in Fig. 5.1.

The key optical element in a wavefront coding system is the waveplate. This is a transparent molded plastic disc with a precise aspheric height variation. Placing the waveplate in the back focal plane of a lens introduces a phase aberration designed to create invariance in the optical system against some chosen imaging parameter. A cubic phase function on the waveplate is useful for microscopy, as it makes the low aperture optical transfer function (OTF) insensitive to defocus.

While the optical image produced is quite blurry, it is uniformly blurred over a large range along the optical axis through the specimen (Fig. 1.2). From this blurred intermediate image, we can digitally reconstruct a sharp EDF image, using a measured PSF of the system and a single step deconvolution. The waveplate and digital filter are chosen to match a particular objective lens and imaging mode, with the digital filter further calibrated by the measured PSF. Once these steps are carried out, wavefront coding works well for any typical specimen.

The EDF behaviour relies on modifying the light collection optics only, which is why it can be used in other imaging systems such as photographic cameras, without needing precise control over the illumination light. In epi–fluorescence microscopy both the illumination light and the fluorescent light pass through the waveplate. The CPM provides a beneficial effect on the illumination side, by spreading out the axial range of stimulation in the specimen, which will improve the SNR for planes away from best focus.

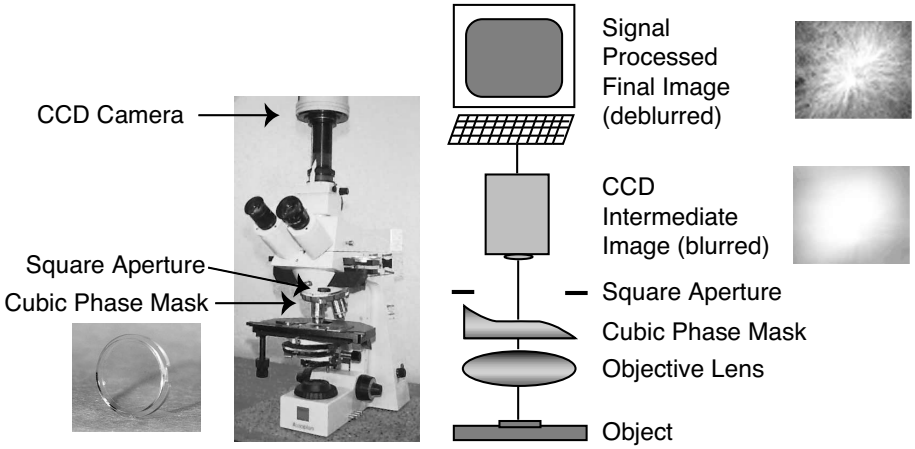

Figure 5.1: An overview of a wavefront coding microscope system. The image-forming light from the object passes through the objective lens and phase mask and produces an intermediate encoded image on the CCD camera. This blurred image is then digitally filtered (decoded) to produce the extended depth of field result. Examples at right show the fluorescing cell image of Fig. 5.8(c) at each stage of the two–step process. At lower left a pair of arrows show where the CPM and square aperture are inserted into the microscope.

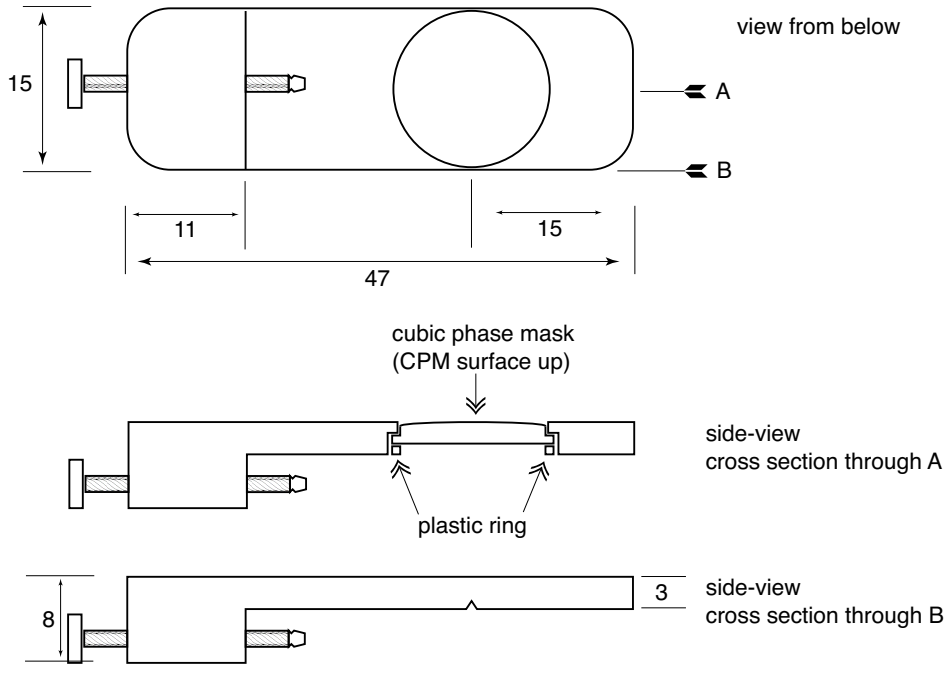

Figure 5.2: Custom CPM mount designed to fit in the DIC slot of a Zeiss Axioplan microscope. The screw allows lateral alignment of the CPM with the square aperture. The mount was designed and built at the University of Sydney by Carol Cogswell and Ken Weigert. All lengths in millimetres.

5.1 Experimental method

The experimental setup followed the system outline shown in Fig. 5.1. We used a Zeiss Axioplan microscope with a Zeiss Plan Neofluar 40x 1.3 NA oil immersion objective. The wavefront coding plate was a rectangular cubic phase function design (CPM 127-R60 Phase Mask from CDM Optics, Boulder, CO, USA) with a peak to valley phase change of 56.6 waves at 546 nm across a 13 mm diameter optical surface. This plate was placed in a custom mount (shown in Fig. 5.2) and inserted into the differential interference contrast slider slot, 4 mm above the objective. The CPM was aligned so that it was centred with the optical axis, covering the back pupil.

A custom square aperture mask was inserted into an auxiliary slot 22 mm above the lens, with the square mask cut to fit inside the 10 mm circular pupil of the objective lens. This square aperture is needed due to the rectangular nature of the CPM function given in Eq. (4.3). The square aperture was rotated to match the *mn* axes of the CPM. After clipping by the square aperture, the CPM strength was reduced to 25.8 waves peak to valley. For comparison, standard widefield fluorescence imaging was performed without the CPM or the square aperture mask in place.

Fluorescent images were taken in epi-fluorescence mode with a mercury lamp (HBO 50 W) and fluorescein isothiocyanate (FITC) fluorescence filters in place. Two cameras were used to record images:

1. A Photometrics cooled camera (CH250) with a Thomson TH 7895 CCD at 12 bit precision. This camera was purchased in 1994. The quantum efficiency is about 40%. The pixels are 19 µm square.

2. A Photometrics Cascade 650 cooled camera (Roper Scientific, USA) with a Texas Instruments TC253 CCD, purchased in 2002. The CCD pixel wells have a maximum count of 27000 (~15 bit) and have a quantum efficiency of 50% for light at 530 nm. The CCD has on–chip gain to avoid readout noise and a 16 bit readout to the PC.

To ensure we were sampling at the maximum resolution of the 1.3 NA lens, a 2.5× eyepiece was inserted just before the camera inside a custom camera mount tube. The tube is shown in Fig. 5.3. This tube allowed precise rotational alignment of the camera, in order to match the CCD pixel array axes with the CPM *mn* axes.

With 100x total magnification, this setup gave a resolution of 190 nm per pixel for the CH250 camera, and 74 nm per pixel for the Cascade camera. The theoretical maximum transverse resolution for a 1.3 NA lens is 220 nm (see Fig. 1.1), for which critical sampling

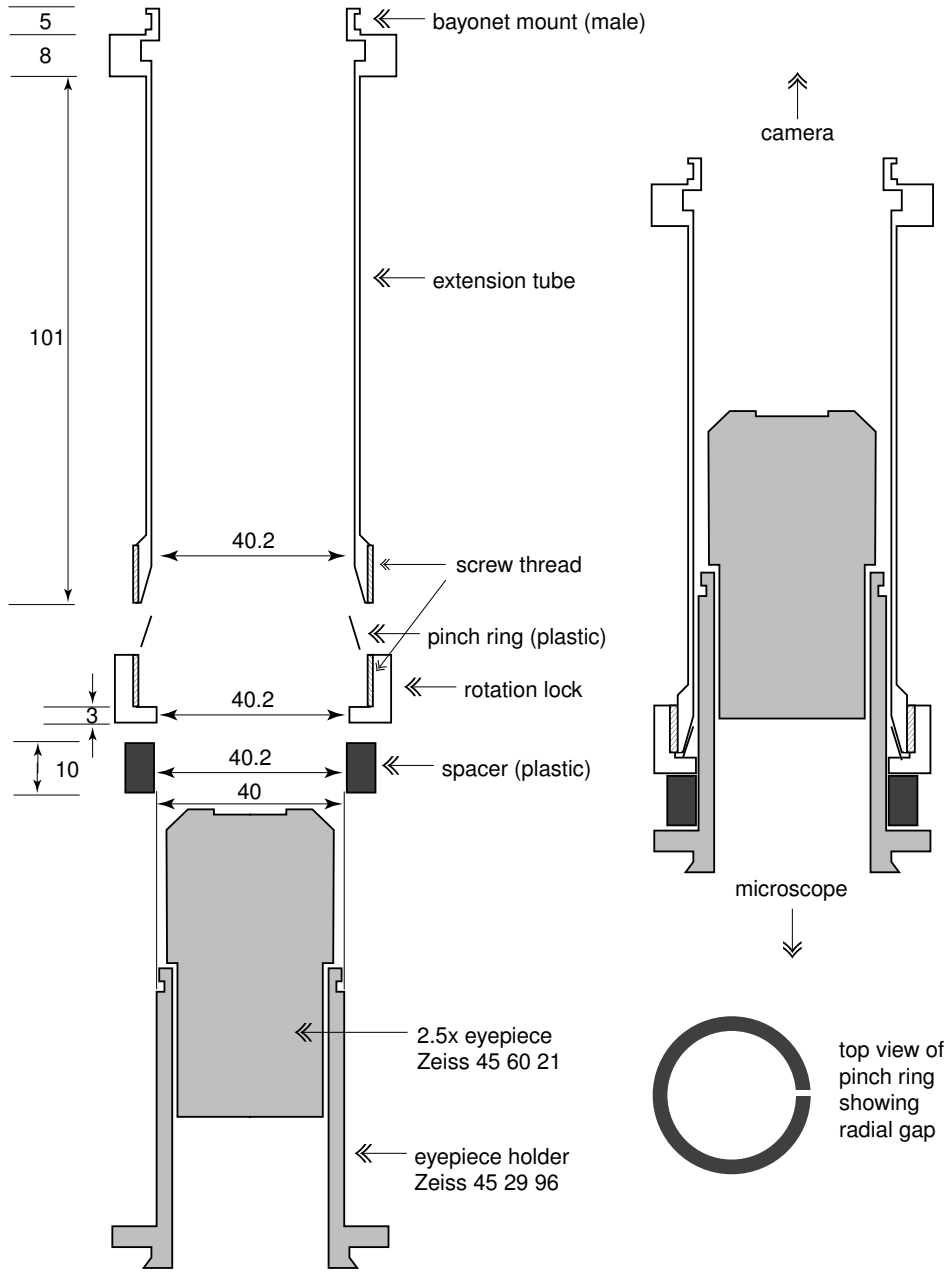

Figure 5.3: Custom camera mounting tube to allow the addition of a 2.5× eyepiece below the camera on a Zeiss Axioplan microscope. The tube can be precisely and repeatably rotated to match the alignment of the CCD camera pixel axes with the CPM. The tube was designed and built at the University of Sydney by Carol Cogswell and Ken Weigert. All lengths in millimetres.

would be 110 nm per pixel. So the CH250 results are slightly under sampled and the Cascade results are slightly over sampled.

Initial alignment of the axes of the CPM with the square aperture and the CCD camera was carried out by visual inspection. Although the CPM was circular, we knew the axis of the CPM from machine drawings. We then fine tuned the alignment by observing the CPM PSF.

5.1.1 PSF measurements

We used both fluorescent beads and a pinhole as approximate point objects for measuring the PSF. The fluorescent bead specimen was designed to fully sample the transverse resolution of the system, using 100 nm polystyrene beads stained with fluorescent dye.

We began with a vial of 100 nm yellow–green fluorescent beads suspended in water (FluoSpheres 505 / 515 F-8803, Molecular Probes, USA). Although these beads were not stained with FITC, they are designed to behave in a similar manner.

The Zeiss FITC filter uses blue incident light and green collection to help isolate the FITC fluorescent response from reflected light and emission from other dyes. The peak absorption and emission wavelengths for FITC are 495 nm and 530 nm respectively. The yellow–green FluoSpheres have corresponding peaks at 505 nm and 515 nm. According to Molecular Probes, these beads are efficiently excited at 488 nm, and show no appreciable bleaching after 30 minutes exposure to a 250 W lamp. Therefore, they are highly suitable for characterising wavefront coding for high aperture fluorescence imaging.

The FluoSphere suspension had 2% solids. This was diluted with distilled water by a factor of 10^9 so that the beads were far enough apart in the specimen to record a PSF from a single bead. A 3 µL drop of the dilute suspension was placed on a 22 mm × 22 mm number 1.5 coverglass. This was left to air dry, in the dark to avoid photo-bleaching of the fluorescent dye.

After drying, a 3 µL drop of mounting medium (InSpeck I-7223 fluorescent intensity calibration kit, refractive index 1.47, Molecular Probes, USA) was placed on a slide, the prepared coverglass was placed on top with the bead side downwards, and the edges of the coverglass were sealed with nail polish. We used a low–fluorescence immersion oil (Zeiss Immersol 518F) when recording the PSF. This oil has a specified refractive index of 1.518 at 23°C.

The mounting medium we used does not set, so in principle the beads could drift through the medium. But during air drying the beads became attached to the coverglass, and in our

experience they remained attached after mounting. This means their position was stable, and not affected by Brownian motion as it would be if they were in solution. It also meant that the refractive index change between the coverglass and the mounting medium would have only a minor impact. However, there were still several potential sources of spherical aberration, due to uncertainty in the refractive index of the immersion oil and the coverglass, together with possible variations of the coverglass thickness.

The second PSF specimen used a metal pinhole to provide a stronger signal, allowing observation of the PSF structure at greater distances from the focal point. This is important because the CPM stretches the PSF over a much wider region, which also decreases the overall strength of the PSF signal compared with widefield. To prepare the pinhole on a slide for observation, the top and bottom of a 1 µm diameter pinhole were coated in immersion oil. The pinhole was mounted on a slide under a number 1.5 coverslip, and then illuminated with a standard lamp in brightfield transmission. By applying a green filter in the base of the microscope we narrowed the bandwidth of the illumination. An analyser in the collection path was oriented to match the *mn* axes of the CPM.

For both the 100 nm fluorescent bead specimens and the pinhole specimen, the 3D PSF was recorded with the Cascade 650 camera by taking a continuous series of transverse images at 1 µm steps through focus. This is a dramatic under sampling of the axial resolution of our 1.3 NA objective, but unfortunately it was the limit of accuracy of the microscope focus control. The OTF for a given focal plane was obtained by taking the 2D fast Fourier transform of the corresponding PSF.

To further increase the SNR of the measured PSF, long exposures, on-chip gain, and frame averaging were all used during image acquisition. The 100 nm bead CPM PSF was recorded by taking the average of 100 frames each with an exposure length of 800 ms, with the Cascade on-chip gain at 2048, which is half the maximum setting of 4096. The pinhole CPM PSF was much brighter, so we set the on-chip gain to 0, and averaged 10 frames with an exposure of 100 ms each for the brightest planes of the PSF. Fewer exposures of shorter length were used to record the widefield PSF as the intensity was much brighter.

These measures substantially reduced random noise in the images of the PSF. The main limit on the SNR for the 100 nm beads was background glare. The most likely source of this glare was reflections from slightly mismatched refractive indexes at interfaces within the specimen, exacerbated by the inevitable crosstalk between the excited and fluoresced light, not all of which is eliminated by the FITC filters.

5.1.2 Biological imaging

To calibrate the system for biological specimen imaging, we measured the PSF in a separate experiment using a 1 µm diameter polystyrene bead stained with FITC dye. Two dimensional PSF images were taken over a focal range of 10 µm in 1 µm steps using the CH250 camera. This PSF measurement (shown in Fig. 6.5 of Arnison et al. (2003)) was used to design an inverse filter using the approach described by Bradburn (1998). The first step in this method was to take the inverse of the modulus of the measured OTF. The OTF was obtained by applying a Fourier transform to the measured PSF. The second step was to incorporate a least squares filter into this inverse filter to suppress noise beyond the spatial frequency cutoff of the optical system. The inverse filter was then used to restore the EDF image by single–step deconvolution.

Each intermediate wavefront coded image of our biological specimens was a single exposure on the CH250 camera. Each final wavefront coded image was obtained by applying the inverse filter to a single intermediate image.

5.2 PSF and OTF results

The measured PSFs and derived OTFs for the focused and 4 µm defocused cases are shown in Figs. 5.4 and 5.5, comparing standard widefield microscopy with wavefront coding using a CPM. The widefield PSF shows dramatic change with defocus, as expected for a high aperture image of a 100 nm bead. But the wavefront coding PSF shows very little change after being defocused by the same amount.

The OTF measurements in Fig. 5.4(a) emphasise this focus independence for the wavefront coding system. While the in–focus OTF for the widefield system has the best overall response, the OTF quickly drops after defocusing. The widefield defocused OTF also appears to bounce at 1.1 cycles / µm, indicating a null below the spatial frequency cutoff. Such nulls make it impossible in widefield to use the most straightforward method of deconvolution — division of the image by the system OTF in Fourier space. Time consuming iterative solutions must be used instead.

The wavefront coding system OTF shows a reduced SNR compared with the in–focus widefield OTF. Yet the same SNR is maintained through a wide change in focus, indicating a depth of field at least 8 times higher than the widefield system. The CPM frequency response extends to 80% of the spatial frequency cutoff of the widefield case before descending into the noise floor. This indicates that the wavefront coding system has maintained much of the

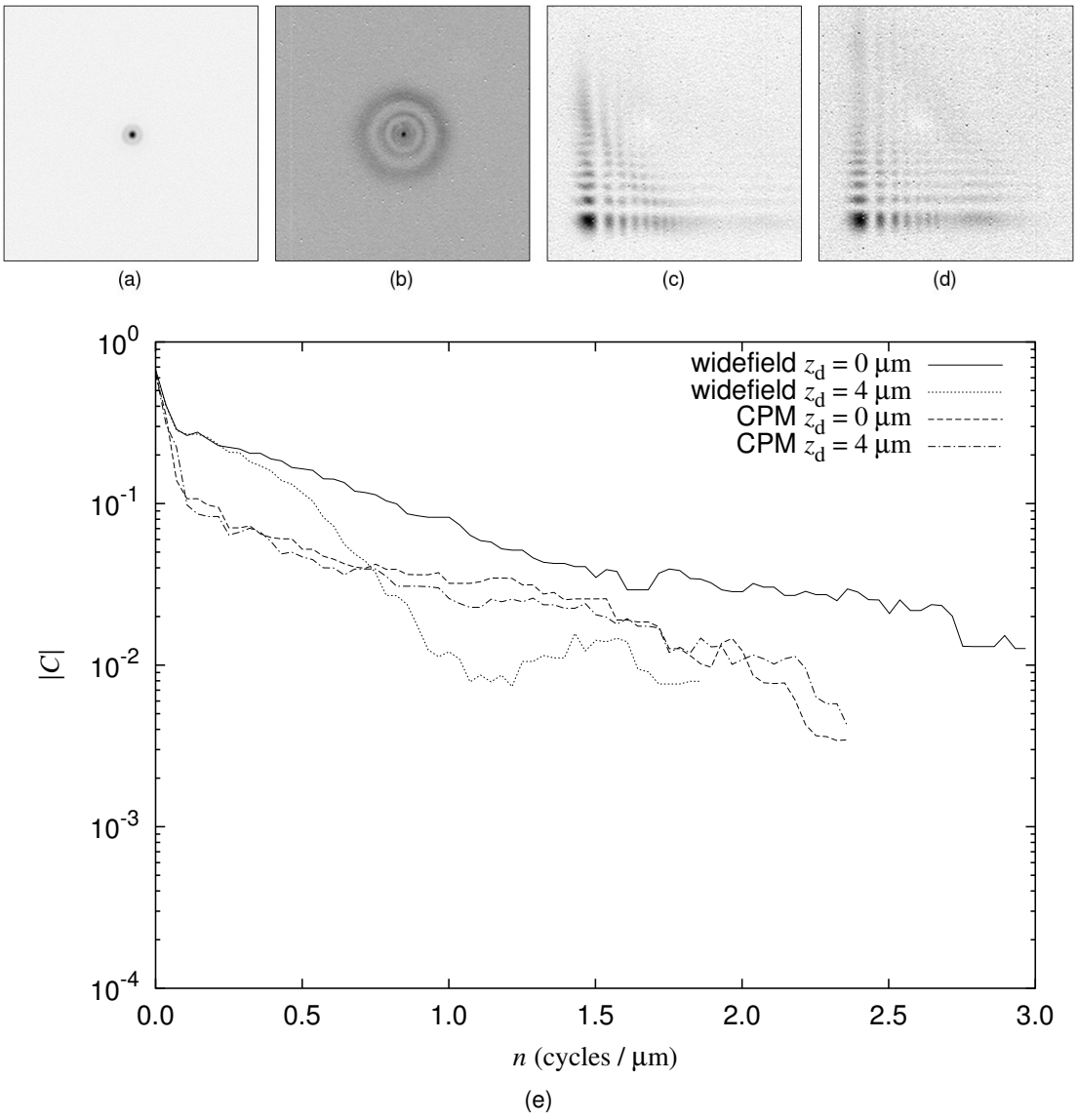

Figure 5.4: Experimental PSFs and OTFs for the widefield and wavefront coding systems as measured using a 100 nm fluorescent bead and a NA $= 1.3$ oil objective. For each type of microscope, a PSF from the plane of best focus is followed by one with 4 µm defocus. The upper images (a-d) show the intensity of a central region of the PSF whilst the lower graph (e) gives the magnitude of the OTF for a line $m = 0$ through the OTF for each case: (a) widefield $z_d = 0\,\mu$m, (b) widefield defocused $z_d = 4\,\mu$m, (c) CPM $z_d = 0\,\mu$m, (d) CPM defocused $z_d = 4\,\mu$m. The PSFs have area $13\,\mu\text{m} \times 13\,\mu\text{m}$ and can be compared with the simulations in Fig. 4.6. The raw OTF results were noisy right across the spectrum. For clarity they have been median filtered and truncated when the signal dropped below their respective noise floors.

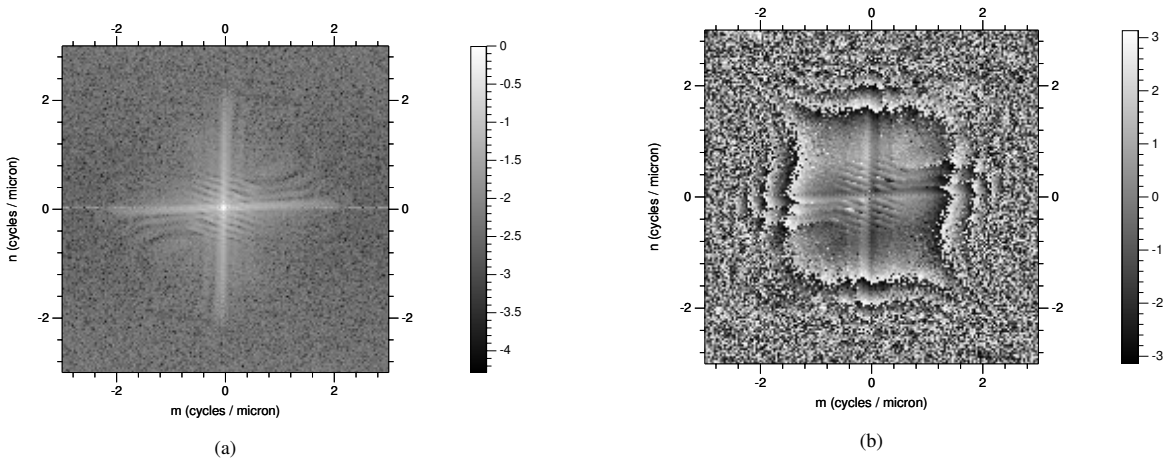

Figure 5.5: The measured CPM in–focus 2D OTF : (a) is the magnitude of the OTF in $\log_{10}$ scale, and (b) is the wrapped OTF phase in radians. This OTF was obtained from the Fourier transform of a 100 nm fluorescent bead PSF in Fig. 5.4. This figure can be compared with the simulation results in Fig. 4.7.

transverse resolution expected from the high aperture lens used. Because there are no nulls in the CPM OTF at spatial frequencies below the SNR imposed cutoff, deconvolution can be performed using a single–pass inverse filter based on the reciprocal of the system OTF.

A limiting factor on the SNR, and therefore the wavefront coding system resolution, is the CCD camera dynamic range of 16 bits, giving a noise floor of at least 1.5×10^{-5}. From Fig. 5.4(e) the effective noise floor seems to be dramatically higher at 10^{-2}. As discussed in section 5.1.1, background glare imposed a limit on the SNR for the fluorescent bead PSF. This reduction in SNR has a greater impact on the off–axis spatial frequencies, where a higher SNR is required to maintain high spatial frequency response, an effect which is clearly seen in the measured 2D OTF in Fig. 5.5.

Using the 1 µm pinhole, we were able to probe the axial behaviour of the CPM PSF. The measured PSF at $z_{\mathrm{d}} = -15\,\mu\mathrm{m}$ is compared with vectorial and paraxial theory in Fig. 5.6. Clearly the vectorial theory is correctly predicting high order structure in the defocused PSF which is missing from the paraxial simulation. However, the PSF is very dim at 15 µm, an axial distance which is well outside the working EDF range for the CPM used in these measurements.

PSF slices along the optical axis are shown in Fig. 5.7 for both widefield and CPM. These can be compared with the theoretical predictions shown in Figs. 4.8 and 4.9. While it is clear that we have under sampled the PSF, we have nevertheless obtained a good overview of the extended CPM PSF, which matches vectorial theory in the broad features of the visible struc-

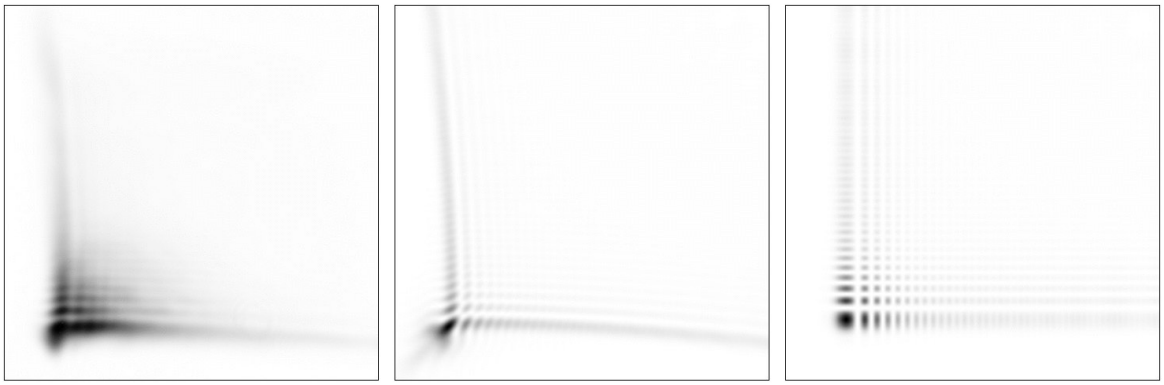

Figure 5.6: The effect of deep defocus on the CPM PSF. Shown for $z_d = -15\,\mu m$ are the 2D PSFs (a) measured with the $1\,\mu m$ pinhole, (b) simulated with vectorial theory, and (c) simulated with paraxial theory. The projected pupil integration code from chapter 4 was used to calculate the simulation images. The image width for each case is $21\,\mu m$.

ture, such as the banana shape and the approximate dimensions. To compare more closely with the fine detail of the simulated PSFs, finer z steps are needed, which could be provided by piezo driven objective mount. A smaller pinhole could also be used, for example holes in a 50 nm thin layer of evaporated gold can be as small as 5 nm in diameter (Brakenhoff et al., 1979), although any vectorial diffraction effects due to such a small aperture would have to be carefully considered (Roberts, 1987).

5.3 Biological imaging results

In order to experimentally test high resolution biological imaging using the CPM wavefront coding system in epi-fluorescence, we imaged an anti-tubulin / FITC–labelled HeLa cell. For comparison, we also imaged the same mitotic nucleus in both a standard widefield fluorescence microscope and a confocal laser scanning system (Fig. 5.8). The CPM and widefield images were recorded with our Photometrics CH250 camera.

The first widefield image, Fig. 5.8(a), shows a mitotic nucleus with one centriole in sharp focus, while a second centriole higher in the specimen is blurred. This feature became sharp when the focus was altered by $6\,\mu m$, as shown in Fig. 5.8(b). The wavefront coding system image in Fig. 5.8(c) shows a much greater depth of field, with both centrioles in focus in the same image. We observed a depth of field increase of at least 6 times compared with the widefield system, giving a lower bound of $6\,\mu m$ on the depth of field for the wavefront coding

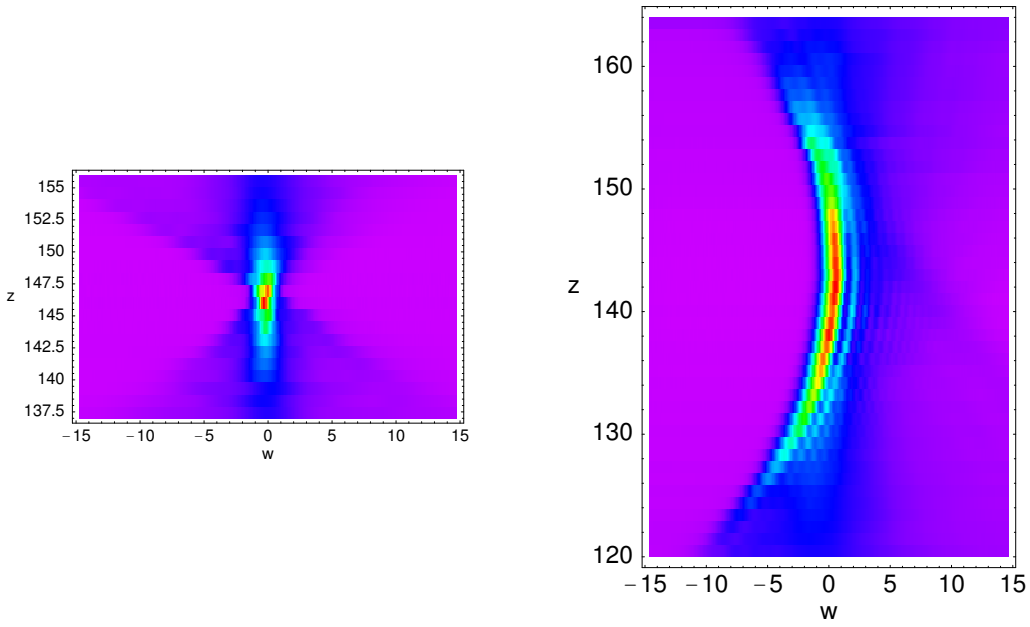

(a) (b)

Figure 5.7: Slices along the z axis through the (a) widefield PSF and (b) CPM PSF. The transverse co-ordinate w runs along the line $x = y$. The PSFs were measured using the 1 µm pinhole. These plots can be compared with the vectorial simulations in Fig. 4.8 and the paraxial CPM PSF simulation in Fig. 4.9. The measured CPM PSF has the clear banana shape as predicted. A slight clockwise rotation and general vertical asymmetry in the CPM PSF could indicate spherical aberration. However, the widefield PSF also displays some asymmetry. Coarse stepping is clearly visible, due to the 1 µm gap between transverse planes of the measured PSFs. The 1 µm pinhole width also limits the clarity of any fine structure in the PSFs, while giving a very strong signal which was crucial for imaging the extended structure of the CPM PSF. The w and z axis units are all in the same scale of µm. The z axis was taken from the microscope focus dial, and has an arbitrary offset between (a) and (b).

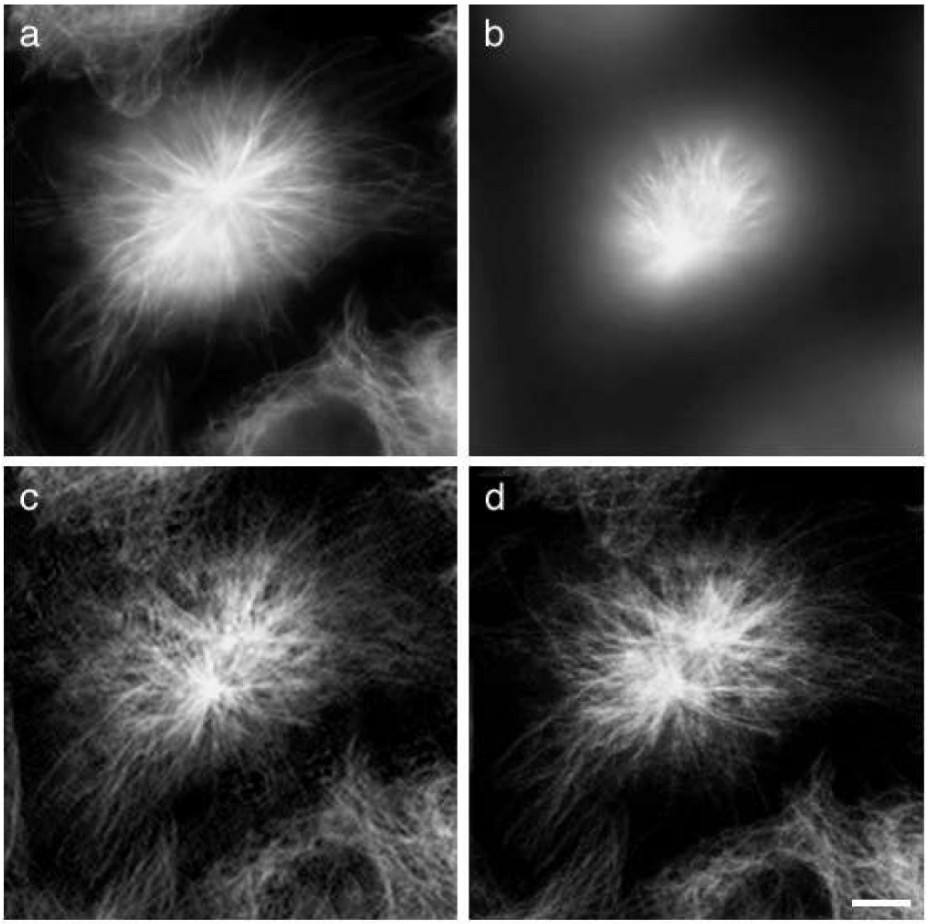

Figure 5.8: Comparison images of an anti-tubulin / FITC–labelled HeLa cell nucleus obtained using three kinds of microscope. (a-b) Conventional widefield fluorescence images of the same mitotic nucleus acquired at two different focal planes, 6 µm apart in depth. Misfocus blurring is prevalent, with only one of the two centrioles in focus in each image. (c) A CPM wavefront coding image of this nucleus greatly increases focal depth so that now both centrioles in the mitotic spindle are sharply focused. (d) An equivalent confocal fluorescence EDF image obtained by averaging 24 separate planes of focus, spaced 0.5 µm apart. The resolutions of the wavefront coding and confocal images are comparable but the confocal image took over 20 times longer to produce. Note that wavefront coding gives a perspective projection and confocal gives an isometric projection, which chiefly accounts for their slight difference in appearance. Objective NA=1.3 oil, scale bar: 6 µm.

system with an NA = 1.3 oil objective. This compares well with an 8 µm EDF working range predicted by the theory in chapter 4.

For further comparison, we imaged the same specimen using a confocal microscope. A simulated EDF image is shown in Fig. 5.8(d), obtained by averaging 24 planes of focus. This gives an image of similar quality to the wavefront coding image. However, the confocal system took over 20 times longer to acquire the data for this image, due to the need to scan the image point in all three dimensions. There is also a change in projection geometry between the two systems. The confocal EDF image has orthogonal projection, whereas the wavefront coding EDF image has perspective projection.

We used wavefront coding to image several other biological specimens with the NA = 1.3 oil objective in epi-fluorescence and brightfield. Specimens included cultured neurons and pollen grains. The results were similar to those shown above for the HeLa cells.

5.4 Conclusion

Wavefront coding is a new approach to microscopy. Instead of avoiding aberrations, we deliberately create and exploit them. The aperture of the imaging lens still places fundamental limits on performance. However wavefront coding allows us to trade off those limits between the different parameters we need for a given imaging task. Focal range, signal to noise, mechanical focus scanning speed and maximum frequency response are all negotiable using this hybrid digital–optical approach to microscopy.

The theoretical simulations in chapter 4 predict that the CPM focal region behaviour will be altered at high apertures, which will become more important with higher SNR imaging systems. For large values of defocus, these results predict a tighter limit on the focal range of EDF imaging than is the case for paraxial systems, as well as additional potential for image artefacts due to aberrations.

The high aperture experimental results point to the significant promise of wavefront coding. They clearly agree with the vectorial theory more closely than the paraxial theory. Although, as is generally the case in microscopy, many important features of focusing are still visible after taking the paraxial approximation.

The fundamental EDF behaviour remains in force at high apertures, as demonstrated by both experiment and theory. This gives a solid foundation to build on. The CPM was part of the first generation wavefront coding design. Using simulations, new phase mask designs can be tested for performance at high apertures before fabrication. With this knowledge,

further development of wavefront coding techniques may be carried out, enhancing its use at high apertures.

Part III

Phase measurement using DIC microscopy

Chapter 6

DIC theory and phase retrieval

Differential interference contrast (DIC) is a popular way to image unstained biological specimens. In this chapter I summarise relevant existing theory for DIC imaging, and review various methods for enhancing the phase imaging that DIC provides. This chapter forms the background to a new recipe for phase retrieval which is proposed in chapter 7.

6.1 Theory

A vectorial high aperture theory for DIC has not yet been presented. The most advanced theory published is by Preza et al. (1999). They proposed a partially coherent paraxial theory of DIC imaging for 3D objects using the Born approximation for isotropic weak phase objects and compared simulations against experimental measurements of manufactured phase objects. A detailed study of the transfer function for DIC was made by Cogswell and Sheppard (1992). A general overview of DIC imaging was presented in Pluta (1989).

We follow the coherent paraxial 2D model by Preza et al. (1999). The optical setup required for DIC imaging is shown in Fig. 6.1. Linearly polarised light is split by the first Wollaston prism into two orthogonally polarised beams with slightly different propagation directions. After focusing by the condenser lens, the two beams are separated at the focal plane by a shear distance $2\Delta x$. If there is a phase gradient in the specimen at the focal plane, then the two beams will acquire slightly different optical path lengths ϕ_{1x} and ϕ_{2x}. The beams are then collected by the objective lens, before being combined at a second Wollaston prism to produce a single linearly polarised beam, where the axis of polarisation carries information about the phase difference between the two beams at the focal plane. The analyser converts this into intensity so that the phase gradient $\Delta\phi_x = \phi_{1x} - \phi_{2x}$ is imaged.

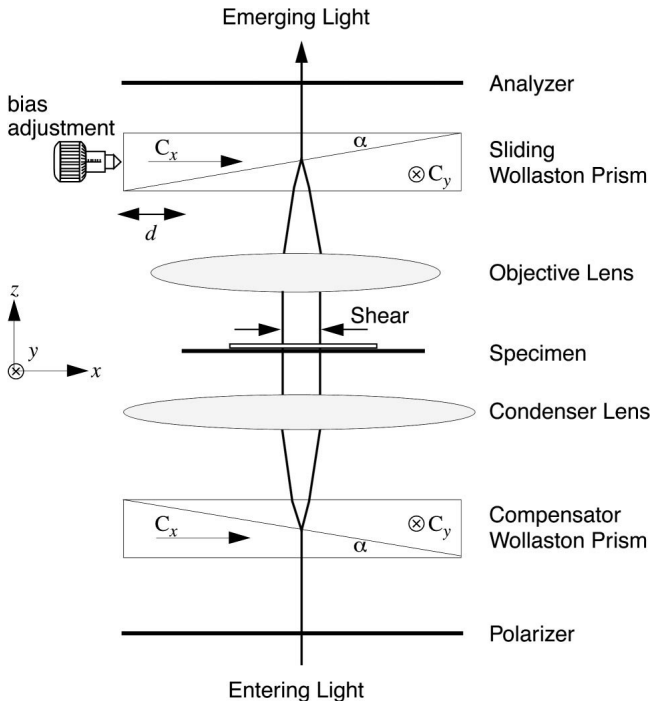

Figure 6.1: Diagram of the optical system for DIC imaging, reproduced from Preza et al. (1999).

Using geometrical optics and assuming a thin object with weak absorption and phase, we can write the DIC image intensity as

$$f_{2\theta}(x,y) = a_{1x}^2 + a_{2x}^2 + 2a_{1x}a_{2x}\cos[\phi_{1x} - \phi_{2x} + 2\theta] \,, \tag{6.1}$$

where $a_{1x}(x+\Delta x, y)$and $a_{2x}(x-\Delta x, y)$ are the amplitudes for two points in the object separated by a shear $2\Delta x$, and 2θ is the optical DIC bias which is commonly set by translating the second Wollaston prism (Pluta, 1989; Cogswell and Sheppard, 1992). An alternative method for changing the bias which is more convenient in some cases is known as the de Senarmont method, where a quarter waveplate is inserted before the analyser, allowing the bias to be changed by rotating the analyser (Hariharan, 1993). Some microscope manufacturers, such as Nikon, offer this method as part of their standard setup for DIC.

Note that Eq. (6.1) does not assume a constant object amplitude. The DIC image contains a mixture of information about the amplitude and phase of the specimen.

While the geometrical optics model of DIC is useful for describing this mixture of phase and amplitude imaging, in the next chapter we will simulate DIC for a NA $= 0.5$ objective, so we need a more accurate model for simulating phase retrieval methods. A significant

increase in realism is obtained by using a paraxial Fourier optics model, assuming a 2D weak phase object.

We begin by considering the brightfield PSF $E_{\mathrm{BF}}(x,y)$. We can determine E_{BF} using a paraxial version of the Fourier optics approach given in sections 4.2.2–4.2.4. The paraxial pupil was given in Eq. (4.18), which we set to unity for brightfield imaging

$$P_{\mathrm{BF}}(m,n) \approx \begin{cases} 1 & \text{if } m^2+n^2 < \sin^2\alpha \\ 0 & \text{elsewhere} \end{cases}, \tag{6.2}$$

where α is the aperture half-angle. We can then obtain the focal plane PSF using a 2D Fourier transform across the circular pupil

$$E_{\mathrm{BF}}(x,y) = \mathcal{F}\{P_{\mathrm{BF}}(m,n)\}\,. \tag{6.3}$$

This model is scalar in that we assume depolarisation during focusing is negligible due to the relatively low aperture.

The DIC PSF can then be written as the superposition of two laterally offset beams each with a different bias phase

$$E_{\mathrm{DIC}}(x,y) = \frac{1}{2}\left[\mathrm{e}^{-i\theta}E_{\mathrm{BF}}(x-\Delta x,y) - \mathrm{e}^{i\theta}E_{\mathrm{BF}}(x+\Delta x,y)\right]\,. \tag{6.4}$$

Using the Fourier shift theorem and Eq. (6.2), we can take the inverse Fourier transform of the PSF to arrive at a paraxial pupil function for DIC

$$P_{\mathrm{DIC}}(m,n) = \begin{cases} -2i\sin(\theta + k\Delta x m) & \text{if } m^2+n^2 < \sin^2\alpha \\ 0 & \text{elsewhere} \end{cases}. \tag{6.5}$$

In order to calculate a coherent image of the complex weak phase object

$$w(x,y) = a(x,y)\exp[i\phi(x,y)]\,, \tag{6.6}$$

we take the 2D Fourier transform to get the object spectrum $W(m,n)$ and then multiply with the pupil function, Fourier transform and take the intensity to get the image

$$I(x,y) = \left|\mathcal{F}\{P(m,n)W(m,n)\}\right|^2\,. \tag{6.7}$$

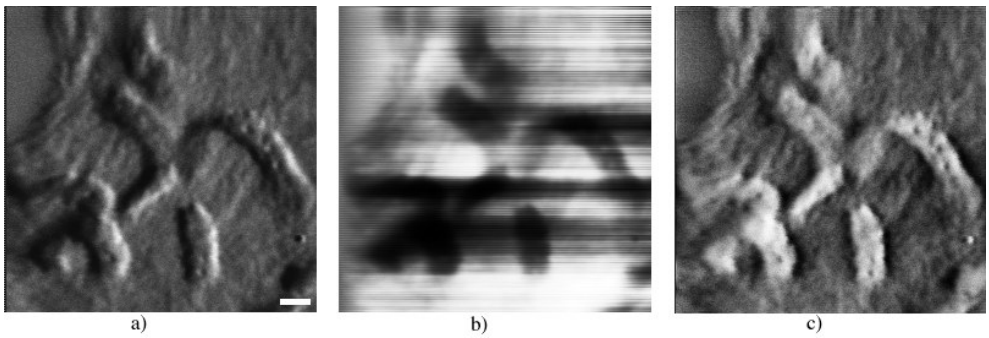

Figure 6.2: Image processing of DIC images. (a) A confocal transmission DIC image of metaphase chromosomes from an orchid root tip preparation showing the directional gradient shading which is characteristic of DIC. (b) The same image after line integration along the horizontal axis shows streaking due to the unknown constant of integration for each line. (c) The same image after applying a half–plane Hilbert transform demonstrates that the chromosome features now could be isolated from the background using simple thresholding. Scale bar = 2 µm. Reproduced from Arnison et al. (2000).

DIC microscopy is usually partially coherent both temporally (white light) and laterally (open condenser aperture). This requires additional convolution operations to model, as detailed by Preza et al. (1999). However, Preza et al. also noted that coherent imaging is reasonably accurate. Objects which are bandwidth limited to within the passband of the coherent transfer function will be imaged with a similar spatial frequency response for both coherent and partially coherent imaging. Coherent ringing effects are only encountered when the object spectrum exceeds the passband of the pupil.

6.2 Enhancement methods

DIC is popular for biological imaging because it can image many features without the need for staining. An example DIC image is shown in Fig. 6.2(a). DIC is often combined with other contrast methods, for example fluorescence may select for specific features while DIC gives an overview of the cell structure including the cell walls and nucleus. DIC is also often used in laser trapping experiments to track the motion of the trapped bead in relation to cell components (Cole et al., 1995). For these applications, generally no additional optical modifications or post-processing is required.

Nevertheless there are cases where DIC enhancement is desirable. Researchers may wish to concentrate on the phase information, for example to image very small objects such as

microtubules or as a quantitative measure of specimen properties (Inoué, 1989). Sometimes amplitude contrast from the specimen dominates the phase signal the researcher is interested in. Or researchers may want to visualise the specimen phase in 3D, which is difficult because of the differential nature of DIC imaging (Arnison et al., 2000). Being able to image the specimen phase in isolation from specimen amplitude contrast obviously offers the most flexibility for applications like these.

To summarise, four major problems persist in using DIC to image specimen phase:

1. standard DIC systems are qualitative in nature, with a non-linear response to optical path length gradients in the specimen;

2. the DIC output intensity is a mix of amplitude and phase gradient contrast;

3. for many applications it is useful to obtain the actual phase of the specimen, whereas DIC gives a directional phase gradient; and

4. it is desirable that any phase reconstruction method be straightforward, non-iterative and yet robust.

Several approaches to solving these problems have been proposed in recent years. Phase shifting DIC is a quantitative optical approach to isolating the phase gradient by shifting the DIC prism bias (Hariharan and Roy, 1996; Cogswell et al., 1997; Xu et al., 2001). While phase shifting DIC relies on a geometrical optics approximation of DIC imaging in order to isolate the phase, Ishiwata et al. (1996) demonstrated an alternative method for isolating the phase based on a partially coherent model. Their method involves multiplying the image intensity by the sin of the DIC prism bias, then integrating over the bias to isolate the phase.

Shimada et al. (1990) briefly outline a method which at first glance solves the main three problems of linearity, phase isolation and isotropic integration. They demonstrated phase retrieval from a series of DIC images with changing prism bias and shear direction. However, the details are not clearly specified for their phase shifting and phase integration steps. In addition, their method is designed for reflection DIC, and implicitly assumes a constant object amplitude.

Approaches involving iterative computation which also only partially solve the first three problems include line integration (Fig. 6.2(b)) preferably combined with deconvolution (Kam, 1998), variance filtering and directional integration using iterative energy minimisation (Feineigle et al., 1996), and rotational diversity (Preza, 2000). The latter technique involves taking several rotated DIC images and combining them using iterative deconvolution. Non-iterative

yet anisotropic methods include direct deconvolution (van Munster et al., 1997) and the half–plane Hilbert transform (Fig. 6.2(c) from Arnison et al. (2000)) which is a qualitative Fourier approach to integrating the phase gradient.

Chapter 7

Phase imaging using DIC and spiral phase

To date no author has outlined a full method which completely addresses all four DIC problems outlined in section 6.2. In this chapter we detail a combined optical and computational extension of DIC which solves these major problems, resulting in a phase image which is linearly proportional to the object phase and which has a laterally isotropic response to specimen phase. The method combines phase shifting, two directions of shear, and Fourier-space integration using a modified spiral phase transform. We simulated the method using a phantom object with spatially varying amplitude and phase. Simulated results show good agreement between the final phase image and the object phase.

7.1 Method

Our method combines four techniques. The first technique is conventional DIC microscopy, as described in section 6.1, which results in the 2D image intensity previously given in Eq. (6.1),

$$f_{2\theta}(x,y) = a_{1x}^2 + a_{2x}^2 + 2a_{1x}a_{2x}\cos[\phi_{1x} - \phi_{2x} + 2\theta] \,. \tag{7.1}$$

where $a_{1x}(x+\Delta x, y)$and $a_{2x}(x-\Delta x, y)$ are the amplitudes for two points in the object separated by a shear $2\Delta x$ set by the DIC Wollaston prism, $\Delta\phi_x = \phi_{1x} - \phi_{2x}$ is the corresponding phase difference between those two points, and 2θ is the optical DIC bias. Here we assume geometrical optics and the Born approximation, but we do not assume a constant object amplitude.

The second technique is phase shifting DIC (Hariharan and Roy, 1996; Cogswell et al., 1997; Xu et al., 2001). This technique retrieves a linear phase gradient through phase shifting by rotating the bias 2θ. The bias may be conveniently set by first inserting a quarter wave plate before the analyser. Rotating the analyser then rotates the bias (Hariharan, 1993). We can then obtain the phase gradient in the x direction using

$$\Delta\phi_x = \tan^{-1}\left(\frac{f_{\pi/2} - f_{3\pi/2}}{f_0 - f_\pi}\right) , \tag{7.2}$$

where four DIC images f have been recorded at biases of $2\theta = 0, \pi/2, \pi, 3\pi/2$. We have now removed both the object amplitude and vignetting from the signal and obtained a linear phase gradient in the x direction. This step also removes many potential phase-independent system errors, such as weak spots on the camera or non-uniform illumination. But we have so far only imaged the component of the phase gradient which is parallel with the shear direction (van Munster et al., 1998).

The third technique is to repeat the previous two steps with the shear rotated to obtain $\Delta\phi_y$. The shear direction may be changed by rotating either the specimen or the DIC prisms by 90°. We note that a recently announced variant of DIC called total interference microscopy (Carl Zeiss, Germany) is designed to allow easy rotation of the shear angle. Combinations of DIC with multiple shear directions and phase shifting have been published previously (Hartman et al., 1980; Preza et al., 1998; Preza, 2000; Shimada et al., 1990). However in those papers a simpler phase shifting technique was applied which assumed a constant object amplitude.

Using the Fourier shift theorem, we can write down the Fourier transforms of our phase gradients

$$\Delta\phi_x(x,y) \iff 2\mathrm{i}\sin(2\pi\Delta x m)\Phi(m,n) \tag{7.3}$$

$$\Delta\phi_y(x,y) \iff 2\mathrm{i}\sin(2\pi\Delta y n)\Phi(m,n) , \tag{7.4}$$

where m, n are the spatial frequency co-ordinates, $\mathrm{i} = \sqrt{-1}$, $\iff$ denotes a 2D Fourier transform, and capitalisation denotes a Fourier transformed function.

This sets the stage for the fourth technique: using Eqs. (7.3) and (7.4) to obtain the phase $\phi(x,y)$. We apply a Fourier-space integration approach which is direct, straightforward, and

reasonably accurate for images that do not contain discontinuities, such as biological phase images. We begin by combining the x and y phase gradients to form a complex function,

$$g(x,y) = \Delta\phi_x + \mathrm{i}\Delta\phi_y \,. \tag{7.5}$$

We then perform a 2D Fourier transform on $g(x,y)$ and apply the Fourier shift theorem to give

$$\Phi(m,n) = \begin{cases} 0 & \text{if } [\sin(2\pi\Delta x m), \sin(2\pi\Delta x n)] = [0,0] \\ G(m,n)/H(m,n) & \text{otherwise} \end{cases} \tag{7.6}$$

with

$$H(m,n) = 2i\,[\sin(2\pi\Delta x m) + \mathrm{i}\sin(2\pi\Delta x n)] \tag{7.7}$$

where we have assumed $\Delta x = \Delta y$. An inverse Fourier transform of $\Phi(m,n)$ gives the desired phase $\phi(x,y)$. Phase unwrapping presents a similar problem which can be solved using a range of direct and iterative methods (Ghiglia and Pritt, 1998; Volkov et al., 2002).

For small shear distances Δx we can use $\sin x \approx x$ to approximate Eq. (7.7) with

$$H_{\mathrm{d}}(m,n) = 4\pi\mathrm{i}\Delta x(m + \mathrm{i}n) \,. \tag{7.8}$$

This is equivalent to approximating the phase gradients $\Delta\phi_x$ and $\Delta\phi_y$ with the partial derivatives $\partial\phi/\partial x$ and $\partial\phi/\partial y$, and then applying the Fourier derivative theorem.

Summarising the algorithm steps we have:

1. DIC imaging giving f,
2. phase shifting giving $\Delta\phi_x$,
3. shear rotation giving $\Delta\phi_y$, and
4. Fourier phase integration giving the desired phase ϕ.

7.2 Simulation results

We have carried out simulations to evaluate the full method. We used a coherent paraxial imaging model as described in section 6.1, which has been shown to give reasonably accurate predictions for DIC (Preza et al., 1999). However, extending our model for this simulation

to include partial coherence and vectorial diffraction should not pose any fundamental difficulties.

The phantom object we simulated is shown in Fig. 7.1(a-b), with a transmission amplitude varying from 80% to 100% and a phase varying from 0 waves to 0.3 waves. The illuminating beam was monochromatic with wavelength $\lambda = 550\,\text{nm}$, imaging the sample through a 0.5 NA lens. The shear of the DIC Wollaston prism was set at $2\Delta x = 1\,\mu\text{m}$.

DIC imaging was modelled using fast Fourier transforms (FFT) with 1024×1024 pixels including windowing and padding, with the subsequent image being 363×363 pixels corresponding to a $25\,\mu\text{m}$ square region of the object. DIC was simulated using the pupil functions

$$P_x(m,n) = -2\text{i}\sin(\theta + k\Delta x m) \tag{7.9}$$

$$P_y(m,n) = -2\text{i}\sin(\theta + k\Delta x n)\,, \tag{7.10}$$

for shear in the x and y directions respectively, where $k = 2\pi/\lambda$. An example pupil function used in the model is shown in Fig. 7.2. We added 10% random noise to the intensity of each simulated DIC image, an example of which is shown in Fig. 7.1(c). Note the image contains a mixture of amplitude and phase information, with the amplitude information geometrically distorted due to the asymmetrical pupil function in Eq. (7.9). We used this DIC imaging model to simulate and compute steps 2 and 3 of the algorithm. The phase gradient in the x direction $\Delta\phi_x$ is shown in Fig. 7.1(d).

The final step, Eqs. (7.6) and (7.7), was carried out using 726×726 FFTs, after mirror reflecting the phase gradient image to significantly reduce edge discontinuity effects, as described by Ghiglia and Pritt (1998, pp. 191-192). The mirror reflection was implemented by creating a larger image g_r with four reflected copies of $g(x,y)$ inside it

$$g_\text{r} = \begin{bmatrix} g(x,y) & g(-x,y) \\ g(x,-y) & g(-x,-y) \end{bmatrix}\,, \tag{7.11}$$

before applying a Fourier transform to get $G(m,n)$. We also windowed $H(m,n)$ to avoid amplifying high frequency noise in the image, by setting $H(m,n) = 0$ for spatial frequencies outside the aperture of the simulated imaging system. Fig. 7.3 shows the spiral transform derived from the Fourier shift theorem H compared with the derivative approximation H_d. Steps 1-3 took 54 s to execute on an AMD Athlon 1.4 GHz PC, while performing step 4 took 4 s.

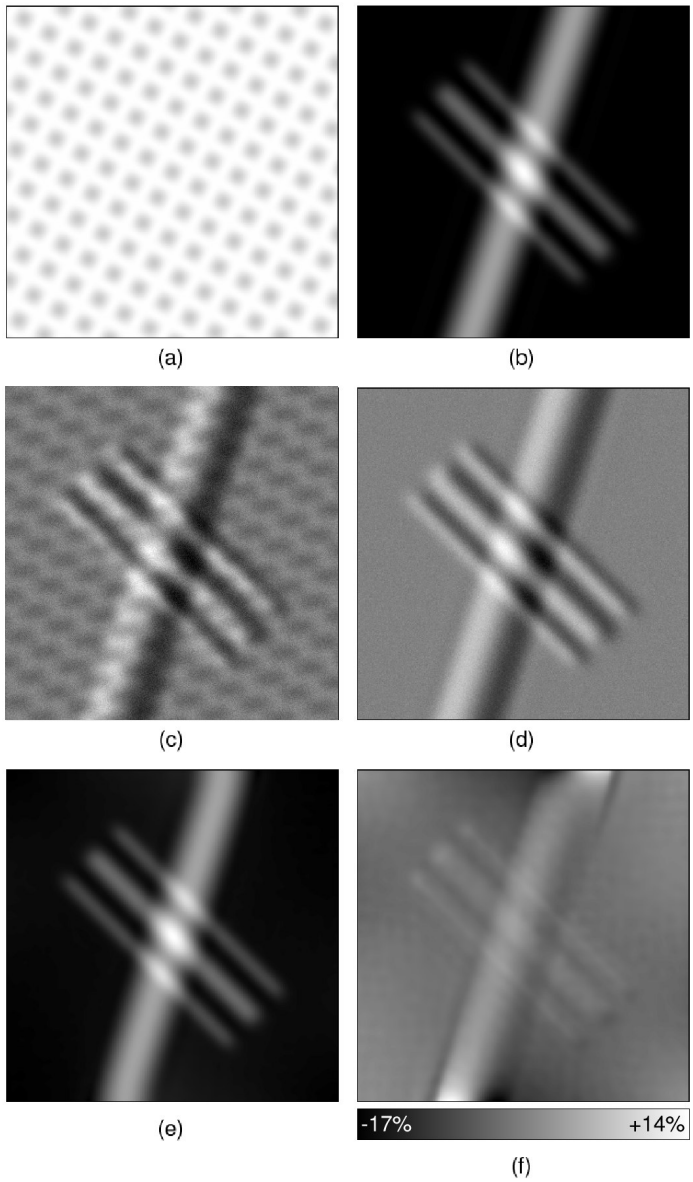

Figure 7.1: Linear phase imaging simulation results. (a) Object transmission amplitude. (b) Object phase. (c) Simulated DIC image with shear in the x (horizontal) direction, bias $2\theta = 3\pi/2$ and artificial imaging noise at 10% of the signal. (d) Phase shifted DIC image $\Delta\phi_x$. This step isolates the phase gradient from the DIC image. (e) Final retrieved phase from our algorithm. The object amplitude, noise and directional phase shading have all been removed by our algorithm, leaving an image which is a close match to the object phase shown in (b). (f) Phase error between the normalised object phase and the normalised retrieved phase. Note the only large errors are where the phase object meets the upper and lower edges of the image. The width of the field of view is $25\,\mu$m.

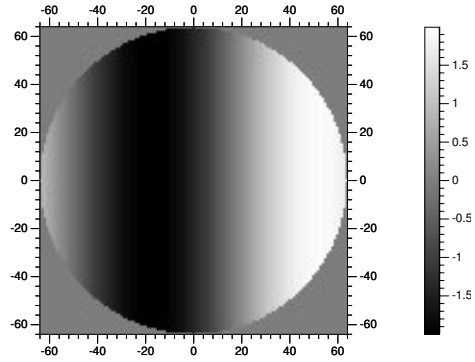

Figure 7.2: Imaginary part of the simulated DIC pupil for shear in the x (horizontal) direction, bias $2\theta = 3\pi/2$. The real part is zero throughout. The axis units are pixels within discrete Fourier space.

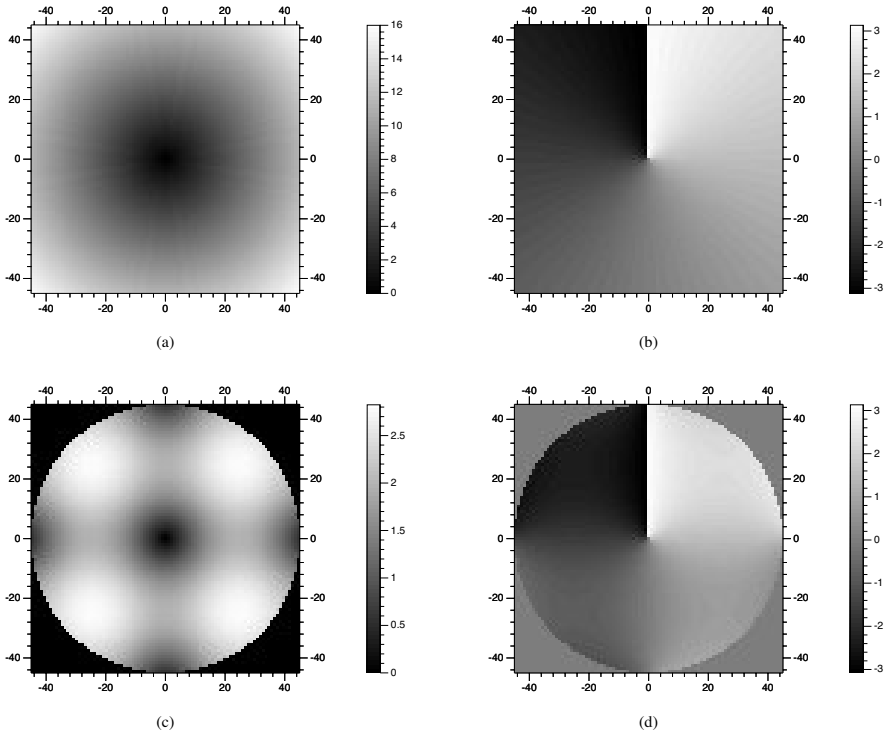

Figure 7.3: Modified spiral phase transforms. (a) Magnitude and (b) phase of the derivative approximation H_{d} of Eq. (7.8). (c) Magnitude and (d) phase of H of Eq. (7.7) after we applied an aperture window to avoid boosting the noise.

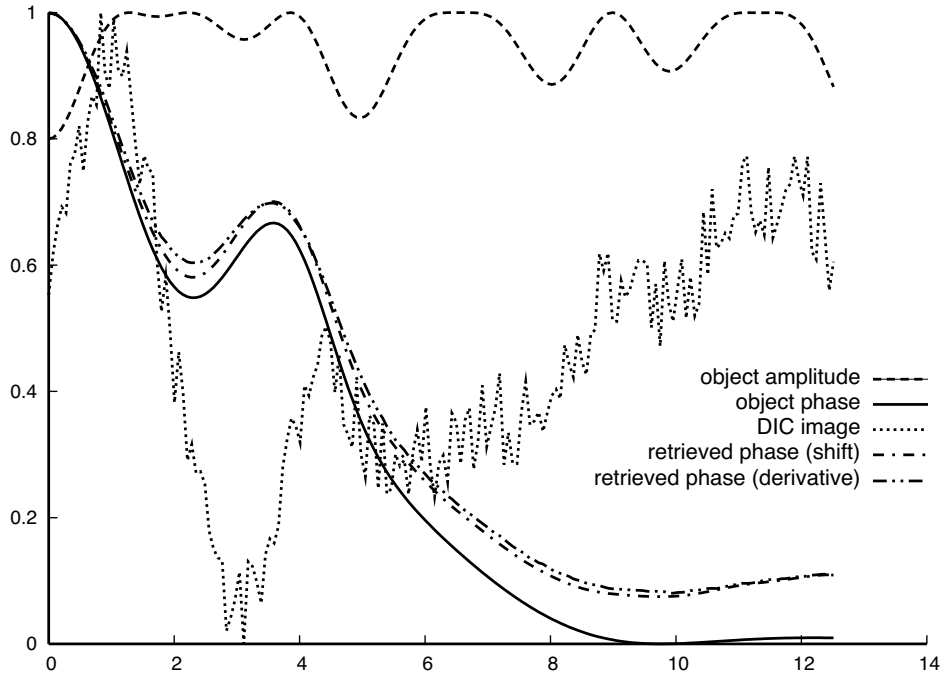

Figure 7.4: A one dimensional line plot through Fig. 7.1, vertically downwards from the image centre. Shown are the object amplitude, object phase, DIC image with shear in the x direction and the final phase images from our shift algorithm using H from Eq. (7.8) and the derivative algorithm using H_{d} from Eq. (7.7). The latter three values have been normalised to enable comparison. The horizontal axis is in microns and the vertical axis is in normalised units. The retrieved phase has been effectively isolated from the object amplitude and signal noise. The error due to Fourier edge artefacts increases as the plot moves away from the centre of the image.

Figure 7.5: Retrieved phase when the mirror reflection step was omitted from the shift algorithm.

The final phase image ϕ generated using H from Eq. (7.7) is shown in Fig. 7.1(e). This image shows we have extracted only the phase from the phantom object, with no visible corruption by either the object amplitude or random noise. After normalising both the object phase and the retrieved phase, a normalised image of the error (Fig. 7.1(f)) and a line plot (Fig. 7.4) show good agreement between the shift algorithm retrieved phase image and the phase of the object, with a maximum error of 17% at the edge of the image. The mean squared error is 1.5×10^{-3}.

Using the shift algorithm instead of the derivative algorithm made a relatively small difference, as seen in Fig. 7.4, with the derivative method having a mean squared error of 1.8×10^{-3} and a peak error of 18%. However, the results from both algorithms were significantly worse if the mirror reflection step of Eq. (7.11) was left out, as illustrated in Fig. 7.5.

7.3 Discussion

The retrieved phase image is qualitatively excellent. However, certain errors persist, mostly at the top and bottom edges of the image. The error in those regions is caused by the intersection of the object with the image boundary. These Fourier edge artefacts might be avoided when acquiring images experimentally by placing the spatially varying parts of the object entirely within the field of view. However, avoiding such object clipping is not always possible, which is why we have deliberately placed parts of our simulated object across the image boundary. The edge artefacts could also be removed during processing by using an

improved phase integration technique at the cost of increased complexity and computation (Ghiglia and Pritt, 1998). We note that our method does not produce streaking artefacts of the sort shown in Fig. 6.2(b), in contrast with the real-space line integration techniques described by Kam (1998) and Shimada et al. (1990).

For simplicity in explaining our algorithm, Eqs. (7.1) and (7.2) assume geometrical optics. However, our imaging simulation included diffraction, which will attenuate high spatial frequencies in the phase gradient and thereby introduce additional error in the retrieved phase. Yet despite our simulated object phase having a broad spatial frequency spectrum, the Fourier edge artefacts noted above produced larger errors than the geometrical optics basis of our algorithm. Supplementing our method with iterative deconvolution would produce more accurate results, effectively adding the ability to deal with spatially varying amplitudes to the approach by Preza (2000).

Careful consideration of sampling is required to maintain high accuracy. We are assuming that the phase gradient $\Delta\phi_x$ is not too large. Unless

$$\Delta\phi_x < \pi \tag{7.12}$$

the DIC phase signal will wrap around. An additional limit is imposed by diffraction (Sprague and Thompson, 1972)

$$\frac{\Delta\phi_x}{2\Delta x} < k \sin\alpha \,. \tag{7.13}$$

For the system we have simulated, Eq. (7.12) is a tighter constraint on $\Delta\phi_x$ than Eq. (7.13). The size of the diffraction spot provides a tighter limit on $\Delta\phi_x$ than the shear distance only if the shear distance $2\Delta x$ is less than half the width of the brightfield PSF, where the PSF width is defined by Sprague and Thompson (1972) to be $\lambda/\sin\alpha$. Vignetting will also affect the signal for large phase gradients.

An alternative for linear phase imaging is quantitative phase microscopy (Barty et al., 1998). This method obtains the axial intensity derivative using defocus and converts it to separate amplitude and phase images using the transport of intensity equation (TIE). One important difference to our technique is that the TIE image contrast for fine phase details decreases with higher condenser apertures (Barone-Nugent et al., 2002; Sheppard, 2002), whereas DIC imaging gives the best contrast and resolution at the largest condenser apertures.

It is interesting to note that the phase integration method in Eqs. (7.5–7.7) is related to the Hilbert transform, especially when expressed in the approximate form in Eq. (7.8). H_{d} may be rewritten as

$$H_{\mathrm{d}}(m,n) = 4\pi \mathrm{i} \Delta x \sqrt{m^2+n^2} \exp\left[\mathrm{i} \arctan(n/m)\right] \ . \tag{7.14}$$

Applying the spiral phase term $\exp\left[\mathrm{i} \arctan(n/m)\right]$ in Fourier space has been proposed as a 2D version of the Hilbert transform, which is traditionally defined in 1D only (Larkin et al., 2001). It is also known as a complex Riesz transform. This 2D Hilbert transform is isotropic, as compared with the anisotropic 2D half–plane Hilbert transform outlined by Arnison et al. (2000). While both the modified spiral phase transform in Eq. (7.14) and the 2D Hilbert transform proposed by Larkin et al. are isotropic, our modified spiral differs by virtue of the amplitude weighting, present in Eq. (7.14) as the square root term.

A similar phase integration solution may be obtained using vectors instead of complex numbers in Eq. (7.5), as detailed in appendix A.

In conclusion, we have detailed an extension of DIC which enables isotropic linear phase imaging using phase shifting, two directions of shear, and non-iterative Fourier phase integration incorporating a modified spiral phase transform. Simulated results show good agreement between the final phase image and the object phase, for a 2D phantom object with spatially varying amplitude and phase. The method can in principle be used with any DIC imaging system, with potential applications including biological microscopy, 3D visualisation, surface profiling, refractive index profiling, and x-ray microscopy (David et al., 2002; Kaulich et al., 2002).

Part IV

Conclusion

Chapter 8

Conclusion

This thesis has explored several key developments in modern microscopy.

1. The digital and optical components of the microscope are becoming increasingly intertwined.
2. 3D Fourier optics is gaining ground as a powerful tool for modelling high aperture focusing.
3. Accurate modelling of aberrations in high aperture imaging systems poses interesting challenges, whether those aberrations are deliberate or otherwise.
4. There is renewed interest in phase, including controlling the phase of the pupil and measuring the phase of the specimen.

I have described both theoretical and experimental techniques which are in the process of stretching their wings into the hybrid digital–optical domain. These techniques were then applied as appropriate for two examples of hybrid microscopy with promising potential for biomedical imaging: controlling the pupil phase using a cubic phase mask (CPM) to produce the desired imaging behaviour, and measuring the specimen phase using differential interference contrast (DIC) microscopy. I have demonstrated that 3D Fourier optics is a useful conceptual model for designing, simulating, and measuring the performance of modern high resolution microscopes.

8.1 Summary of results

Hybrid microscopy changes the way we look at performance. Chapter 3 presented a generalisation of 3D optical transfer function (OTF) theory which can assess the spatial frequencies

produced by focusing designs with arbitrary pupil functions. I used this theory to completely map the 3D spatial frequencies of the intensity in the focal region for linearly polarised illumination, results which had not been presented previously despite the 80 year history of vectorial focusing theory.

But arbitrary pupil designs may fundamentally change the nature of focusing, which means we need to adapt our focal region measurement techniques. In chapter 5 I documented experiments which measured at high resolution the greatly extended point spread functions (PSFs) which are produced by wavefront coding microscopes.

This extended PSF in turn makes new demands on theoretical calculations in the focal region. Chapter 4 outlined the theoretical and numerical tools necessary to chart the increased territory using vectorial diffraction, and applied them to modelling wavefront coding microscopy with a rectangular cubic phase function as the pupil.

Part II described high aperture imaging using a CPM, a first generation wavefront coding pupil designed to enable extended depth of focus (EDF) imaging. This approach hinges on the creation of suitable conditions for reliable post-processing, side–stepping the apparently degraded images produced by the optical part of the hybrid microscope. The paraxial behaviour of focusing with a CPM at low apertures was well known, but EDF behaviour is desirable for many high aperture microscope applications. This thesis compared the paraxial and vectorial theory for calculating the CPM PSF, finding significant differences in behaviour. My high aperture PSF measurements verified many details of the vectorial theory predictions. The most significant theoretical result was a reduction in the EDF working range compared with a paraxial estimate.

We applied the CPM to high aperture fluorescence imaging of biological specimens, and found we were able to produce EDF images at the cost of some dynamic range. I presented images of a HeLa cell taken with a 1.3 NA lens and a CPM strength of 25.8 waves, indicating a minimum $6\times$ increase in the depth of field. The vectorial theory showed that only minor degradation in the spatial frequencies in the PSF are expected over a focal range which is $8\times$ that of a widefield system.

Switching from controlling the phase to measuring it, part III described a new recipe for making linear measurements of the specimen phase using the popular DIC microscopy mode. This recipe involved separating the phase gradient from the specimen amplitude using phase shifting, and then computationally combining the phase gradient measured in two orthogonal directions using a modified spiral phase transform applied in Fourier space.

I presented a simulation of this spiral phase method being applied to a phantom object. Qualitatively the phase images produced clearly matched the phase of the simulated object,

with reasonably low errors appearing in the quantitative analysis. Fourier processing played a crucial role in the conception of this phase retrieval method, which relies on complementary optical and digital extensions of DIC microscopy.

8.2 Future directions

Throughout this thesis I have suggested many areas which I feel would be interesting for future exploration. In this section I summarise those suggestions, along with additional ideas for future research which would build on the themes of this thesis.

The vectorial transfer function theory I presented covers only the monochromatic incoherent case. The effect of reduced temporal coherence in broadband light and short pulses on the vectorial transfer function could be modelled using a finite pupil thickness instead of an infinitely thin spherical shell. Lateral partial coherence could also be introduced by a suitable 3D generalisation of accepted 2D partially coherent transfer function theory.

Since even 2D lateral partially coherent calculations add an additional 2 dimensions to 2D diffraction integrals, it may be a little while yet before computers are powerful enough for a full 3D exploration of the partially coherent frequency spectrum of vectorial focusing. But brightfield and DIC microscopes are usually operated with a wide condenser aperture, providing the motivation for ongoing extension of partially coherent imaging theory.

In particular, 2D partially coherent simulations for wavefront coding have yet to be presented, even though partial coherence is often present in such systems. Our simulation of spiral phase retrieval could also benefit from extension to partial coherence, as well as extension to 3D to explore its behaviour for imaging the phase of objects which are not flat. These aspects of DIC have been simulated before, however what has not yet been done is a vectorial high aperture model of DIC. Although this could be over the top in simulating the spiral phase retrieval method, which after all was based partly on geometrical optics, a full vectorial model of DIC would certainly be interesting in its own right.

In section 3.4 I mentioned the constraints on using the vectorial OTF for measuring the performance of a complete microscope, as opposed to the spectral content of the intensity in the focal region. A key question is whether a complete microscope model can be built up as a series of pupil functions and Fourier operations.

Rohrbach and Stelzer (2002b) have gone a long way in compiling a set of vectorial pupil functions which accurately embody aberrations, dipole radiation patterns, and multiple scattering. Such developments could follow in the footsteps of the paraxial success of 2D Fourier optics by enabling a full 3D vectorial impulse response and transfer function theory, which

seems likely to enable simpler modelling of existing high aperture systems, together with providing the symbolic tools to design new hybrid microscopes.

Evaluation of the projected pupil function integral I described in chapter 4 using fast Fourier transforms provided the speed we needed to explore the extended focal region produced by the CPM. There are several ways this technique could be extended which would be very helpful for modelling wavefront coding, as well as vectorial focusing in general.

Larkin (1999) has outlined a method for projecting the pupil along a transverse axis before Fourier transforming to find the PSF, which would be particularly useful for plotting axial slices through both spherically aberrated and CPM PSFs. This would also involve using pupil function formulations of refractive index change theory, as described by Török et al. (1995), Rohrbach and Stelzer (2002b) and Schönle and Hell (2002).

The enlarged PSF that the CPM provides could also be the basis for an interesting test of the limits of the Debye approximation for microscope objectives. CPM PSF calculations using the Huygens–Fresnel integral could be compared with the Debye–Wolf integral results presented in this thesis to see if the Debye approximation imposes a significant accuracy penalty at practical distances from the Gaussian focal point.

The vectorial results in this thesis are limited to modelling the field in the focal region of a single lens. A more complete model of wavefront coding at high apertures would include both condenser and collection objectives, dipole effects, and integration over polarisation angle for unpolarised illumination. A practical aid for CPM optical alignment would be models of the CPM PSF for lateral and rotational misalignment of the CPM relative to the limiting square aperture. In addition, the effects of propagation of the CPM over the distance to the true back focal plane of the lens could be important to explore.

This additional theory will need experimental verification. Obvious improvements to the PSF measurement techniques presented in this thesis would include measuring at finer focal steps using a piezo objective positioner, and using finer holes as point sources. Juškaitis (2003) and Rhodes et al. (2002) outline methods for even finer PSF measurement, including determination of the PSF phase.

High aperture optics could feed back into wavefront coding in important ways. For the biological wavefront coding results presented in this thesis, restoration was performed using an inverse filter designed using the simulated paraxial widefield OTF and the vectorial measured CPM OTF. Instead of the paraxial simulation, the vectorial simulated widefield OTF should be used. An additional option would be to use the simulated vectorial CPM OTF to see if it improves the filter performance.

Phase derivatives can be obtained using simple amplitude pupil masks based on the Fourier derivative theorem (Sprague and Thompson, 1972; Lancis et al., 1997; Szoplik et al., 1998; Furuhashi et al., 2003), but these investigations restricted their attention to pure phase objects. Modern spatial light modulators (SLMs) are capable of dynamic high resolution filtering of both the amplitude and phase of an incident field. Using SLMs in the pupil plane, the DIC pupil model in Eq. (6.5) could be implemented as an optical Fourier filter. This would allow easy adjustment of the shear distance, shear direction and bias. It would be a powerful way to explore DIC, as well as an efficient apparatus for implementing our proposed spiral phase retrieval method.

Of course, our spiral phase algorithm was presented in this thesis using simulations only. I look forward to experimental tests using standard DIC optics which determine whether the spiral phase algorithm lives up to its promise.

Part V

Appendices

Appendix A

Fourier solution of the inverse gradient

We start with the 2D vector relation

$$\nabla\phi = \frac{\partial\phi}{\partial x}\mathbf{i} + \frac{\partial\phi}{\partial y}\mathbf{j}\,, \tag{A.1}$$

where ϕ is the phase we want to retrieve, $\Delta\phi_x = \partial\phi/\partial x$ and $\Delta\phi_y = \partial\phi/\partial y$ are the linear phase gradients we get from phase shifting DIC, and $\mathbf{i}$ and $\mathbf{j}$ are the unit vectors pointing along the x and y axes respectively. Now the definition of ∇^2 is

$$\nabla^2 g = \nabla\cdot\nabla g\,, \tag{A.2}$$

so, as suggested by Colin Sheppard, we can write

$$\nabla^2\phi = \nabla\cdot(\Delta\phi_x\mathbf{i} + \Delta\phi_y\mathbf{j})\,. \tag{A.3}$$

Rearranging gives

$$\phi = \nabla^{-2}\left[\nabla\cdot(\Delta\phi_x\mathbf{i} + \Delta\phi_y\mathbf{j})\right]\,. \tag{A.4}$$

Note the Fourier relations (Bracewell, 1978; Sheppard, 1999)

$$\nabla\cdot\mathbf{g} \Longleftrightarrow \mathbf{r}\cdot\mathbf{G} \tag{A.5}$$

$$\nabla^{-2}\psi \Longleftrightarrow \frac{1}{r^2}\Psi\,, \tag{A.6}$$

where $\mathbf{r}$ is the polar co-ordinate vector in Fourier space. Applying these we can solve Eq. (A.4) via Fourier space using

$$\phi = \mathcal{F}^{-1}\left[\frac{1}{r^2}\mathbf{r}\cdot\mathcal{F}\left(\Delta\phi_x\mathbf{i}+\Delta\phi_y\mathbf{j}\right)\right] . \tag{A.7}$$

This is similar to the Fourier solution of the inverse Laplacian used by the transport of intensity phase retrieval method (Paganin and Nugent, 1998) as detailed by Volkov et al. (2002).

I then simplified Eq. (A.7) to

$$\phi = \mathcal{F}^{-1}\left\{\frac{1}{r}\left[\cos\theta\mathcal{F}\left(\Delta\phi_x\right)+\sin\theta\mathcal{F}\left(\Delta\phi_y\right)\right]\right\} . \tag{A.8}$$

The complex version using

$$g = \Delta\phi_x + i\Delta\phi_y , \tag{A.9}$$

which is used as Eq. (7.5) in chapter 7, was contributed by Kieran Larkin as an equivalent calculation which provides a computational shortcut. It means we only have to do two Fourier transforms instead of three. It is also an interesting example of using a complex number to represent a 2D vector. Servin et al. (2003) in their discussion of an n-dimensional quadrature transform, argue that numerical cross talk can create problems when using complex numbers to represent a pair of 2D vectors in this way.

Appendix B

Code

In this appendix I describe the details of the computer code used for optical calculations in this thesis.

Vectorial optical transfer function (chapter 3)

I calculated the vectorial optical transfer function using numerical integration in a Mathematica notebook called `otf.nb`. The axial projections were verified against Sheppard and Larkin (1997). Three-dimensional isosurface plots were created with OpenDX.

A free copy of this code can be obtained by contacting me at `mra@physics.usyd.edu.au`.

Projected pupil integration (chapters 4, 5 & 7)

I developed a MATLAB script called `votf.m`. This was executed in either MATLAB itself, or a free software clone of MATLAB called octave.

`votf.m` was used to calculate the projected pupil, transverse slices through the point spread function, and the projected optical transfer function. It could model these using a vectorial Debye–Wolf model, a scalar model, or the paraxial approximation. I applied it to modelling widefield microscopy, microscopy with the cubic phase mask, and for simulating paraxial DIC.

The projected pupil was sampled in Cartesian co-ordinates, and 2D fast Fourier transforms were used to perform integrations. I verified it in the following ways:

- Intensity PSF results matched Boivin and Wolf (1965) Fig. 2 (which shows a transverse plane through the PSF with (a) focused and (b) defocused $u = 6$ where u is a normalised axial co-ordinate) with at least 5% accuracy;

- OTF results matched Born and Wolf (1999) Fig. 9.13 (which shows defocused OTFs) with at least 5% accuracy;
- I checked the pupil phase gradient was not wrapping ($|\nabla\phi| < \pi$, based on the Nyquist criterion) for CPM calculations with $N = 2048$; and
- I checked it converged stably for the CPM and defocus cases investigated. Results using $N = 2048, 4096, 6144$ matched to within 1%.

A free copy of this code can be obtained by contacting me at `mra@physics.usyd.edu.au`.

Refractive index change integration (chapter 4)

A Mathematica notebook called `interface.nb` was used to plot the results of a C++ program called `cpmiface.cc`. The two programs communicated using mathlink. `cpmiface.cc` used Gauss–Legendre sampling of the pupil (Press et al., 1993) in calculating a 2D spherical polar integral. Original Mathematica, mathlink and C++ code was kindly provided by Peter Török. I modified the C++ code to add the cubic phase mask.

This code was used to calculate *wz* sections of the widefield, CPM and spherically aberrated PSF. It was verified in the following ways:

- The widefield PSF was verified to 1% accuracy against Stamnes (1986) Fig. 16.7, which shows 1D transverse plots though the IPSF for $u = 0$, a range of aperture angles α and along (a) the x axis and (b) the y axis; and
- The spherically aberrated PSF was verified to 5% accuracy against Sheppard and Török (1997a) Fig. 3, which shows axial lines through the IPSF for $d = 0, 20, 40, 100\mu$m.

Convergence was an issue for the CPM PSF with a square pupil. Even with 2000^2 samples of the pupil, for observation points 10µm from the axis the result fluctuated by up to 2% when small changes were made to the number of samples. With the CPM being a rectangular function across a square aperture, it is more likely to produce aliasing errors when sampled using a polar function.

The 2D density plots which were calculated using this code, in Fig. 4.8, have a linear scale, and are normalised to the peak intensity over a large $40 \times 30\,\mu$m slice through the PSF. Using $N = 400$ samples was found to give sufficient accuracy under these conditions.

For the CPM, `votf.m` and `cpmiface.cc` agreed qualitatively but not quantitatively. The quantitative discrepancy was in the range 1%–10%, and was most visible as a difference

in the axial scaling of *wz* slices through the PSF. Both codes are based on the Debye–Wolf integral and its accompanying approximations.

I am not sure what the cause of the discrepancy is, but I suspect it is due to differences in CPM and defocus scaling. The large pupil phase strengths introduced by the CPM and its long focal depth place unusually high demands on the accuracy of any integration code. These accuracy issues have been taken into account in the observations and discussions based on the results from these codes. Statements are generally qualitative in nature, based on much larger differences in the results than the size of these numerical discrepancies.

Bibliography

Agard, D. A. and Sedat, J. W. (1983) "Three-dimensional architecture of a polytene nucleus," *Nature*, **302**, 676–681.

Allen, R. D., Allen, N. S., and Travis, J. L. (1981) "Video-enhanced contrast, differential interference contrast (AVEC-DIC) microscopy: a new method capable of analyzing microtubule-related motility in the reticulopodial network of Allogromia laticollaris," *Cell Motil.*, **1**(3), 291–302.

Amos, W. B., Reichelt, S., Cattermole, D. M., and Laufer, J. (2003) "Re-evaluation of differential phase contrast (DPC) in a scanning laser microscope using a split detector as an alternative to differential interference contrast (DIC) optics," *J. Microsc.*, **210**(2), 166–175.

Arfken, G. B. and Weber, H. J. (1995) *Mathematical methods for physicists*, Academic Press, 4th ed.

Arnison, M. R., Cogswell, C. J., Sheppard, C. J. R., and Török, P. (2003) "Wavefront coding fluorescence microscopy using high aperture lenses," in P. Török and F.-J. Kao (Eds.), *Optical imaging and microscopy: techniques and advanced systems*, vol. 87 of *Springer series in optical sciences*, chap. 6, pp. 143–165, Springer-Verlag, Berlin.

Arnison, M. R., Cogswell, C. J., Smith, N. I., Fekete, P. W., and Larkin, K. G. (2000) "Using the Hilbert transform for 3D visualisation of differential interference constrast microscope images," *J. Microsc.*, **199**(1), 79–84.

Arnison, M. R., Larkin, K. G., Sheppard, C. J. R., Smith, N. I., and Cogswell, C. J. (2004) "Linear phase imaging using differential interference contrast microscopy," *J. Microsc.*, **214**(1), 7–12.

Arnison, M. R. and Sheppard, C. J. R. (2002) "A 3D vectorial optical transfer function suitable for arbitrary pupil functions," *Opt. Commun.*, **211**(1-6), 53–63.

Bahlmann, K. and Hell, S. W. (2000) "Electric field depolarization in high aperture focusing with emphasis on annular apertures," *J. Microsc.*, **200**(1), 59–67.

Bailey, B., Farkas, D. L., Taylor, D. L., and Lanni, F. (1993) "Enhancement of axial resolution in fluorescence microscopy by standing wave excitation," *Nature*, **366**, 44–48.

Bajer, A. S. and Molè-Bajer, J. (1956) "Ciné-micrographic studies on mitosis in endosperm. II. Chromosome, cytoplasm and Brownian movements," *Chromosoma*, **7**, 558–607.

Barone-Nugent, E., Barty, A., and Nugent, K. (2002) "Quantitative phase-amplitude microscopy I: optical microscopy," *J. Microsc.*, **206**(3), 194–203.

Barty, A., Nugent, K. A., Paganin, D., and Roberts, A. (1998) "Quantitative optical phase microscopy," *Opt. Lett.*, **23**(11), 817–819.

Berek, M. (1927) "Grundlagen der Tiefenwahrnehmung im Mikroskop," *Marburg Sitzungs Ber.*, **62**, 189–223.

Boivin, A. and Wolf, E. (1965) "Electromagnetic field in the neighborhood of the focus of a coherent beam," *Phys. Rev.*, **138**(6B), 1561–1565.

Booth, M. J., Neil, M. A. A., Juškaitis, R., and Wilson, T. (2002) "Adaptive aberration correction in a confocal microscope," *Proc. Natl. Acad. Sci. USA*, **99**(9), 5788–5792.

Born, M. and Wolf, E. (1999) *Principles of optics*, Cambridge University Press, Cambridge, U. K., 7th ed.

Bracewell, R. N. (1978) *The Fourier transform and its applications*, McGraw-Hill, New York, 2nd ed.

Bracewell, R. N. (1995) *Two-dimensional imaging*, Prentice Hall, Englewood Cliffs, NJ, USA.

Bradburn, S., Cathey, W. T., and Dowski, E. R., Jr. (1997) "Realizations of focus invariance in optical-digital systems with wave-front coding," *App. Opt.*, **36**(35), 9157–9166.

Bradburn, S. C. (1998) *Experimental procedures for obtaining extended-depth-of-focus images using hybrid optical/digital systems*, Master's thesis, University of Colorado.

Brakenhoff, G. J., Blom, P., and Barends, P. (1979) "Confocal scanning light microscopy with high aperture immersion lenses," *J. Microsc.*, **117**(2), 219–232.

Brenner, K., Lohmann, A., and Ojeda-Castañeda, J. O. (1983) "The ambiguity function as a polar display of the OFT," *Opt. Commun.*, **44**, 323–326.

Campos, J., Escalera, J. C., Sheppard, C. J. R., and Yzuel, M. J. (2000) "Axially invariant pupil filters," *J. Mod. Optics*, **47**(1), 57–68.

Carlsson, K., Danielsson, P. E., Lenz, R., Liljeaborg, A., Majlöf, L., and Åslund, N. (1985) "Three-dimensional microscopy using a confocal laser scanning microscope," *Opt. Lett.*, **10**, 53–55.

Castleman, K. R. (1979) *Digital image processing*, Prentice-Hall.

Cathey, W. T. and Dowski, E. R. (2002) "New paradigm for imaging systems," *Appl. Opt.*, **41**(29), 6080–6092.

Cathey, W. T. and Dowski, E. R., Jr. (1998) "Extended depth of field optical systems," US Patent 5,748,371.

Cathey, W. T., Frieden, B. R., Rhodes, W. T., and Rushforth, C. K. (1984) "Image gathering and processing for enhanced resolution," *J. Opt. Soc. Am. A*, **1**(3), 241–250.

Chi, W. and George, N. (2001) "Electronic imaging using a logarithmic asphere," *Opt. Lett.*, **26**(12), 875–877.

Cogswell, C. J. and Sheppard, C. J. R. (1992) "Confocal differential interference contrast (DIC) microscopy: including a theoretical analysis of conventional and confocal DIC imaging," *J. Microsc.*, **165**(1), 81–101.

Cogswell, C. J., Smith, N. I., Larkin, K. G., and Hariharan, P. (1997) "Quantitative DIC microscopy using a geometric phase shifter," in *Proc. SPIE*, vol. 2984, pp. 72–81, San Jose, CA, USA.

Cole, R. W., Khodjakov, A., Wright, W. H., and Rieder, C. L. (1995) "A differential interference contrast-based light microscopic system for laser microsurgery and optical trapping of selected chromosomes during mitosis in vivo," *J. Microsc. Soc. Amer.*, **1**, 203–215.

Cox, I. J. and Sheppard, C. J. R. (1983a) "Digital image processing of confocal images," *Image and Vision Computing*, **1**(1), 52–56.

Cox, I. J. and Sheppard, C. J. R. (1983b) "Scanning optical microscope incorporating a digital framestore and microcomputer," *Applied Optics*, **22**, 1474–1478.

David, C., Nöhammer, B., Solak, H. H., and Ziegler, E. (2002) "Differential x-ray phase contrast imaging using a shearing interferometer," *Appl. Phys. Let.*, **81**(17), 3287–3289.

Debye, P. (1909) "Das Verhalten von Lichtwellen in der Nähe eines Brennpunktes oder einer Brennlinie," *Ann. Phys.*, **30**(4), 755–776.

Dowski, E. R., Jr. and Cathey, W. T. (1995) "Extended depth of field through wave-front coding," *Appl. Opt.*, **34**(11), 1859–1866.

Dowski, E. R., Jr. and Cogswell, C. J. (2003) "Wavefront coding phase contrast imaging systems," US Patent 6,525,302.

Egner, A. and Hell, S. W. (1999) "Equivalence of the Huygens-Fresnel and Debye approach for the calculation of high aperture point-spread functions in the presence of refractive index mismatch," *J. Microsc.*, **193**(3), 244–256.

Egner, A., Schrader, M., and Hell, S. (1998) "Refractive index mismatch induced intensity and phase variations in fluorescence confocal, multiphoton and 4Pi-microscopy," *Opt. Commun.*, **153**(4-6), 211–217.

Elkind, D., Zalevsky, Z., Levy, U., and Mendlovic, D. (2003) "Optical transfer function shaping and depth of focus by using a phase only filter," *Appl. Opt.*, **42**(11), 1925–1931.

Ewald, P. P. (1916) *An.. Physik*, **49**(1), 117.

Feineigle, P. A., Witkin, A. P., and Stonick, V. L. (1996) "Processing of 3D DIC microscopy images for data visualisation," in *Proc. IEEE International conference on acoustics, speech, and signal processing*, vol. 4, pp. 2160–2163, IEEE, New York.

Frieden, B. R. (1967) "Optical transfer of the three-dimensional object," *J. Opt. Soc. Am.*, **57**, 56–66.

Furuhashi, H., Matsuda, K., and Grover, C. P. (2003) "Visualization of phase objects by use of a differentiation filter," *Appl. Opt.*, **42**(2), 218–226.

Gan, X., Sheppard, C. J. R., and Gu, M. (1997) "Effects of Fresnel diffraction on confocal imaging with an annular lens," *Bioimaging*, **5**, 153–158.

Ghiglia, D. C. and Pritt, M. D. (1998) *Two-dimensional phase unwrapping : theory, algorithms, and software*, Wiley, New York, USA.

Gibson, S. F. and Lanni, F. (1989) "Diffraction by a circular aperture as a model for three-dimensional optical microscopy," *J. Opt. Soc. Am. A*, **6**(9), 1357–1367.

Gibson, S. F. and Lanni, F. (1991) "Experimental test of an analytical model of aberration in an oil-immersion objective lens used in three-dimensional light microscopy," *J. Opt. Soc. Am. A*, **8**(10), 1601–1613.

Goodman, J. (1968) *Introduction to Fourier optics*, McGraw-Hill, San Francisco, 1st ed.

Gu, M. (2000) *Advanced optical imaging theory*, Springer.

Gu, M. and Sheppard, C. J. R. (1992) "Three-dimensional coherent transfer function in reflection-mode confocal microscopy using annular lenses," *J. Mod. Opt.*, **39**, 783–793.

Gustafsson, M. G. L. (1999) "Extended resolution fluorescence microscopy," *Current Opinion in Structural Biology*, **9**, 627–634.

Gustafsson, M. G. L., Agard, D. A., and Sedat, J. W. (1999) "I5M: 3D widefield light microscopy with better than 100 nm axial resolution," *J. Microsc.*, **195**(1), 10–16.

Hamilton, D. K. and Sheppard, C. J. R. (1984) "Differential phase contrast in scanning optical microscopy," *J. Microsc.*, **133**, 27–39.

Hamilton, D. K., Wilson, T., and Sheppard, C. J. R. (1981) "Experimental observations of the depth-discrimination properties of scanning microscopes," *Opt. Lett.*, **6**, 625–626.

Hanser, B. M., Gustafsson, M. G. L., Agard, D. A., and Sedat, J. W. (2001) "Phase retrieval of widefield microscopy point spread functions," *Proc. SPIE*, **4261**, 60–68.

Hanser, B. M., Gustafsson, M. G. L., Agard, D. A., and Sedat, J. W. (2002) "Application of phase retrieved pupil functions in wide-field fluorescence microscopy," *Proc. SPIE*, **4621**, 40–46.

Hanser, B. M., Gustafsson, M. G. L., Agard, D. A., and Sedat, J. W. (2003) "Phase retrieval for high-numerical-aperture optical systems," *Opt. Lett.*, **28**(10), 801–803.

Hariharan, P. (1993) "The Sénarmont compensator: an early application of the geometric phase," *J. Mod. Opt.*, **4**, 2061–2064.

Hariharan, P. and Roy, M. (1996) "Achromatic phase-shifting for two-wavelength phase-stepping interferometry," *Opt. Commun.*, **126**(4-6), 220–222.

Hartman, J. S., Gordon, R. L., and Lessor, D. L. (1980) "Quantitative surface topography determination by Nomarski reflection microscopy. II. Microscope modification, calibration, and planar sample experiments," *Appl. Opt.*, **19**(17), 2998–3009.

Häusler, G. (1972) "A method to increase the depth of focus by two step image processing," *Opt. Commun.*, **6**(1), 38–42.

Häusler, G. and Korner, E. (1984) "Simple focusing criterion," *Appl. Opt.*, **23**, 2468–2469.

Heintzmann, R., Hanley, Q. S., Arndt-Jovin, D., and Jovin, T. M. (2001) "A dual path programmable array microscope (PAM): simultaneous acquisition of conjugate and non-conjugate images," *J. Microsc.*, **204**(2), 119.

Hell, S. W., Schrader, M., and Voort, H. T. M. v. d. (1997) "Far-field fluorescence microscopy with three-dimensional resolution in the 100-nm range," *J. Microsc.*, **187**(1), 1–7.

Higdon, P. D., Török, P., and Wilson, T. (1999) "Imaging properties of high aperture multiphoton fluorescence scanning optical microscopes," *J. Microsc.*, **193**(2), 127–141.

Holmes, T. J., Bhattacharyya, S., Cooper, J. A., Hanzel, D., Krishnamurthi, V., Lin, W.-C., Roysam, B., Szarowski, D. H., and Turner, J. N. (1995) "Light microscopic images reconstructed by maximum likelihood deconvolution," in J. B. Pawley (Ed.), *Handbook of biological confocal microscopy*, chap. 24, Plenum Press, New York, 2nd ed.

Holmes, T. J., Liu, Y.-H., Khosla, D., and Agard, D. A. (1991) "Increased depth of field and stereo pairs of fluorescence micrographs via inverse filtering and maximum-likelihood estimation," *Journal of Microscopy*, **164**, 217–237.

Hopkins, H. H. (1943) "The Airy disc formula for systems of high relative aperture," *Proc. Phys. Soc.*, **55**, 116.

Huse, N., Schönle, A., and Hell, S. W. (2001) "Z-polarized confocal microscopy," *J. Biomed. Opt.*, **6**(4), 480–484.

Ignatowsky, V. S. (1919) "Diffraction by a lens of arbitrary aperture," *Trans. Opt. Inst. Petrograd*, **1, paper 4**, 1–36.

Ignatowsky, V. S. (1920) "The relationship between geometrical and wave optics and diffraction of homocentral beams," *Trans. Opt. Inst. Petrograd*, **1, paper 3**, 1–30.

Inoué, S. (1981) "Video image processing greatly enhances contrast, quality, and speed in polarization-based microscopy," *J. Cell Biol.*, **89**(2), 346–356.

Inoué, S. (1989) "Imaging of unresolved objects, superresolution, and precision of distance measurement with video microscopy," *Methods Cell Biol.*, **30**, 85–112.

Inoué, S. (1995) "Foundations of confocal scanned imaging in light microscopy," in J. B. Pawley (Ed.), *Handbook of biological confocal microscopy*, chap. 1, pp. 1–17, Plenum Press, New York, 2nd ed.

Inoué, S. (2003) "Exploring living cells and molecular dynamics with polarized light microscopy," in P. Török and F.-J. Kao (Eds.), *Optical imaging and microscopy: techniques and advanced systems*, vol. 87 of *Springer series in optical sciences*, chap. 1, pp. 3–20, Springer-Verlag, Berlin.

Inoué, S. and Oldenbourg, R. (1998) "Microtubule dynamics in mitotic spindle displayed by polarized light microscopy," *Mol. Biol. Cell*, **9**(7), 1603–1607.

Inoué, S., Shimomura, O., Goda, M., Shribak, M., and Tran, P. T. (2002) "Fluorescence polarization of green fluorescence protein," *Proc. Nat. Acad. Sci. USA*, **99**(7), 4272–4277.

Ishiwata, H., Itoh, M., and Yatagai, T. (1996) "Retardation modulated differential interference microscope and its application to 3-D shape measurement," *Proc. SPIE*, **2873**, 21–24.

Jackson, J. D. (1962) *Classical electrodynamics*, John Wiley & Sons, New York.

Jacquet, M., Renault, G., Lallet, S., De Mey, J., and Goldbeter, A. (2003) "Oscillatory nucleocytoplasmic shuttling of the general stress response transcriptional activators Msn2 and Msn4 in Saccharomyces cerevisiae," *J. Cell Biol.*, p. 200303030.

James, R. W. (1965) *The optical principles of the diffraction of X-rays*, vol. II of *Crystalline state*, Cornell University Press, Ithaca, NY, USA.

Jarvis, R. A. (1974) "Computer controlled scanning optical microscope," *Microscope*, **22**, 247–258.

Juškaitis, R. (2003) "Characterizing high numerical aperture microscope objective lenses," in P. Török and F.-J. Kao (Eds.), *Optical imaging and microscopy: techniques and advanced systems*, vol. 87 of *Springer series in optical sciences*, chap. 2, pp. 21–43, Springer-Verlag, Berlin.

Juškaitis, R., Neil, M. A. A., Massoumian, F., and Wilson, T. (2001) "Strategies for wide-field extended focus microscopy," in *Focus on microscopy conference*, Amsterdam.

Juškaitis, R. and Wilson, T. (1998) "The measurement of the amplitude point spread function of microscope objective lenses," *J. Microsc.*, **189**(1), 8–11.

Kam, Z. (1998) "Microscopic differential interference contrast image processing by line integration (LID) and deconvolution," *Bioimaging*, **6**, 166–176.

Kam, Z., Hanser, B., Gustafsson, M. G. L., Agard, D. A., and Sedat, J. W. (2001) "Computational adaptive optics for live three-dimensional biological imaging," *Proc. Natl. Acad. Sci. USA*, **98**(7), 3790–3795.

Kaulich, B., Wilhein, T., Di Fabrizio, E., Romanato, F., Altissimo, M., Cabrini, S., Fayard, B., and Susini, J. (2002) "Differential interference contrast x-ray microscopy with twin zone plates," *J. Opt. Soc. Am. A*, **19**(4), 797–806.

Lancis, J., Szoplik, T., Tajahuerce, E., Climent, V., and Fernández-Alonso, M. (1997) "Fractional derivative Fourier plane filter for phase-change visualization," *Appl. Opt.*, **36**(29), 7461–7464.

Larkin, K. G. (1999) "PSF calculation by pupil projection along the m axis and subsequent 2D Fourier transformation," Personal communication.

Larkin, K. G., Bone, D. J., and Oldfield, M. A. (2001) "Natural demodulation of two-dimensional fringe patterns. I. General background of the spiral phase quadrature transform," *J. Opt. Soc. Am. A*, **18**(8), 1862–1870.

Mansuripur, M. (1986) "Distribution of light at and near the focus of high-numerical-aperture objectives," *J. Opt. Soc. Am. A*, **3**(12), 2086–2093.

Mansuripur, M. (1989) "Certain computation aspects of vector diffraction problems," *J. Opt. Soc. Am. A*, **6**(5), 786–805.

Mansuripur, M. (1993) "Distribution of light at and near the focus of high-numerical-aperture objectives: erratum," *J. Opt. Soc. Am. A*, **10**(2), 382–383.

McCutchen, C. W. (1964) "Generalized aperture and the three-dimensional diffraction image," *J. Opt. Soc. Am.*, **54**, 240–244.

Mertz, L. (1965) *Transformations in optics*, Wiley, New York.

Mezouari, S. and Harvey, A. R. (2003) "Phase pupil functions for reduction of defocus and spherical aberrations," *Opt. Lett.*, **28**(10), 771–773.

Minsky, M. (1961) "Microscopy apparatus," U.S. Patent No. 3,013,467.

Minsky, M. (1988) "Memoir on inventing the confocal scanning microscope," *Scanning*, **10**, 128–138.

Nieto-Vesperinas, M. (1991) *Scattering and diffraction in physical optics*, Wiley, New York.

Nye, J. F. (1999) *Natural focusing and fine structure of light : caustics and wave dislocations*, Institute of Physics Pub., Philadelphia, PA.

Ojeda-Castañeda, J., Ramos, R., and Noyola-Isgleas, A. (1988) "High focal depth by apodization and digital restoration," *Appl. Opt.*, **27**, 2583–2586.

Ojeda-Castañeda, J., Tepichin, E., and Diaz, A. (1989) "Arbitrarily high focal depth with a quasioptimum real and positive transmittance apodizer," *Appl. Opt.*, **28**(13), 2666–2670.

Oldenbourg, R. and Török, P. (2000) "Point-spread functions of a polarizing microscope equipped with high-numerical-aperture lenses," *Appl. Opt.*, **39**(34), 6325–6331.

Paganin, D. and Nugent, K. A. (1998) "Noninterferometric phase imaging with partially coherent light," *Phys. Rev. Lett.*, **80**, 2586–2589.

Pluta, M. (1989) *Advanced Light Microscopy: Specialised Methods*, vol. 2, Elsevier, Amsterdam.

Potuluri, P., Fetterman, M., and Brady, D. (2001) "High depth of field microscopic imaging using an interferometric camera," *Opt. Express*, **8**(11), 624.

Press, W., Teukolsky, S., Vetterling, W., and Flannery, B. (1993) *Numerical Recipes in C: The Art of Scientific Computing*, Cambridge University Press, Cambridge, UK, 2nd ed.

Preza, C. (2000) "Rotational-diversity phase estimation from differential-interference-contrast microscopy images," *J. Opt. Soc. Am. A*, **17**(3), 415–424.

Preza, C., Snyder, D. L., and Conchello, J.-A. (1999) "Theoretical development and experimental evaluation of imaging models for differential-interference-contrast microscopy," *J. Opt. Soc. Am. A*, **16**(9), 2185–2199.

Preza, C., van Munster, E. B., Aten, J. A., Snyder, D. L., and Rosenberger, F. U. (1998) "Determination of direction-independent optical path-length distribution of cells using rotational-diversity transmitted-light differential interference contrast (DIC) images," in *Three-dimensional and multidimensional microscopy: image acquisition and processing V*, vol. 3261, pp. 60–70, International Society for Optical Engineering (SPIE), San Jose, California, USA.

Rhodes, S. K., Nugent, K. A., and Roberts, A. (2002) "Precision measurement of the electromagnetic fields in the focal region of a high-numerical-aperture lens using a tapered fiber probe," *J. Opt. Soc. Am. A*, **19**(8), 1689–1693.

Richards, B. and Wolf, E. (1959) "Electromagnetic diffraction in optical systems II. Structure of the image field in aplanatic systems," *Proc. Roy. Soc. A*, **253**, 358–379.

Roberts, A. (1987) "Electromagnetic theory of diffraction by a circular aperture in a thick, perfectly conducting screen," *J. Opt. Soc. Am. A*, **4**(10), 1970–1984.

Rohrbach, A. and Stelzer, E. H. K. (2001) "Optical trapping of dielectric particles in arbitrary fields," *J. Opt. Soc. Am. A*, **18**(4), 839–853.

Rohrbach, A. and Stelzer, E. H. K. (2002a) "Three-dimensional position detection of optically trapped dielectric particles," *J. Appl. Phys.*, **91**(8), 5474–5488.

Rohrbach, A. and Stelzer, E. H. K. (2002b) "Trapping forces, force constants, and potential depths for dielectric spheres in the presence of spherical aberrations," *Appl. Opt.*, **41**(13), 2494–2507.

Salmon, E. D. and Tran, P. (1998) "High-resolution video-enhanced differential interference contrast (VE-DIC) light microscopy," *Methods Cell Biol.*, **56**, 153–184.

Schechner, Y. Y. and Kiryati, N. (2000) "Depth from defocus vs. stereo: How different really are they?" *Int. J. Comput. Vision*, **39**(2), 141–162.

Schechner, Y. Y., Kiryati, N., and Basri, R. (2000) "Separation of transparent layers using focus," *Int. J. Comput. Vision*, **39**(1), 25–39.

Schönle, A. and Hell, S. W. (2002) "Calculation of vectorial three-dimensional transfer functions in large-angle focusing systems," *J. Opt. Soc. Am. A*, **19**(10), 2121–2126.

Schrader, M. and Hell, S. (1996) "Wavefronts in the focus of a light microscope," *J. Microsc.*, **184**(3), 143–148.

Servin, M., Quiroga, J. A., and Marroquin, J. L. (2003) "General n-dimensional quadrature transform and its application to interferogram demodulation," *J. Opt. Soc. Am. A*, **20**(5), 925–934.

Shaw, P. J. (1995) "Comparison of wide-field/deconvolution and confocal microscopy for 3D imaging," in J. B. Pawley (Ed.), *Handbook of biological confocal microscopy*, chap. 23, Plenum Press, New York, 2nd ed.

Sheppard, C. J. R. (1988) "Depth of field in optical microscopy," *J. Microsc.*, **149**, 73–75.

Sheppard, C. J. R. (1997) "Aberrations in high aperture optical systems," *Optik*, **105**(1), 29–33.

Sheppard, C. J. R. (1999) "Vectors and Fourier transforms in optics," *Optik*, **110**(3), 157–160.

Sheppard, C. J. R. (2002) "Three-dimensional phase imaging with the intensity transport equation," *Appl. Opt.*, **41**(28), 5951–5955.

Sheppard, C. J. R. and Cogswell, C. J. (1990) "Three-dimensional imaging in confocal microscopy," in T. Wilson (Ed.), *Confocal Microscopy*, pp. 143–169, Academic Press, London, UK.

Sheppard, C. J. R., Gu, M., Kawata, Y., and Kawata, S. (1994) "Three-dimensional transfer functions for high aperture systems obeying the sine condition," *J. Opt. Soc. Am. A*, **11**, 593–598.

Sheppard, C. J. R., Hamilton, D. K., and Cox, I. J. (1983) "Optical microscopy with extended depth of field," *Proc. R. Soc. Lond. A*, **A387**, 171–186.

Sheppard, C. J. R. and Larkin, K. G. (1997) "Vectorial pupil functions and vectorial transfer functions," *Optik*, **107**(2), 79–87.

Sheppard, C. J. R. and Török, P. (1997a) "Effects of specimen refractive index on confocal imaging," *J. Microsc.*, **185**(3), 366–374.

Sheppard, C. J. R. and Török, P. (1997b) "An electromagnetic theory of imaging in fluorescence microscopy, and imaging in polarization fluorescence microscopy," *Bioimaging*, **5**, 205–218.

Sheppard, C. J. R. and Török, P. (1998) "Dependence of Fresnel number on aperture stop position," *J. Opt. Soc. Am. A*, **15**, 3016–3019.

Sheppard, C. J. R. and Wilson, T. (1980) "Fourier imaging of phase information in conventional and scanning microscopes," *Proc. Roy. Soc. London A*, **295**, 513–536.

Sherif, S. and Cathey, W. T. (2003) "Depth of field control in incoherent hybrid imaging systems," in P. Török and F.-J. Kao (Eds.), *Optical imaging and microscopy: techniques and advanced systems*, vol. 87 of *Springer series in optical sciences*, chap. 5, pp. 111–142, Springer-Verlag, Berlin.

Shimada, W., Sato, T., and Yatagai, T. (1990) "Optical surface microtopography using phase-shifting Nomarski microscope." *Proc. SPIE*, **1332**(2), 525–9.

Slomba, A. F., Wasserman, D. F., Gaufman, G. I., and Nester, J. F. (1972) "A laser fly spot scanner for use in automatised fluorescence antibody instrumentaion," *J. Assoc. Adv. Med. Instrum.*, **6**, 230–234.

Sprague, R. A. and Thompson, B. J. (1972) "Quantitative visualization of large variation phase objects," *Appl. Opt.*, **11**(7), 1469.

Stamnes, J. (1986) *Waves in focal regions*, Adam Hilger, Bristol, UK, 1st ed.

Steel, W. H. (1960) "Axicons with spherical surfaces," in P. Mollet (Ed.), *Optics in metrology*, pp. 181–193, Pergamon.

Stein, P. G., Lipkin, L. E., and Shapiro, H. M. (1969) "Spectre II: General-purpose microscope input for a computer," *Science*, **166**, 328–333.

Streibl, N. (1984a) "Depth transfer by an imaging system," *Optica Acta*, **31**(11), 1233–1241.

Streibl, N. (1984b) "Fundamental restrictions for 3-D light distributions," *Optik*, **66**, 341–354.

Streibl, N. (1985) "Three-dimensional imaging by a microscope," *J. Opt. Soc. Am. A*, **2**, 121–127.

Synoptics Ltd. (2001) "Auto-montage: Digital 3D imaging," http://www.syncroscopy.com/syncroscopy/am.asp.

Szoplik, T., Climent, V., Tajahuerce, E., Lancis, J., and Fernández-Alonso, M. (1998) "Phase-change visualization in two-dimensional phase objects with a semiderivative real filter," *Appl. Opt.*, **37**(23), 5472–5478.

Török, P. (1999) "Focusing of electromagnetic waves through dielectric interfaces: theory and correction of aberration," *Opt. Mem. Neural Netw.*, **8**(1), 9–24.

Török, P. (2000) "Imaging of small birefringent objects by polarised light conventional and confocal microscopes," *Opt. Commun.*, **181**, 7–18.

Török, P., Hewlett, S. J., and Varga, P. (1997) "The role of specimen-induced spherical aberration in confocal microscopy," *J. Microsc.*, **188**(2), 158–172.

Török, P. and Sheppard, C. J. R. (2002) "The role of pinhole size in high aperture two- and three-photon microscopy," in A. Diaspro (Ed.), *Confocal and two-photon microscopy: Foundations, applications, and advances*, pp. 127–151, Wiley-Liss, New York, USA.

Török, P., Varga, P., Laczik, Z., and Booker, G. R. (1995) "Electromagnetic diffraction of light focussed through a planar interface between materials of mismatched refractive indices: an integral representation," *J. Opt. Soc. Am. A*, **12**(2), 325–332.

Tschunko, H. F. A. (1974) "Imaging performance of annular apertures," *Appl. Opt.*, **13**(8), 1820.

Tschunko, H. F. A. (1981) "Annular apertures with low and high obstruction," *Appl. Opt.*, **20**(2), 168.

Tucker, S. C., Cathey, W. T., and Dowski, E. R., Jr (1999) "Extended depth of field and aberration control for inexpensive digital microscope systems," *Opt. Express*, **4**(11), 467–474.

Urbańczyk, W. (1986) "Optical transfer function for imaging systems which change the state of light polarization," *Optica Acta*, **33**(1), 53–62.

Valdecasas, A. G., Marshall, D., Becerra, J. M., and Terrero, J. J. (2001) "On the extended depth of focus algorithms for bright field microscopy," *Micron*, **32**(6), 559–569.

van Munster, E. B., van Vliet, L. J., and Aten, J. A. (1997) "Reconstruction of optical pathlength distributions from images obtained by a wide-field differential interference contrast microscope," *J. Microsc.*, **188**(2), 149–157.

van Munster, E. B., Winter, E. K., and Aten, J. A. (1998) "Measurement-based evaluation of optical pathlength distributions reconstructed from simulated differential interference contrast images," *J. Microsc.*, **191**(2), 170–176.

Volkov, V. V., Zhu, Y., and De Graef, M. (2002) "A new symmetrized solution for phase retrieval using the transport of intensity equation," *Micron*, **33**(5), 411–416.

Waterman-Storer, C. M. (1998) "Microtubules and microscopes: How the development of light microscopic imaging technologies has contributed to discoveries about microtubule dynamics in living cells," *Mol. Biol. Cell*, **9**(12), 3263–3271.

Welford, W. T. (1960) "Use of annular apertures to increase focal depth," *J. Opt. Soc. Am.*, **50**(8), 749–753.

Wield, G. L., Bartels, P. H., Bahr, G. F., and Oldfield, D. G. (1968) "Taxonomic intra-cellular analytic system (TICAS) for cell identification," *Acta Cytologica*, **12**, 180–204.

Wilson, T., Neil, M., and Massoumian, F. (2002) "Point spread functions with extended depth of focus," in *Proc. SPIE*, vol. 4621, pp. 28–31, San Jose, CA, USA.

Wolf, E. (1959) "Electromagnetic diffraction in optical systems 1. An integral representation of the image field," *Proc. Roy. Soc. A*, **253**, 349–357.

Wolf, E. (1969) "Three-dimensional structure determination of semi-transparent objects from holographic data," *Opt. Commun.*, **1**, 153–156.

Xu, Y., Xu, Y.-x., Hui, M., and Cai, X. (2001) "Quantitative surface topography determination by differential interference contrast microscopy," *Opt. Precision Eng.*, **9**(3), 226–229.

Young, J. Z. and Roberts, F. (1951) "A flying-spot microscope," *Nature*, **167**, 231.